School of Systems Engineering

Dual Drive Series Actuator

by

Balazs Janko

Thesis submitted for the degree of Doctor of Philosophy

School of Systems Engineering

May 2015

University of Reading

Abstract

Industrial robotic manipulators can be found in most factories today. Their tasks are accomplished through actively moving, placing and assembling parts. This movement is facilitated by actuators that apply a torque in response to a command signal. The presence of friction and possibly backlash have instigated the development of sophisticated compensation and control methods in order to achieve the desired performance may that be accurate motion tracking, fast movement or in fact contact with the environment.

This thesis presents a dual drive actuator design that is capable of physically linearising friction and hence eliminating the need for complex compensation algorithms. A number of mathematical models are derived that allow for the simulation of the actuator dynamics. The actuator may be constructed using geared dc motors, in which case the benefits of torque magnification is retained whilst the increased non-linear friction effects are also linearised. An additional benefit of the actuator is the high quality, low latency output position signal provided by the differencing of the two drive positions. Due to this and the linearised nature of friction, the actuator is well suited for low velocity, stop-start applications, micro-manipulation and even in hard-contact tasks.

There are, however, disadvantages to its design. When idle, the device uses power whilst many other, single drive actuators do not. Also the complexity of the models mean that parameterisation is difficult. Management of start-up conditions still pose a challenge.

Declaration

I confirm that this is my own work and the use of all material from other sources has been properly and fully acknowledged.

Balazs Janko

Acknowledgements

First and foremost, I would like to thank my supervisors *Prof. Paul M Sharkey* and *Prof. William S Harwin* for their help throughout the years. I would also like to thank the many PhD students in the department whose projects inspired me to learn more about the vast field that is Cybernetics.
Many thanks go to my housemates and good friends Kim Cave-Ayland and Andrew Salmon, whose house is still not finished after having been living there for over three years. I am forever in your debt, Brian Tse.

Table of Contents

List of Tables

List of Figures

Glossary

Acronyms and abbreviations

DDA - Dual drive actuator
DoF - Degrees of freedom
HIL - Hardware in the loop
SDA - Single drive actuator

Notation

a - scalar
$\mathbf{a}$ - vector
$\mathbf{A}$ - matrix
a_i - i^{th} element of vector a
$a_{i,j}$ - element at row i, column j of matrix $\mathbf{A}$

Chapter 1

Introduction

Industrial robot research spans the second half of the 20th century [1], which not only saw the development of the physical construction, but improved on the functioning of manipulators by implementing a range of joint controllers and motion planners. Initial efforts focused on position control, whereby each joint is required to go to a specific position yielding the correct configuration of the arm. Once achieved, a second configuration is commanded. This cycle repeats as the planner traverses all required configurations. Further advancements from the 1980s made a great impact on applicability due not only to new ideas in control, but also to improvements in the drive electronics, actuator design and sensors [2]. As applications dictate the design of the manipulators, there are a great number of different configurations, a large range of actuators and suitable control approaches available now.

Robotic actuation is concerned with controlled motion of each joint of a manipulator [3]. At a conceptual level, a robotic manipulator is comprised of a mechanical structure, drives and transmissions, sensors and power source. Additionally, control software is required to perform closed loop joint control with a motion planner to guide each joint, safety guards to ensure the safe functioning along with the safety of the robot and its surroundings. In order to perform its tasks, the manipulator is

required to move through a series of actions - preprogrammed arm configurations, free motion and contact tasks. It may also be required to accommodate for unforeseen additional events such as contacts with obstacles.

It is also possible to reverse the role of the robot arm and let an operator manipulate its position. Coupled with the use of virtual reality these systems provide force feedback creating the sensations of touching surfaces and objects that are purely virtual. Haptics, as the field is known, is concerned with the recreation of sensory experiences which let the operator believe they are experiencing touching an object.

1.1 Research motivation

This thesis concentrates on the actuator design of a robotic manipulator and presents a new configuration with considerable advantages. A dual drive series linked redundant actuator is proposed, which can be operated in such a manner that its output exhibits linear friction properties.

An actuator with such properties is attractive because its torque production is linear over all output velocities, and hence classical linear control theory can be applied. In practical actuators, elaborate control schemes have been devised which aim to compensate for the non-linear response of drives with gearboxes. However, if the drive inherently provides a linear response, then the control effort can focus on the task at hand. Also, such a property is highly desirable in creating truly transparent haptic devices where the operator feels no residual forces whilst in free space and not in contact with virtual objects.

A second reason for trying to eliminate the need for compensation is that such schemes are limited due to the quality of measurements available and imperfect compensation can lead to degraded performance, limit cycles or even instabilities [4].

And finally, such actuators (with inherently simpler control systems and desir-

able output behaviour regardless of the presence of gearboxes) may be constructed cheaply, can be designed to be manufactured as a single module and be a cost effective solution to highly demanding, accurate positioning tasks.

1.2 Research aim and objectives

The aim of the research is to model the dual drive series actuator to determine its performance, in particular to evaluate the extent to which friction is linearised at its output. Also of interest is to establish the design trade-offs of such an actuator in terms of friction, inertia and stability.

The objectives of the research are to carry out a thorough literature search, derive a suitable mathematical model to describe the actuator and evaluate its properties using numerical simulations. These results are to be compared to those of a practical implementation of the actuator. Finally, the suitability of such an actuator design in robotic applications is to be demonstrated.

1.3 Research methodology

The thesis presents background knowledge to summarise the key aspects of actuator design. A literature survey was carried out on the subject of robotic contact tasks and dual drive actuation. The survey presents the achievements of work found in the literature, and highlights the control strategies and complexity of design of the different approaches.

A mathematical model was derived from the equations of motion of the drives within the actuator. These are then expressed in state-variable form and the properties of the model, such as stability, are tested. It was found that the high order of the model makes algebraic analysis of stability impractical, hence reduced order models are also presented. Once the stability of the model was established, output friction

behaviour was investigated by means of numerical simulations.

A physical implementation of the system was built and a hardware in the loop (HIL) Simulink model was created to test and compare to the findings of the simulation study.

The implementation also allows for experiments to be carried out as a single drive actuator, hence it forms the basis of comparison. P only position control was demonstrated for both simulation and the physical system. The step response of both systems are compared to that of an equivalent second order response.

An impedance control scheme is applied to the the physical system to demonstrate the actuator's suitability for haptic applications.

1.4 Research contributions

- Suitable mathematical models of the dual drive actuator for 2, 3 and 4 degrees-of-freedom models are derived.
- The extent to which the actuator linearises friction is shown in both simulation and a practical implementation. The idle velocity of the combined rotor is demonstrated to have little effect on friction exhibited by the actuator.
- Stable control of the actuator is presented and its performance is compared to that of a single drive actuator.
- The actuator is shown to be applicable in a number of areas in robotics. In particular, it is demonstrated in a haptic wall application and the actuator may form the basis of more novel haptic devices.

1.5 Thesis outline

Chapter 2 presents background knowledge in the mathematical modelling of dc motors, transmission and losses. Sources of non-linearities arising from backlash, friction are described. Also introduced is the fundamental concept behind haptic rendering as an example application area for the prototype actuator.

Chapter 3 describes the findings of the literature review on backlash and friction compensation techniques and their efficacy, and also discusses approaches to robotic contact tasks and the challenges arising in making contact with the physical world. Approaches to dual drive actuation and current themes and areas of application are identified.

Chapter 4 presents the mathematical modelling of the actuator. The most complete model is derived first, however its stability is impractical to analyse algebraically. Hence two reduced order models are presented that allow for the assessment of stability, at the expense of masking certain dynamics within the original model. The chapter concludes with a discussion on suitable friction models for simulation and also shows that the over torque production of the proposed actuator arrangement is limited to that of a single drive.

Chapter 5 lists the Simulink models and shows simulation results of these three models. Of primary interest is the output friction behaviour with the drives powered up. As the reduction in complexity in the models are made possible due to making assumptions about the coupling mechanism, its effects are also highlighted.

Chapter 6 describes experiments carried out on the physical actuator. First, an implementation with Harmonic drive actuators is presented along with details of the hardware in the loop configuration. The un-powered and powered open-loop behaviour is investigated and compared with simulation results from the preceding chapter. The step response of the system is compared against a characteristic second order response, such that a single drive actuator (SDA) can be compared with

the proposed dual drive actuator (DDA). Two practical closed loop systems are also presented: a classic PID position control, and a haptic virtual wall. Both of these applications compare the performance of the SDA and DDA.

Chapter 7 presents a discussion on the findings of the thesis and concludes that the DDA is worth pursuing in certain application areas. Although there are a number of disadvantages to this design, the effects of friction linearisation makes it a very attractive alternative actuator.

Chapter 2

Fundamental Concepts

Manipulators are generally constructed using linked sections, which are moved physically by actuators. There are two different groups of actuators: those that involve a form of transmission, and those that do not. In a *direct-drive* actuator the link is coupled rigidly to the rotor of the drive, whilst the previous link or base is attached to the stator. In this form, there is a direct transmission of torque, velocity and position from drive to link. In a *geared* or *belt transmission* actuator the rotor of the drive is coupled to the link through a gear-train or belt pulley. This arrangement allows for a modified torque, velocity and position relationship between the drive and the link.

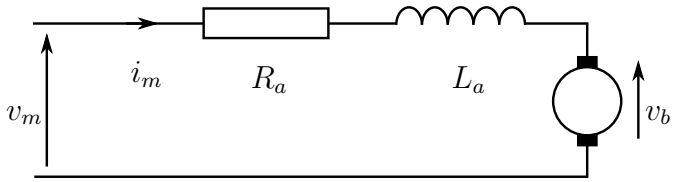

Figure 2.1: Electric equivalent circuit of a permanent magnet dc motor

A great number of manipulators have permanent magnet brushed dc motor actuated joints. The electrical equivalent circuit in Fig. 2.1 shows the applied motor voltage v_m, the armature resistance R_a and inductance L_a, and the current i_m. As the coils rotate through a magnetic field, the conductor cuts the magnetic flux and so a voltage v_b is generated by the rotor. This induced voltage is proportional to the

velocity and is given as $v_b = K_m\dot{\theta}_m$.

Using Kirchoff's second law, the circuit equation is

$$v_m(t) = R_a i_m(t) + L_a \frac{di_m(t)}{dt} + K_b\dot{\theta}_m \tag{2.1}$$

As the permanent magnets provide a constant magnetic field, the torque produced by the motor is proportional to the current in the coils and is given as $T_m = K_t i_m$. By balancing the torques acting on the rotor, the following relationship also holds

$$K_t i_m(t) - T_l = J_m\ddot{\theta}_m(t) + B(\dot{\theta}_m) \tag{2.2}$$

where T_l is the load torque, J_m is the rotor inertia, B is the function of friction and K_t is the motor torque constant.

The Torque/Velocity curve of a permanent magnet dc motor may be expressed in terms of torque T_m or velocity $\dot{\theta}_m$

$$T_m = T_s - \frac{\dot{\theta}_m T_s}{\dot{\theta}_s} \tag{2.3a}$$

$$\dot{\theta}_m = \dot{\theta}_s - \frac{T_m\dot{\theta}_s}{T_s} \tag{2.3b}$$

where $\dot{\theta}_s$ and T_s are the no load velocity and stall torque of the motor. This is shown in Fig. 2.2.

At a constant velocity the current through the motor coil is also constant. Using (2.1) and replacing i_m with $\frac{T_m}{K_t}$, the following expression may be used to find the available torque at a velocity $\dot{\theta}$ for a given supply voltage v_m

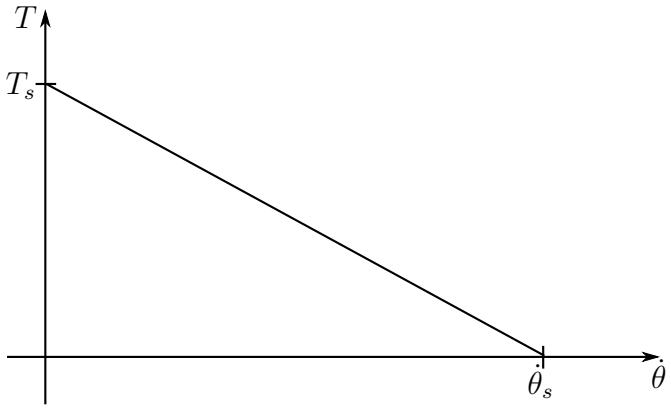

Figure 2.2: Torque-speed characteristics of a dc motor

$$T_m(v_m, \dot{\theta}) = K_t(\frac{v_m}{R_a} - \frac{K_b\dot{\theta}}{R_a}) \tag{2.4}$$

Note that when working in SI units, K_b and K_t have the same numerical value only expressed in different units. In practice this allows K_t to be determined more easily as K_b can be measured more accurately [5].

This set of equations which describe the torque and velocity production of a brushed dc motor, along with the relative simplicity of drive electronics make these motors understandably popular.

2.1 Transmission

In a given manipulator pose, every link experiences some torque due to gravity acting on its centre of mass and on further links. This torque, along with torques arising from motion (including torques due to Coriolis effects) must be countered and overcome by the torque of the actuator in order to accelerate the link. When using direct drive actuators, the available torque is directly proportional to the motor current as given in (2.2). However, the physical size and weight of actuators often required by such design would be prohibitive as the drives would contribute unacceptable amounts inertia to the links and hence require even more torque from the actuators.

Applying a form of transmission can solve this problem. Gearboxes can magnify the torque of the drive and so physically smaller devices can produce torque equivalent to that of larger ones.

A gear transmission [6] is comprised of at least two gears with cut teeth that mesh together. One is the *driver gear* and is considered as the input to the transmission, the other is the *driven gear* and is considered as the output. There may be additional gears meshed between the *driving* and *driven* gears. There are also a number of possible geometric arrangements, as in the case of the planetary and cylindrical gear, which allow the input and output shafts of the gear train to lie on the same axis. This essentially allows the drive to be mounted coaxially with the transmission, creating one single drive unit. There are also other geometric arrangements for gears, but these are outside of the scope of this thesis.

Ideal gear transmission relationships for velocity ($\dot{\theta}$) and torque (T) can be expressed as

$$\dot{\theta}_{\text{out}} = -\frac{1}{r}\dot{\theta}_{\text{in}} \tag{2.5a}$$

$$T_{\text{out}} = -rT_{\text{in}} \tag{2.5b}$$

where $r > 1$ is the gear ratio and the subscripts *in* and *out* signify the input and output quantities of the gear-train, respectively. The $-ve$ sign notation reflects the usual gear arrangement that reverses direction of motion.

When inertia J is attached to the output of the gearbox, the input side equation of the torque balance (assuming ideal conditions) becomes

$$T_m = \frac{1}{r}(J(\frac{1}{r}\ddot{\theta}_m))$$

This relationship demonstrates that any inertia present on the output of the

gearbox will be reduced by a factor of r^2. Conversely, torque acting on the output is magnified by a factor of r. Hence it is possible to apply smaller motors to manipulators when combined with gearboxes.

An alternative to mating spur gears is strain wave gearing or *harmonic drives* [7]. In this form of gearing a toothed flex-spine is placed between the toothed stator and a wave generator. The spline is connected to the output shaft and the wave generator to the input shaft; the teeth on opposite sides of the elliptically shaped flex-spline are engaged with the teeth of the stator. As the wave generator rotates, the spline - which has fewer teeth than the stator - rotates in the opposite direction as the teeth re-engage. There have also been incremental changes proposed to this design, such as by Maiti [8], where the wave generator is altered. The previously derived equations for spur gears still hold, however losses as discussed below are also more pronounced.

2.2 Losses

Losses in gear trains arise due to a number of factors, such as friction between engaged teeth and lubrication losses, where viscous friction effects dominate due to the gears travelling through a lubrication medium. Gear train design and analysis is a very mature area and there has been a lot of interest in characterising losses in gear trains [9, 10, 11], the effects of tooth losses and predicting failure [12, 13]. The efficiency of each stage of spur and helical gearing is around 98%-99% [14]. Higher gear ratios of 1:20 and above require multiple stages and hence the resultant efficiency may be around 70% or higher.

In harmonic drives, most of the friction forces arise from the continual deflection of the spline, which in itself is a highly complex and non-linear behaviour [15] and is beyond the scope of this thesis. However, as the result of its construction both static and dynamic friction is greatly magnified and the mechanism also introduces

a position dependent element to its torque transmission profile. The characteristic efficiency for this type of transmission is around 40% to 80% [7].

Simple spur gears, planetary and cylindrical gearboxes suffer from a phenomenon called backlash, which is discussed next. Backlash is all but eliminated from harmonic drives, hence this type of gearing has been widely used in positioning applications such as high precision mirror grinding, space manipulators and medical devices [7].

Both methods of transmission also suffer from the presence of friction, which is discussed in detail in the following sections.

2.3 Backlash

Backlash in a pair of gears is the result of tooth clearance between the mated teeth of two gears, and is evoked when the rotation is reversed. Theoretically, backlash could be eliminated from the design, however practically some clearance is necessary to prevent the gears from jamming, to allow for machining inaccuracies, effective lubrication and deflection from heat expansion [14, 16, 17].

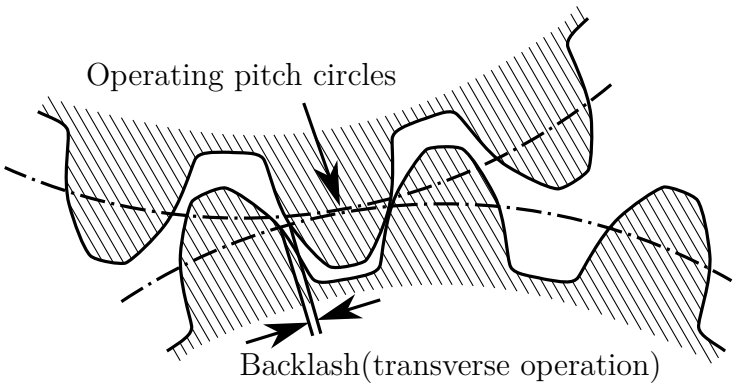

Figure 2.3: Mating gears with backlash

In robotics, the use of gears are necessitated as manipulators with lower inertia - but otherwise equivalent joint torque capability - may achieve a higher bandwidth of operation. This is a driving force in the creation of new designs as a higher bandwidth

allows faster motions and therefore reduced production time in an automated assembly line.

In a gear-train, backlash is cumulative. When the driving gear is reversed, it has to turn equal to all the backlashes before the the driven gear is engaged and begins to turn. As position encoding is usually done on the motor shaft instead of the output of the gearbox to increase resolution, backlash leads to calculation errors at every reversal of direction.

Figure 2.4: Anti-backlash gear

Backlash may be compensated for through design. In the case of spur gears, a gear may be split into two gears of half the thickness, supported on a common shaft as shown in Fig. 2.4. One half is fixed to the shaft, the other is allowed to turn on the shaft. A pre-tensioned springs are attached between these two gears, which rotate the second gear relative to the first one until all the backlash is taken out. This way, both sides of the pinion gear's tooth is engaged with the driven gear. Backlash is eliminated when the load does not exceed the spring forces - but due to the teeth forced to be in constant contact, friction is greatly increased in this design.

In other gear train designs such as worm drives, it is possible to have a worm gear with uneven thread width so that its relative position to the driven spur gear can reduce the amount of backlash present. These are popular in CNC machines, where the wear of parts may be periodically accounted for by manually adjusting the gears.

In robotic applications however, manual adjustments are difficult or impractical to perform, so two options remain in order to eliminate backlash. One is to use direct-drive mechanisms, where no gears are present. This approach may not be suitable where large torques are necessary as that necessitates a physically larger drive and it also has the undesirable effect of the introduction of torque ripple to the link.

Another method of backlash compensation is by the control system itself. Upon velocity reversal, the motor is additionally driven such that the amount of backlash is taken up and the driven gear is re-engaged. This method, however, inherently allows uncontrolled motion in the link during this period.

2.4 Friction

Friction forces are a result of surface irregularities and asperities coming into contact. The effect depends on a number of factors including the properties of the materials, relative velocity and displacement, the presence of lubrication among others. Ever since Da Vinci there have been a number of models developed that aim to characterise and describe the nature of friction. Friction in every day life is a very useful phenomenon, however its presence in manipulators may lead to a reduction in positioning accuracy, slip-stick motion and even the introduction of limit cycles. Regardless of the type of actuators used, a common element to all is the presence of friction. This section introduces some of the established models, and demonstrates that compensating for these effects is a difficult engineering challenge.

One of the simplest and earliest example of static friction models is the Coulomb and viscous friction

$$F(\dot{x}) = F_c \text{sign}(\dot{x}) + b\dot{x} \tag{2.6}$$

where F_c is the Coulomb friction, b is the viscous friction coefficient, F is the friction force and $\dot{x}$ is the relative surface velocity.

Stiction is the phenomenon where a higher friction force is present before relative motion begins. The applied force therefore has to overcome a breakaway force F_s, which may be incorporated into the above model. It has also been demonstrated that the transition from stiction to motion is a continuous function of velocity and hence there have been a number of models incorporating this aspect called the *Stribeck effect*. Model (2.7) presents a function that captures Coulomb and viscous friction along with stiction and the Stribeck effect

$$F(\dot{x}) = [F_c + (F_s - F_c)e^{-|\frac{\dot{x}}{\dot{x}_s}|^s}]\text{sign}(\dot{x}) + b\dot{x} \tag{2.7}$$

where s is the coefficient for the decay of the Stribeck effect and $\dot{x}_s$ is the velocity region for which the Stribeck effect is present. The difference between these models is shown in Fig. 2.5.

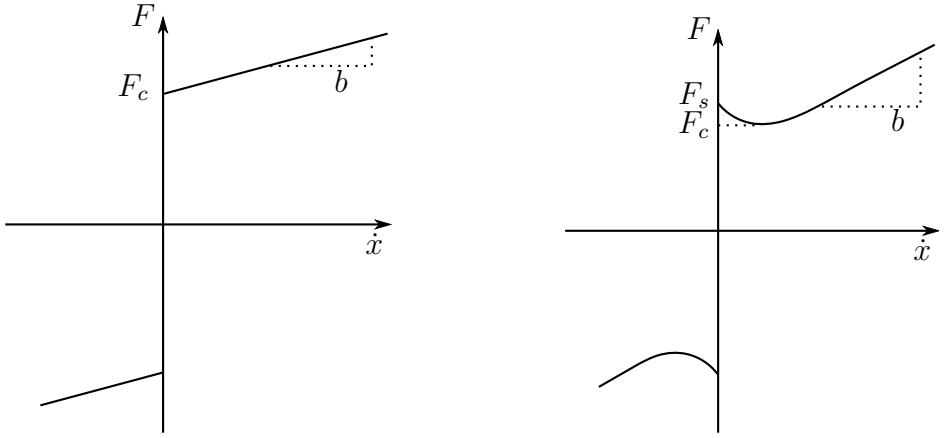

(a) Coulomb and viscous only (b) Coulomb, viscous and Stribeck effect

Figure 2.5: Static friction models

The presence of Coulomb friction poses a great challenge for the numerical simulation tools due to the abrupt discontinuity at zero relative velocity [18]. To overcome this limitation, a variation can be introduced to Model (2.7) as

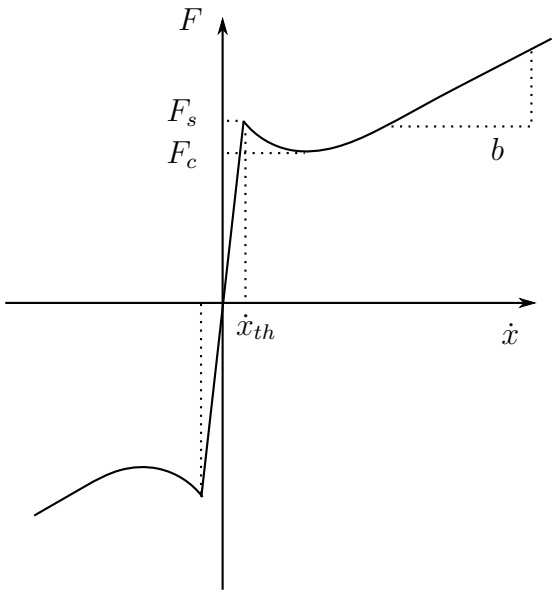

Figure 2.6: Continuous Coulomb, viscous and Stribeck friction

$$f_f(\dot{x}) = \begin{cases} (C + (F_s - C)e^{-s|\dot{x}|})\text{sign}(\dot{x}) + b\dot{x} & \text{if } |\dot{x}| \geq \dot{x}_{\text{th}} \\ \frac{\dot{x}}{\dot{x}_{\text{th}}}((C + (F_s - C)e^{-s\dot{x}_{\text{th}}}) + b\dot{x}_{\text{th}}) & \text{if } |\dot{x}| < \dot{x}_{\text{th}} \end{cases} \tag{2.8}$$

where a threshold velocity $\dot{x}_{th}$ is defined below which the function assumes a fraction of the breakaway force proportional to the actual velocity $\dot{x}$. Model (2.8) is hence a continuous function as shown in Fig. 2.6.

Due to the presence of this fractional force, the surfaces may move relative to one another. This addition, as long as $\dot{x}_{th}$ is small enough to approximate the discontinuous form shown in Fig. 2.5b, allows for a very efficient numeric simulation. As this model yields what is considered to be a stiff system, the selection of a suitable differential equation solver is essential.

Another group of friction models take into account the effect that can be observed when investigating friction at a microscopic level. Asperities in both surfaces engage and deform due to external forces acting on them. The models based on capturing this behaviour are called dynamic models. These can describe hysteretic effects of friction, variations in breakaway force and small displacements which occur during

stiction.

One of the best known models is the Dahl model [19] first published in 1968. By defining the average asperity or bristle deflection as z, the model which defines the friction behaviour is

$$\dot{z} = \sigma\dot{x} - \frac{|\dot{x}|}{F_c}\sigma z \tag{2.9a}$$

$$F = \sigma z \tag{2.9b}$$

where z is the bristle stiffness parameter. As it is a very simplistic model, it does not include the Stribeck effect or stiction, however it is very easy to parameterise. A more complete model is an extension to the Dahl model called the *LuGre* model as presented by de Wit et al. [20]. This friction model includes both stiction and the Stribeck effect, given as

$$\dot{z} = \dot{x} - \frac{|\dot{x}|}{g(\dot{x})}\sigma_0 z \tag{2.10a}$$

$$F = \sigma_0 z + \sigma_1 \dot{z} + f(\dot{x}) \tag{2.10b}$$

where σ_0 and σ_1 are constants, $f(\dot{x})$ and $g(\dot{x})$ describe viscous friction and the Stribeck effect respectively. The LuGre model is more difficult to parameterise as functions $f(\dot{x})$ and $g(\dot{x})$ may take on a number of different forms, as discussed by de Wit [21]. The identification of model parameters have been described by Bona et al. as cumbersome, error prone and require high precision sensors to capture high quality data for characterisation of the pre-sliding phase [22]. Further, more complex models have also been developed, such as the Leuven model [23].

These dynamic models are based on particular properties, and other exhibited

behaviour is a coincidental consequence of the formulation. Lampaert et al. [24] claim that dissipativity [25], which is inherent in friction and depends on model parameters, is difficult to prove for these models. This difficulty means that more appropriate models for control are still sought after. Lampaert et al. proposed a physically motivated generic friction model [26] which is highly computationally expensive, but may be used to derive simpler - albeit less generic - models which are faster to compute.

The Generalized Maxwell-Slip (GSM) model [24] is an example of such derived, simpler model suitable for control applications. The paper investigates its properties and compares its behaviour to that of other models and the generic model. The model builds on two groups of ideas. The first group includes mechanisms like normal creep of the contacting asperities, adhesion and hysteresis losses as a consequence of geometrical deformation. The second group involves the asperity contact scenario, where the two flexible contacting surfaces are transformed into a set of flexible spring-mass elements, where each element has its own contact profile. This model is inherently dissipative as energy of the deformed asperity is lost upon it losing contact.

2.5 Haptic displays

In areas such as automated assembly, warehouse management, manufacturing etc. the manipulator is interacting with physical objects. In kineasthetic haptic applications, the manipulator is instead used to provide force feedback that allows humans to interact with virtually generated objects[27].

The simplest form of haptic actuator is a one degree of freedom device that measures the position of the operator (the end effector) and applies a force along a single spatial dimension. This is a form of impedance control, and may be utilised to

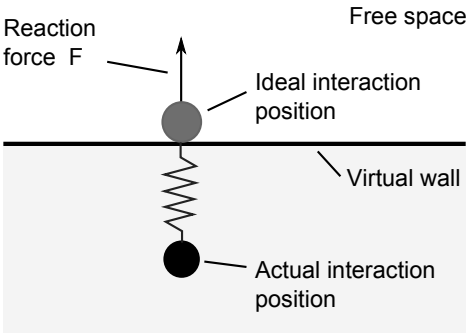

Figure 2.7: Virtual wall concept along one spatial dimension. The reaction force is proportional to the difference between the actual and desired effector position

create a rendering of a virtual wall using the control law

$$F = \begin{cases} 0 & \text{when } x > x_w \\ -k(x_w - x) & \text{otherwise} \end{cases}$$

where k is the stiffness of the contact, x_w is the location of the virtual wall and x is the measured position of the end effector or haptic interaction point. As the user approaches the wall, the actual interaction point will penetrate the wall and so the resultant force can be computed to set up a spring force. This force acts as to return the measured point to the ideal wall contact point. Although it is a very simple form of haptic interaction, it forms the foundation of a haptic stability and impedance fidelity analysis [28, 29].

Once the virtual wall in constructed, the user can move freely in space when $x > x_w$. In an ideal case, the user should feel no force from the haptic device. Impedance controlled haptic devices - which respond with a force to a change in position - are physically moved by the operator, hence forces due to friction and manipulator inertia will be felt. Admittance controlled devices - which actuate themselves as to produce the required position to achieve a commanded contact force with the user - are capable of minimising the forces felt in free-space motion, however due to limited actuator bandwidth this advantage diminishes as acceleration increases.

Furthermore, admittance control requires the measurement of contact force between the operator and the robotic arm, that add cost and complexity to such devices.

2.6 Summary

This chapter introduces the basic concepts of electric dc motor and transmission modelling. The phenomena of friction is described along with a number of models that have been developed to try and characterise its complex behaviour. These concepts are key in order to further understand the challenges in creating a new type of actuator or to control current actuators, as described in the following chapter. Also briefly introduced is the basic concept of haptic feedback, which allows operators interacting with robotic manipulators to feel surfaces and virtual objects through the use of force feedback.

Chapter 3

Literature review

All forms of robotics require the use of actuators to articulate the manipulator according to the controller to achieve a certain task. Hence all manipulators encounter challenges with motion control due to sources of non-linearities as discussed in Chapter 2. This chapter highlights methods of mitigating such non-linear effects and also presents control approaches of robot manipulation where a form of contact is made with the physical environment. The chapter then describes the case of haptic contact tasks where the manipulator arm is to simulate contact with virtual surfaces.

3.1 Backlash compensation

As described in the previous chapter, as backlash causes delay, oscillations, limit cycling and inaccurate tracking may result at the output. Even in anti-backlash designs a certain amount of non-linearity may still be present, which require a more comprehensive control approach [30]. There have been a number of different methods deployed in combating both conservative and anti-backlash gear designs [31].

Mokhtari et al. use a two-stage design process, where initially a linear position controller is designed to meet certain performance criteria [32]. This ensures that backlash is effectively reduced to a delay, which comes into effect at every rotation

reversal. At this stage a feedforward part is introduced, which aims to minimize this delay by traversing the motor gear through the backlash gap as fast as possible, which leads to a reduction in delay. Although simple, an instantaneous rotation equal to the backlash in the gearbox is infeasible, so this approach may only be able to reduce the effects, not to eliminate them.

Another control approach, similar in nature is the one presented by Mohan et al. [33]. An inner position loop is constructed with the assumption of no backlash effects and is designed to meet the performance criteria. Steady state control of load position can be achieved by exponentially delayed introduction of load position feedback. Although purely analytical, this paper and a successive paper [34] both demonstrate a very simple yet effective approach whereby knowledge of only the gear-ratio and not the actual system backlash is necessary.

Other, more intricate control designs aim to maintain an inverse backlash model, which also has been a popular method [35, 30, 36, 37]. Some compensation efforts utilise fuzzy logic during the identification of the model parameters, such as presented by Woo [38] and Tao [39]. Mohammadzaman argues that when a good model of backlash is known, predictive control may be used successfully in eliminating the adverse effects of backlash [40, 41]. A model may be obtained through identification, such as described by Marton and Lantos in [42].

Backlash can also lead to vibration which may be observed when torsional compliance is added between the load inertia and the output of the gearbox [43, 44].

Backlash is inherent in many transmission designs and, as shown by these papers, is difficult to compensate for. Other forms of transmission such as belt drives also suffer from a form a backlash introduced by the reversal of tension and slack sides of the belt.

3.2 Friction compensation

As manipulators are required to position themselves precisely, friction effects must be compensated for. Having chosen a model, friction compensation can take place, which aims to eliminate the non-linear friction so that the actuator (and hence the system) appears to behave linearly.

In the case of independent joint control, where torques acting on the actuator (due to gravity or Coriolis effects) are treated as disturbances, a fixed compensation term is added through feed-forward. This method of compensation requires good knowledge of the friction coefficients, which may be estimated by systems identification techniques [45].

Mallon et al. [4] present a reduced-order observer to recover the unobserved state of the system. The friction compensation model makes use of this estimate to create a bias torque which, together with the controller torque, form the control signal to the joint. An investigation of the closed-loop dynamics is also carried out for both exact and non-exact friction compensation, and a set of design rules are proposed in terms of controller and observer parameters which will result in global exponential stability. It is also shown that in the case of non-exact friction compensation, undercompensation leads to equilibrium set (of possible positions where motion stops) and overcompensation leads to limit cycling.

Estimation of model parameters is a common way to derive compensators, as described in [46]. The velocity dependent friction model is defined as

$$T_{fv}(\dot{\theta}) = \begin{cases} f_p + f_{vp}\dot{\theta}_e + f_{ap}\dot{\theta}_e^2 & \text{if } \dot{\theta}_e > 0 \\ \left(\frac{f_p - f_n}{2}\right) sign(T_m) & \text{if } \dot{\theta}_e = 0 \\ f_n + f_{vn}\dot{\theta}_e + f_{an}\dot{\theta}_e^2 & \text{if } \dot{\theta}_e < 0 \end{cases} \tag{3.1}$$

where f, f_v and f_a are constant coefficients, the subscripts p and n denoting the

positive and negative directions respectively.

Model (3.1) shows that second order polynomials are used to better approximate the experimental results. Gomes et al. note that the experiments as presented in [46] were carried out using a harmonic drive gearbox, the operation of which induces a sinusoidal change in the torque produced dependent on the rotor position.

On-line compensation techniques include model-based adaptive algorithms. In this scheme a specific friction model is chosen whose gains are changed to achieve satisfactory results [47, 48].

Other on-line compensation techniques include the *soft-computing* approach, such as neural networks or fuzzy logic, to estimate the friction force. Mostefai et al. describe a method of compensation using a fuzzy observer [49]. A set of linear controller gains are effectively interpolated using the fuzzy inference method. The results presented show good tracking performance and represent a simpler technique than many of the aforementioned models. While previous models effectively linearise the response, this method - through *switching* between suitable control gain values - can be the basis for further developments when using robust adaptive control and hybrid-control strategies.

A large body of research is concerned with the effects, identification and compensation of non-linear friction effects at low joint velocities. As described in the previous chapter, all friction models other than the purely viscous friction exhibit undesirable, non-linear effects at low interface velocities near the vicinity of zero. A common method is to utilise model based disturbance observers [50, 51, 52], the observer tracks deviations of the dynamic model to estimate the forces of the manipulator. Although primarily concerned with estimating the exerted force by the manipulator, such an approach may also be used in conjunction with a force sensor to identify joint friction parameters. Friction compensation is usually realized based on a friction model [53, 54, 55], but inherent under- and overcompensation will inevitably

lead to steady-state error or limit-cycling. PID control alone is insufficient to eliminate limit cycles in the presence of Coulomb and static friction [56]. Furthermore, under low velocity conditions, high gain PD control (which is otherwise a robust technique to achieving low steady-state error without limit cycling) fails to achieve low steady-state error. [57]. Alternative control approaches have been studied in depth, such as the addition of feedforward [58], adaptive [59, 60] and sliding mode control [61, 62]. Although the approaches perform very well, they either reply on a static two stage identify-compensate paradigm or online, adaptive mechanisms for identification and mitigation of friction effects.

There are many more examples of friction compensation. It has been a very active area of research as a main limiting factor of high performance robotics is the presence of friction. The difficulty with compensating for this phenomenon is its dependency on the specific implementation of the actuator including its controller. Certain manipulators may allow for sophisticated compensation techniques, which are, however, unsuitable for others due to variations in the drive mechanics, transmission, controller implementation. As Mallon et al. demonstrate in [4], any control effort with non-exact friction compensation will lead to undesirable behaviour and will affect the motion and stability of the joint.

3.3 Contact tasks in robotics

Most tasks carried out by robots involve some contacts, such as manipulation of the environment, other robots, or even interaction with humans. Some tasks pose only a small challenge as there is little - if any - actual contact between the manipulator and the manipulandum, like in the case of spot welding. However, most tasks prove to be of a more complex nature, where the robot has to come into contact with, and exert force on objects, such as assembly, drilling etc. Once the manipulator has coupled to

its environment, simultaneous control of both position and force present a challenge in robotics.

Hogan [63] proposed a unified approach to robot manipulation called impedance control, which - without having to explicitly switch between different control strategies - copes with free motion, constrained motion and the transition between them. The robot is considered rigid and the environment modelled by an appropriate impedance. This method builds on the dynamics of the environment - albeit it is restricted to a linear model. Impedance control seeks to impose a desired dynamic relationship between positioning errors and end effector forces. The controller is to replace the manipulator's impedance with the desired impedance using feedback of measured positions, forces, accelerations and a model of the manipulator dynamics.

In manipulator robotics, the need for an end effector coming into contact with its environment is mostly inevitable. In certain tasks, the effector or even the environment exhibit some level of compliance and so - although still complex - the behaviour of the control methodology inherently has a more relaxed design criteria than that of tasks where hard-on-hard contacts occur. When an otherwise rigid robot comes in contact with a stiff environment, the manipulator is effectively static. This leads to an elimination of velocity feedback, which in manipulators with high quality joints (that have low friction and therefore low passive damping) effectively eliminates the only source of damping for stabilising the system. Alici et al. [64] concludes, that when the above is the case, high quality and high resolution encoders are necessary to stabilise such a system. One common way to increase the resolution is through the use of gears (this is one of the reasons why geared actuators are so abundant). However, in direct drive systems there is no such advantage and costly, high resolution encoders must be used.

Glover et al. [65] discusses simulation models which include highly non-linear effects such as slip-stick friction and backlash along with some commonly ignored

effects of motor and load dynamics. The paper presents a very detailed discussion of motor gearbox friction model including a hardware in the loop simulation where practical considerations are also included, such as delays and sample rates.

Of primary concern when it comes into contact tasks is the transition between the manipulator's free motion and force exertion once the manipulator has coupled to its manipulandum. Control mechanisms have to either clearly distinguish between these two states, as in hybrid control, along every degree of freedom; or incorporate a unified approach to defining position/force for every configuration, as in for example, impedance control.

The problem is further exacerbated when the otherwise stiff manipulator encounters a hard contact, where effects such as bouncing and limit cycling may lead to instability and therefore there is also a need to develop new methods and further extend the above approaches. Friction and backlash also play a key role in degrading performance and result in inferior behaviour than that predicted by simulations [66].

When the manipulator is in free space and is therefore not in contact with its environment, position control can be used. Once in contact however, as discussed above, this control scheme no longer facilitates motion control, and some form of force control is necessary. For impedance control to be effective, the encountered contact (desirably exact) model must be incorporated into the controller, and is therefore unsuitable in applications where these are uncertain or even unknown.

The main issue presented in hard contact problems is to design a controller to achieve stable contact transition and output force regulation with minimum impact force and bouncing. The transition from free motion to contact presents three modes of controller operation: free-motion, phase-transition and contact-motion modes. It is the phase-transition which was last to be researched as historically free-motion control modes were endeavoured first, followed by contact-motion control techniques assuming that the transition was already carried out successfully.

In transition mode, the end effector may repeatedly lose and regain contact with the object, during which large forces can be exerted possibly leading to damage to both. When contact is lost, the force measurements drop to zero, which in turn leads to limit cycle response or even instability. There have been a number of different transition mode controllers developed [67, 68, 69, 70, 71, 72]. Common to the switching scheme is that they seek to provide a stable response, but under certain circumstances may still exhibit chattering [73]. Among the above mentioned control schemes belong the one presented by Doh et al. [74]. An additional (pre-transition) phase is introduced as a *suppression controller* that suppresses position rebounds in-between the impact times. This ensures that control is handed over to the transition phase with a bounded maximum rebound force, thus allowing for a smoother transition. There is, however, still a period during which contact is made and subsequently broken off.

There have been alternative attempts - such as in [75, 76] where kinematic redundancy was exploited to reduce impact force - to tackle the issues which arise during this phase, along with those presented in [73, 77, 78, 79], which describe a recent adaptive control method.

The stability upon losing contact with the environment is assessed in the case of four different control schemes in [80]. These are: hybrid force control, resolved acceleration based force control, stiffness control and impedance control. The comparison is limited to linearised models (thus leading to local stability) - but non-linear models would allow for assessing global stability, which however may not be warranted as loosing contact and behaviour of the manipulator is in fact happening in a well defined initial position, about which motion should be highly restricted and the linearised models should hold valid.

3.4 Dual Drive Actuation

A number of prevalent technologies currently employ dual-drive actuation. In most systems, such as hard disk drives [81, 82, 83], compliant dual-drive joint actuators [84, 85, 86, 87] and a large reach haptic interface [88], there is a distinct master/slave, macro/micro configuration of the two drive mechanisms. Here, one drive is responsible for large magnitude (low bandwidth) motion whilst the other is responsible for low magnitude (high bandwidth) operation. The overall response represents a system with a higher bandwidth along with higher magnitude than that of either of its components alone [89]. Controllers of macro/micro actuator arrangements must also ensure that no excessive response is requested from the macro actuator [90] and that the small motion range of the micro actuator is compensated for by the macro actuator.

In haptic applications, increased bandwidth allows for a more transparent experience for the operator when encountering motion in free space [91]. This increase allows for faster motions with greater accelerations, yet the force applied to the user can be kept small. In case of impedance control, a higher bandwidth allows for stiffer contacts, while admittance control benefits from faster actuator reaction and hence a greater range of virtual mass simulation.

As hard disk drives store data on rotating platters in concentric rings, read/write heads must be positioned over the correct part of the platter accurately and in timely fashion. The increase in density of the packing and the reduced width of these rings lead to a move away from physically scanned actuation (using bulky and relatively slow stepping motors) to voice coil based designs [92, 93]. Modern hard drives must be able to reposition the heads within a few milliseconds, and they too employ a macro/micro actuator arm to achieve the high positioning bandwidth requirements.

On a larger scale, industrial and other manipulator robots must make greater movements and hence require physically larger drives in each joint. Kim et al. present a dual actuator unit where one drive provides positioning through a large gear re-

duction, whilst the other drive modulates the stiffness of the actuator [94, 95, 96]. The device is capable of simultaneously controlling both position and stiffness, which through the use of more conservative actuator designs utilising control approaches such as force feedback control or indirect impedance control would not be possible. Control schemes such as impedance control have been applied to a number of macro/micro actuator configurations [97].

A different approach is to use two, identical actuators, such as in the tape transport mechanism [98]. It uses independently controlled motors at both capstans, therefore the three servo loops (one for each reel and overall positioning) result in a high-order representation. Further presented is a design of achieving accurate end effector repositioning through the use of optimal control strategies.

Mitsantisuk et al. [99, 100, 101] present a design methodology for a twin direct-drive motor mechanism coupled through cable, which in turn positions an end effector. By using two motors of the same specification, the design is simplified. A dual disturbance observer with modal space design method is presented in [101] to create a robust motion controller which guarantees stability, and a degree of immunity of variation of mechanical parameters while accommodating for external force estimation. This estimate however is limited in accuracy due to the presence of static friction and reliance on an accurate friction model. The paper includes a detailed design pattern, along with discussion on how interaction with a human operator can be modelled and that the application of impedance control is appropriate.

Actuators with dual drives are also applied in robotic applications that interact with humans. Through physical design these actuators will display high compliance - much like the human body - and hence it has been found that the interaction is perceived to be more natural [102, 103].

In parallel configurations, dual drive actuation may also allow load sharing. In this case each drive only has to produce part of the overall load and hence wear is

reduced of the individual drive units [104]. The load may be shared evenly (following maximum load and acceleration requirements) or unevenly (usually one drive is named primary and selected first, the other drives positioned and specified as needed) [105]. This allows the loads on the transmission, usually a form of belt drive, to be carefully controlled (such as tension on a belt drive).

Most dual drive actuators are designed with a very specific problem in mind and hence their general applicability in manipulators are lost. However, the wide range of applications where they are used suggest that more generic actuators may be of benefit in other areas motion control.

3.5 Energy in rotary actuators

In any mechanical system, inertia acts as a storage device for energy. In the scope of this thesis, all actuator motion may be considered rotational, therefore the energy stored in a rotating mass - in its centre of mass frame - is given by

$$E_{rot} = \frac{1}{2} J \dot{\theta}^2 \tag{3.2}$$

where E_{rot} is the energy stored, J is the object's moment of inertia and $\dot{\theta}$ is the angular velocity.

The power of a rotating system can be described as

$$P_{rot} = T \dot{\theta} \tag{3.3}$$

where P_{rot} is the instantaneous power, T is the torque and $\dot{\theta}$ is the angular velocity.

3.5.1 Sources of losses

In brushed dc motors, the armature current is directly proportional to the torque production, increased torque demands result in higher average current. The resistive losses, which are dissipated as heat increase due to the exponential relationship

$$P(t) = i(t)^2 R$$

where $P(t)$ is the instantaneous power loss at time t, $i(t)$ and R are the instantaneous armature current and resistance, respectively.

In geared actuators, frictional losses arise as mating teeth slide against each other. Further losses occur due to the inevitable presence of friction in all moving parts such as bearings and seals. This is most evident in gearboxes and support bearings, especially when they are of a sealed type. Friction effects within the drive may also be magnified by the gearbox and hence it also contributes to overall sources of loss.

3.5.2 Loss minimisation and recovery

As torque production is dependent on armature current and geometry, if it is to be kept constant whilst current consumption is reduced, a larger armature is necessary and therefore the mass of the drive needs to be increased. This is largely impractical as it is an important criterion to keep inertia as small as possible. Frictional losses may be reduced through the use of lubrication, however it can not be eliminated and at higher angular velocities the lubricant can introduce detrimental effects on torque production. These losses will always be present and so the energy lost through these means are irrecoverable.

The kinetic energy of the load inertia is a prime candidate in energy recovery for a number of applications, such as the transportation industry (in cars, buses and

trams) and it was even trialled in Formula 1 [106]. As - in most cases - the inertia is already driven by an electrical motor, using the drive as a generator allows the recovery of rotational kinetic energy and storage as electrical energy in supercapacitors or batteries. This technique is relatively new as challenges in capacitor and battery technologies present themselves under such repetitive, high energy density applications. Once stored, the electrical energy can then be used to accelerate the inertia on demand. Although lossy, some energy is still recovered from the original kinetic energy which would have otherwise been burnt off during more conventional forms of braking.

3.6 Summary

The design and construction of actuators necessary to create robotic manipulators is greatly varied as the application dictates the criteria which their performance must meet. Many industrial robots utilise brushed dc motors due to their ease of control and well defined physical characteristics. To overcome their limitations, gearboxes may be added to form the actuator, which allow for a much increased torque production at the expense of increased friction and the introduction of backlash.

Backlash is a phenomenon which may lead to uncontrolled motion, reduced tracking accuracy and instabilities. It may be mitigated through physical design or by control action. As shown, the efficacy of the utilised schemes may be high, but at the expense of introducing more friction or increased control effort at every velocity reversal.

Friction is a much studied field and there are a great number of models with varying degrees of sophistication that describe the highly non-linear aspect of this phenomenon. Classic static models which capture certain aspects are limited when compared with dynamic models that effectively describe additional effects, such as

stiction and varying break-away forces. Most dynamic models are, however, very difficult to parameterise and there has been great interest in control theory to obtain good estimates for these. As static models define friction in a more intuitive way, for which parameter selection is therefore a more straightforward task, the rest of the thesis considers the use of static models only but the simulations may be extended to dynamic models as well.

As described earlier, friction plays a key role in hard contact tasks, where the manipulator encounters contact with a non-compliant surface. Research highlights the limitations of control schemes due to the presence of friction and the reliance on accurate knowledge of the manipulator dynamics along with fine measurements of contact force and joint positions.

As described in the following chapter, the proposed design is a form of series linked dual drive actuator. There are many application areas where dual drive actuation is utilised as the configuration allows for a macro/micro structure and therefore an increased bandwidth of operation. Hard-drive heads are a prime example of such arrangement, where very high bandwidth of operation can be achieved. Other actuators, such as large scale inherently compliant joints, may also be constructed that otherwise would be achieved by control action.

Chapter 4

Theory and Modelling

A proposed solution to mitigating non-linear effects - in particular friction - is to use two actuators (with the possibility of including a form of transmission) so they can operate in their linear region of the friction domain. This chapter describes such a revolute actuator design constructed using two brushed dc motors in a series configuration. As friction exists between the rotor and the stator, an investigation into this behaviour is presented first. Through the discussion of the physical construction of the actuator, a number of mathematical models are developed. Simulation results are presented in the following chapter.

4.1 Simple linear construction

Chapter 2 has demonstrated that friction is a complex phenomenon that exhibits highly non-linear behaviour in the zero vicinity of the contact surface velocity.

In order to investigate how the dual drive actuator performs in terms of friction, the following concept is introduced.

A block with mass m rests on ground, with force F_s applied to it at position x. Friction arises between the block and the ground as indicated by F_f, its value is implicitly a function of interface velocity and opposes the direction of motion. This

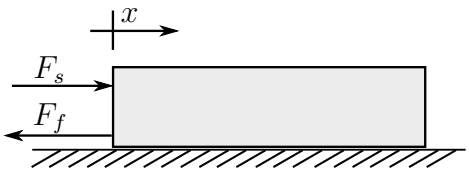

Figure 4.1: Simple linear friction - single sliding block

configuration can be thought of as a linear actuator, where the input is the applied force and the output is the resultant motion and position of the block. The dynamics of the block may hence be described as

$$m\ddot{x} = F_s - F_f(\dot{x}) \tag{4.1}$$

It is possible that the velocity of the block may fall below a minimum threshold, where the dynamic (slipping) regime is overcome by the static (sticking) regime as discussed in the previous chapter. To avoid this non-linear behaviour, the friction interface velocity must remain above this threshold value. This may be achieved by introducing a second, intermediate block (referred to as *Primary*) between the original block (now referred to as *Secondary*) and ground. The resulting configuration provides two interfaces where friction is present: one between the *Primary* block and ground (which follows the description above) and one between the *Secondary* and *Primary* blocks, which is shown in Fig. 3.2.

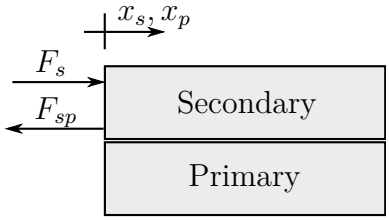

Figure 4.2: Simple linear friction - two blocks moving with respect to an inertial reference frame

In this case, a fraction of the input force is transferred between the blocks due

to friction according to the following equations

$$F_s = m_p\ddot{x}_p + F_{sp}(\dot{x}_p - \dot{x}_s) \tag{4.2a}$$

$$0 = m_s\ddot{x}_s + F_{sp}(\dot{x}_s - \dot{x}_p) \tag{4.2b}$$

These equations indicate that when F_s is removed, friction F_{sp} between the blocks will cause this interface velocity to decay to zero over time. However, the velocity of the *Secondary* block may take on any value with respect to ground. The complete scenario is shown in Fig. 4.3

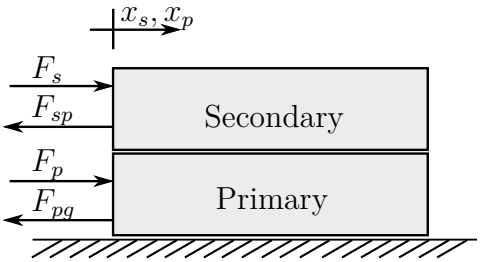

Figure 4.3: Simple linear friction using intermediate sliding block

Mathematically, the dynamics of the two blocks are governed by

$$F_s = m_s\ddot{x}_s + F_{sp}(\dot{x}_s - \dot{x}_p) \tag{4.3a}$$

$$F_p = m_p\ddot{x}_p + F_{sp}(\dot{x}_p - \dot{x}_s) + F_{pg}(\dot{x}_p) \tag{4.3b}$$

where F_{sp} and F_{pg} represent the functions of friction between the *Secondary* and *Primary* blocks, and the *Primary* block and ground respectively.

It is possible to maintain motion of the *Primary* block, whilst the velocity of the *Secondary* block relative to ground comes to zero. When the two interface velocities remain non-zero, F_{sp} and F_{pg} exhibit linear viscous friction.

This concept applies equally to rotating blocks: the first two configurations

readily translate to a direct-drive motor, where *Secondary* block represents the rotor and *Primary* block the stator. The combined configuration represents the proposed dual drive actuator and Fig. 4.4 is presented to aid the comparison between Fig. 4.3 and Fig. 4.5.

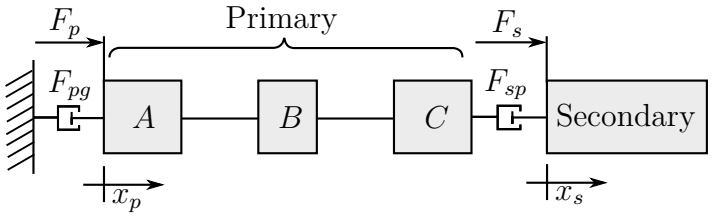

Figure 4.4: Lumped inertia model of sliding blocks

The stator of the primary drive is attached to ground. The rotor of the primary drive A is attached to the rotor of the secondary drive C through a coupling B by means of an infinitely stiff link. Together, blocks A, B and C form the previously introduced *Primary* block; the stator of the secondary drive forms the former *Secondary* block.

Friction F as a function of velocity $\dot{x}$ can be described as

$$F = B(\dot{x})$$

where $B()$ is a static friction model. At $\dot{x} \neq 0$ this expression reduces to just viscous friction, which can be substituted as

$$F = b\dot{x}$$

During the development of the model, B is treated as the function and $(\dot{x})$ notation is dropped to simplify the expressions. Instead of assuming that $\dot{x} \neq 0$, this simplification retains generality of the model for all velocities.

The following sections refine this initial concept and introduce a formal analysis of the proposed dual drive actuator.

4.2 The proposed actuator

In order to achieve a configuration as described previously, two brushed dc motors may be connected together using their rotors, as shown in Fig. 4.5. The rotors (of inertia J_{m1} and J_{m2}) are joined together using a coupling (of inertia J_c) with stiffness K_{c1} and K_{c2} (together these form the *Primary* block from before, henceforth referred to as the *Primary stage*). The stator of the primary motor is treated as ground. The stator of the secondary motor is attached to the load and is treated as the actuator output θ_L (together these form the *Secondary* block from before, henceforth referred to as the *Secondary stage*). Friction B_{m1} exists between J_{m1} and the stator of the primary motor, B_{m2} between J_{m2} and the stator of the secondary motor. In certain coupling mechanisms, friction may also exist between the coupling mechanism and each of the rotors, shown as B_{c1} and B_{c2}. Additionally there is friction B_s between the secondary stator and ground through the support bearing of the load. The motors develop torques T_{m1} and T_{m2} respectively, and T_L is the applied load torque, eg. due to gravity, subsequent links in a manipulator or disturbance torques.

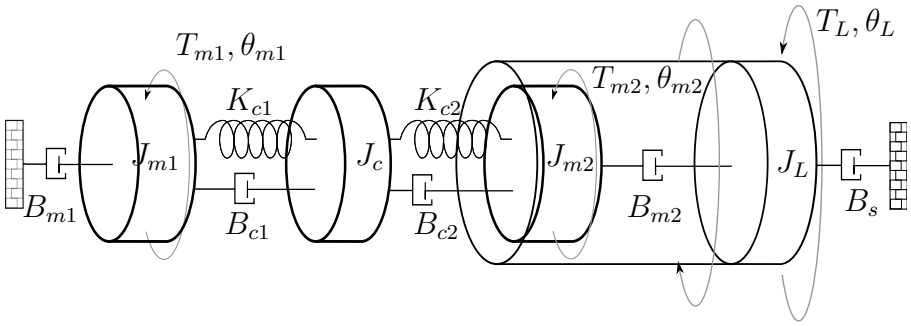

Figure 4.5: Lumped inertia model - the proposed dual drive actuator

4.2.1 Primary stage

In the proposed actuator, the primary drive is attached to ground and hence the inertia of its stator may be treated as infinite. Due to the construction of electric

motors, friction arises from a number of sources including armature bearings and brushes that contact the commutator. These effects may be treated as the single friction term B_{m1}. The armature current induces torque over the rotor inertia J_{m1}.

The rotor of the primary drive is coupled to the rotor of the secondary drive. There are a number of ways to achieve this. When the actuator is constructed from discrete drives, the coupling may be made using an Oldham coupler, a helical coupler or a number of other possible means. Common to these methods of coupling is the presence of finite stiffness and damping, as included in Fig. 4.5. It is however possible to manufacture the two rotors on the same shaft, which leads to a very high stiffness and a lack of damping. The choice of coupling therefore has an impact on the complexity of the mathematical model as described below.

4.2.2 Secondary stage

The rotor of the secondary drive is coupled to that of the primary and the stator is attached to the load. Similar to the primary drive, friction is present between the rotor and stator and is treated as the single friction term B_{m2}. The armature current develops torque on the rotor inertia J_{m2} and an equal and opposite torque is applied to the stator and hence the load. If the assembly requires support, a bearing must be present between ground and the load with friction B'_s.

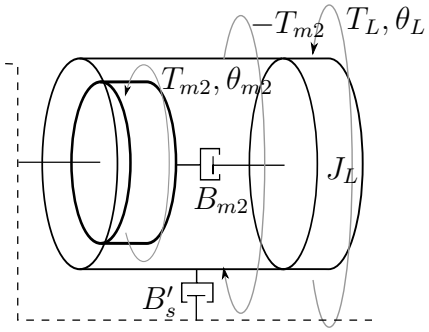

Figure 4.6: Lumped inertia model - Secondary drive only

Fig. 4.6 shows the isolated secondary drive, as regardless of the complexity of

the overall mathematical model due to the variations in the means of rotor coupling, this stage remains unaffected. The isolation boundary represents the points at which a single drive may be connected to linkages. In this case, the rotor may be attached to ground, and the stator to the link. $\dot{\theta}_L$ should be treated as relative motion to the isolation reference frame.

A mathematical model of this actuator is given as

$$\ddot{\theta}_L = \frac{1}{J_L}\left(-B_{m2}\dot{\theta}_L - B_s\dot{\theta}_L - T_{m2} + T_L\right) \tag{4.4}$$

The arrangement shown in Fig. 4.6 is equivalent to single drive actuators, hence exhibit the same limitations with respect to friction. In the case where the rotor is coupled to ground, $\dot{\theta}_L = -\dot{\theta}_{m2}$. In this arrangement, as $\dot{\theta}_L$ traverses the low velocity $\dot{\theta} \to 0$ region, the friction torque produced by B_{m2} and B_s also exhibits its characteristic discontinuous behaviour.

However, as in the proposed actuator, the rotor may be attached to a rotating inertia with non-zero velocity. When $(\dot{\theta}_{m2} - \dot{\theta}_L)$ is sufficiently large as to clear the non-linear domain, friction can be treated as purely viscous in nature. $\dot{\theta}_L$ as referenced to the stator of the primary drive may take on any value - including zero - without encountering the non-linear friction domain.

4.3 Actuator modelling

As described earlier, there is a requirement to couple the rotors of the two drives. Based on the method of coupling, a number of different models may be derived, which are presented in order of complexity. The most comprehensive model is also the most difficult to parameterise and assess for stability, however as it fully describes the proposed DDA.

4.3.1 Four degree-of-freedom model

The differential equations describing the system in Fig. 4.5 can be derived by inspecting the individual components of the system. For the sake of completeness, the electrical equations are also presented here.

Primary drive (grounded):

$$\begin{aligned} v_{m1} &= R_{a1} i_1 + L_{a1} \frac{di_1}{dt} + K_{a1} \dot{\theta}_{m1} \\ \frac{di_1}{dt} &= -\frac{R_{a1}}{L_{a1}} i_1 - \frac{K_{a1}}{L_{a1}} \dot{\theta}_{m1} + \frac{v_{m1}}{L_{a1}} \end{aligned} \tag{4.5a}$$

$$\begin{aligned} T_{m1} &= J_{m1} \ddot{\theta}_{m1} + B_{m1} \dot{\theta}_{m1} + \frac{1}{r_1}\left(\frac{1}{r_1} B_{c1} \dot{\theta}_{m1} + \frac{1}{r_1} K_{c1} \theta_{m1}\right) - \frac{1}{r_1}\left(B_{c1} \dot{\theta}_c + K_{c1} \theta_c\right) \\ \ddot{\theta}_{m1} &= -\frac{B_{m1} + \frac{1}{r_1^2} B_{c1}}{J_{m1}} \dot{\theta}_{m1} - \frac{K_{c1}}{r_1^2 J_{m1}} \theta_{m1} + \frac{B_{c1}}{r_1 J_{m1}} \dot{\theta}_c + \frac{K_{c1}}{r_1 J_{m1}} \theta_c + \frac{T_{m1}}{J_{m1}} \end{aligned} \tag{4.5b}$$

Coupling of the two rotors:

$$\begin{aligned} 0 &= J_c \ddot{\theta}_c + B_{c1} \dot{\theta}_c + K_{c1} \theta_c + B_{c2} \dot{\theta}_c + K_{c2} \theta_c - B_{c1} \frac{\dot{\theta}_{m1}}{r_1} - K_{c1} \frac{\theta_{m1}}{r_1} - B_{c2} \frac{\dot{\theta}_{m2}}{r_2} - K_{c2} \frac{\theta_{m2}}{r_2} \\ \ddot{\theta}_c &= -\frac{B_{c1} + B_{c2}}{J_c} \dot{\theta}_c - \frac{K_{c1} + K_{c2}}{J_c} \theta_c + \frac{B_{c1}}{r_1 J_c} \dot{\theta}_{m1} + \frac{B_{c2}}{r_2 J_c} \dot{\theta}_{m2} + \frac{K_{c1}}{r_1 J_c} \theta_{m1} + \frac{K_{c2}}{r_2 J_c} \theta_{m2} \end{aligned} \tag{4.6a}$$

Secondary drive:

$$v_{m2} = R_{a2} i_2 + L_{a2} \frac{di_2}{dt} + K_{a2} \dot{\theta}_{m2}$$
$$\frac{di_2}{dt} = -\frac{R_{a2}}{L_{a2}} i_2 - \frac{K_{a2}}{L_{a2}} \dot{\theta}_{m2} + \frac{v_{m2}}{L_{a2}} \tag{4.7a}$$

$$T_{m2} = J_{m2} \ddot{\theta}_{m2} + B_{m2} \dot{\theta}_{m2} + \frac{1}{r_2}(\frac{1}{r_2} B_{c2} \dot{\theta}_{m2} + \frac{1}{r_2} K_{c2} \theta_{m2}) - \frac{1}{r_2}(B_{c2} \dot{\theta}_c + K_{c2} \theta_c) - r_2 B_{m2} \dot{\theta}_L$$
$$\ddot{\theta}_{m2} = -\frac{B_{c2} + \frac{1}{r_2^2} B_{m2}}{J_{m2}} \dot{\theta}_{m2} - \frac{K_{c2}}{r_2^2 J_{m2}} \theta_{m2} + \frac{B_{c2}}{r_2 J_{m2}} \dot{\theta}_c + \frac{K_{c2}}{r_2 J_{m2}} \theta_c + \frac{r_2 B_{m2}}{J_{m2}} \dot{\theta}_L + \frac{T_{m2}}{J_{m2}} \tag{4.7b}$$

Load:

$$-r_2 T_{m2} + T_L = J_L \ddot{\theta}_L + B_s \dot{\theta}_L + \frac{1}{r_2} B_{m2} \dot{\theta}_L - \frac{1}{r_2^2} B_{m2} \dot{\theta}_{m2}$$
$$\ddot{\theta}_L = -\frac{\frac{1}{r_2} B_{m2} + B_s}{J_L} \dot{\theta}_L + \frac{B_{m2}}{r_2^2 J_L} \dot{\theta}_{m2} - r_2 \frac{T_{m2}}{J_L} + \frac{T_L}{J_L} \tag{4.8a}$$

These equations may be represented in state space form as

$$\dot{\mathbf{x}} = \mathbf{A}\mathbf{x} + \mathbf{B}\mathbf{u}$$

$$\mathbf{y} = \mathbf{C}\mathbf{x} + \mathbf{D}\mathbf{u}$$

, where $\mathbf{x} = \begin{bmatrix} \theta_{m1} & \dot{\theta}_{m1} & \theta_c & \dot{\theta}_c & \theta_{m2} & \dot{\theta}_{m2} & \theta_L & \dot{\theta}_L \end{bmatrix}'$, then

$$\mathbf{A} = \begin{bmatrix} 0 & 1 & 0 & 0 & 0 & 0 & 0 & 0 \\ -\frac{K_{c1}}{r_1^2 J_{m1}} & -\frac{B_{m1}+\frac{1}{r_1^2}B_{c1}}{J_{m1}} & \frac{K_{c1}}{r_1 J_{m1}} & \frac{B_{c1}}{r_1 J_{m1}} & 0 & 0 & 0 & 0 \\ 0 & 0 & 0 & 1 & 0 & 0 & 0 & 0 \\ \frac{K_{c1}}{r_1 J_c} & \frac{B_c}{r_1 J_c} & -\frac{K_{c1}+K_{c2}}{J_c} & -\frac{B_{c1}+B_{c2}}{J_c} & \frac{K_{c2}}{r_2 J_c} & \frac{B_{c2}}{r_2 J_c} & 0 & 0 \\ 0 & 0 & 0 & 0 & 0 & 1 & 0 & 0 \\ 0 & 0 & \frac{K_{c2}}{r_2 J_{m2}} & \frac{B_{c2}}{r_2 J_{m2}} & -\frac{K_{c2}}{r_2^2 J_{m2}} & -\frac{B_{c2}+\frac{1}{r_2^2}B_{m2}}{J_{m2}} & 0 & \frac{r_2 B_{m2}}{J_{m2}} \\ 0 & 0 & 0 & 0 & 0 & 0 & 0 & 1 \\ 0 & 0 & 0 & 0 & 0 & \frac{B_{m2}}{r_2^2 J_L} & 0 & -\frac{\frac{1}{r_2}B_{m2}+B_s}{J_L} \end{bmatrix}$$

$$\mathbf{B} = \begin{bmatrix} 0 & 0 & 0 \\ \frac{1}{J_{m1}} & 0 & 0 \\ 0 & 0 & 0 \\ 0 & 0 & 0 \\ 0 & 0 & 0 \\ 0 & \frac{1}{J_{m2}} & 0 \\ 0 & 0 & 0 \\ 0 & -\frac{r_2}{J_L} & \frac{1}{J_L} \end{bmatrix} \quad \mathbf{C} = \begin{bmatrix} 1 & 0 & 0 & 0 & 0 & 0 & 0 & 0 \\ 0 & 1 & 0 & 0 & 0 & 0 & 0 & 0 \\ 0 & 0 & 0 & 0 & 1 & 0 & 0 & 0 \\ 0 & 0 & 0 & 0 & 0 & 1 & 0 & 0 \\ 0 & 0 & 0 & 0 & 0 & 0 & 1 & 0 \\ 0 & 0 & 0 & 0 & 0 & 0 & 0 & 1 \end{bmatrix} \quad \mathbf{D} = 0$$

, and $\mathbf{u} = \begin{bmatrix} T_{m1} & T_{m2} & T_L \end{bmatrix}'$.

It is worth noting that by choosing motors of the same characteristics and gear ratio, $J_{m1} = J_{m2}$, $B_{m1} = B_{m2}$, $L_{a1} = L_{a2}$, $K_{a1} = K_{a2}$ and $R_{a1} = R_{a2}$.

To study the stability of the system, the eigenvalues of the system matrix $\mathbf{A}$ should be computed. Achieving this algebraically on such a high order matrix has its difficulties. Tools such as MATLAB Symbolic Toolbox are capable of computing the expressions, however these results are of little use due to their extreme length and complexity. Numerical analysis with a range of values representative of the system yield a set of eigenvalues for each iteration. These sets are shown in Fig. A.1 in the Appendix. The histograms capture the nature of each eigenvalue as the parameters change, and it can be seen that none are positive. As the eigenvalues cover a large

range of multiple orders of magnitude, rounding errors accumulate and disperse the zero in Fig. A.1b. Eigenvalues 2,3 and 4,5 form complex conjugate pairs, hence the figures showing only the real parts appear identical.

As mentioned earlier, the nature of the coupling has a direct impact on the complexity of the model. If the coupling mechanism is assumed to have negligible inertia when compared to the rotor inertias, a simpler model is adequate to describe the system, as derived below.

4.3.2 Three degree-of-freedom model

By assuming that the coupling inertia $J_c \ll (J_{m1} + J_{m2})$, the two stiffness and damping terms may be folded into single stiffness and damping between the two rotor inertias, and a 3 degree-of-freedom model can also be derived as shown in Fig. 4.7. This model captures the dynamics of the load and both rotors individually.

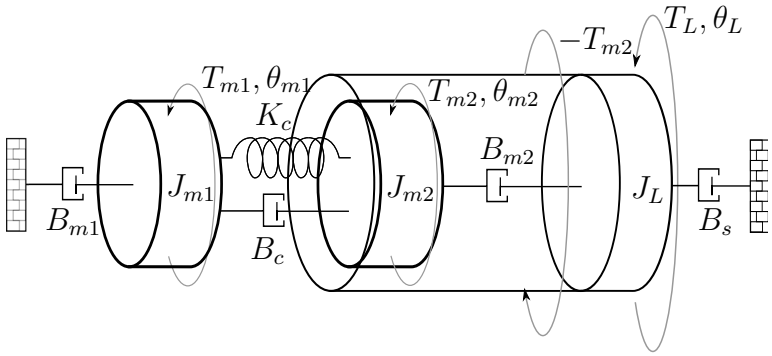

Figure 4.7: Lumped inertia model - 3 degrees of freedom

The balancing of torques gives

$$T_{m1} + B_c\dot{\theta}_{m2} + K_c\theta_{m2} = J_{m1}\ddot{\theta}_{m1} + B_{m1}\dot{\theta}_{m1} + B_c\dot{\theta}_{m1} + K_c\theta_{m1} \tag{4.9}$$

$$T_{m2} + B_c\dot{\theta}_{m1} + K_c\theta_{m1} + B_{m2}\dot{\theta}_L = J_{m2}\ddot{\theta}_{m2} + B_{m2}\dot{\theta}_{m2} + B_c\dot{\theta}_{m2} + K_c\theta_{m2} \tag{4.10}$$

$$-T_{m2} + T_L + B_{m2}\dot{\theta}_{m2} = J_L\ddot{\theta}_L + B_{m2}\dot{\theta}_L + B_s\dot{\theta}_L \tag{4.11}$$

By choosing the state vector as the position and velocity of each lumped inertia, the state equations may then be derived by rearranging the above

$$\ddot{\theta}_{m1} = -\frac{B_{m1} + B_c}{J_{m1}}\dot{\theta}_{m1} - \frac{K_c}{J_{m1}}\theta_{m1} + \frac{B_c}{J_{m1}}\dot{\theta}_{m2} + \frac{K_c}{J_{m1}}\theta_{m2} + \frac{T_{m1}}{J_{m1}} \tag{4.12}$$

$$\ddot{\theta}_{m2} = -\frac{B_{m2} + B_c}{J_{m2}}\dot{\theta}_{m2} - \frac{K_c}{J_{m2}}\theta_{m2} + \frac{B_c}{J_{m2}}\dot{\theta}_{m1} + \frac{K_c}{J_{m2}}\theta_{m1} + \frac{B_{m2}}{J_{m2}}\dot{\theta}_L + \frac{T_{m2}}{J_{m2}} \tag{4.13}$$

$$\ddot{\theta}_L = -\frac{B_{m2} + B_s}{J_L}\dot{\theta}_L + \frac{B_{m2}}{J_L}\dot{\theta}_{m2} - \frac{T_{m2}}{J_L} + \frac{T_L}{J_L} \tag{4.14}$$

Let the state vector $\mathbf{x} = \begin{bmatrix}\theta_{m1} & \dot{\theta}_{m1} & \theta_{m2} & \dot{\theta}_{m2} & \theta_L & \dot{\theta}_L\end{bmatrix}'$.

Equations (4.12 - 4.14) can then be substituted into the state space **A** matrix as

$$\begin{bmatrix} 0 & 1 & 0 & 0 & 0 & 0 \\ -\frac{K_c}{J_{m1}} & -\frac{B_{m1}+B_c}{J_{m1}} & \frac{K_c}{J_{m1}} & \frac{B_c}{J_{m1}} & 0 & 0 \\ 0 & 0 & 0 & 1 & 0 & 0 \\ \frac{K_c}{J_{m2}} & \frac{B_c}{J_{m2}} & -\frac{K_c}{J_{m2}} & -\frac{B_c+B_{m2}}{J_{m2}} & 0 & \frac{B_{m2}}{J_{m2}} \\ 0 & 0 & 0 & 0 & 0 & 1 \\ 0 & 0 & 0 & \frac{B_{m2}}{J_L} & 0 & -\frac{B_{m2}+B_s}{J_L} \end{bmatrix}$$

The eigenvalues of the **A** matrix are the open-loop system poles. The simplified form of the otherwise complex expressions are

$$\lambda_{1,2} = 0$$
$$\lambda_{3,4} = -\frac{B_c + B_{m1}}{2J_{m1}} - \frac{B_{m2} + B_s}{4J_L} - C \pm D$$
$$\lambda_{5,6} = -\frac{B_c + B_{m1}}{2J_{m1}} - \frac{B_{m2} + B_s}{4J_L} + C \pm D$$

, where C and D are expressions that are a result of factorisation of the eigenvalue equations. Symbolic analysis for assessment of stability of this system, like the four degree of freedom model, is still a challenge. Expressions C and D are too complex to draw conclusions from and numerical analysis will yield results in line with those for the earlier model. However, the system matrix $\mathbf{A}$ may be further simplified if the coupling stiffness is treated as the torsional stiffness of a solid, combined rotor and yields to a simpler, two degree of freedom model, which has eigenvalues that can be readily found algebraically.

4.3.3 Two degree-of-freedom model

By assuming that the coupling stiffness is infinite and treating the rotors as a single entity, the following velocities may be defined: $\dot{\theta}_m = \dot{\theta}_{m1}$ and $\dot{\theta}_L = \dot{\theta}_{m2} - \dot{\theta}_{m1}$.

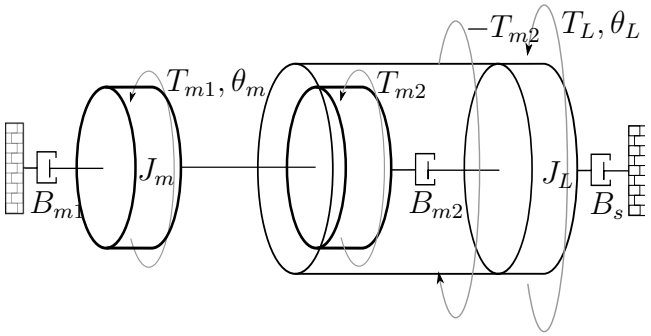

Figure 4.8: Lumped inertia model - 2 degrees of freedom

This model assumes that inertia of the two rotors and the coupler can be lumped into a single inertia J_m. This model provides the foundation for the mathematical models for the dual drive actuator or DDA.

The resultant model as shown in Fig. 4.8 can be described mathematically as

$$T_{m1} + T_{m2} + B_{m2}\dot{\theta}_L = J_m\ddot{\theta}_m + B_{m1}\dot{\theta}_m + B_{m2}\dot{\theta}_m \tag{4.15}$$

$$-T_{m2} + T_L + B_{m2}\dot{\theta}_m = J_L\ddot{\theta}_L + B_s\dot{\theta}_L + B_{m2}\dot{\theta}_L \tag{4.16}$$

This 2 degree-of-freedom (DoF) model allows for precursory investigation into the performance of the secondary drive, and hence the friction behaviour experienced by the load.

By choosing the state vector as the position and velocity of each lumped inertia, the state equations may then be derived by rearranging the above

$$\ddot{\theta}_m = -\frac{B_{m1} + B_{m2}}{J_m}\dot{\theta}_m + \frac{B_{m2}}{J_m}\dot{\theta}_L + \frac{T_{m1}}{J_m} + \frac{T_{m2}}{J_m} \tag{4.17}$$

$$\ddot{\theta}_L = -\frac{B_{m2} + B_s}{J_L}\dot{\theta}_L + \frac{B_{m2}}{J_L}\dot{\theta}_m - \frac{T_{m2}}{J_L} + \frac{T_L}{J_L} \tag{4.18}$$

These equations can now be rewritten in state space form, as

$$\dot{\mathbf{x}} = \mathbf{A}\mathbf{x} + \mathbf{B}\mathbf{u}$$

$$\mathbf{y} = \mathbf{C}\mathbf{x} + \mathbf{D}\mathbf{u}$$

$$\begin{bmatrix} \dot{\theta}_m \\ \theta_m \\ \theta_L \\ \theta_L \end{bmatrix} = \begin{bmatrix} 0 & 1 & 0 & 0 \\ 0 & -\frac{B_{m1}+B_{m2}}{J_m} & 0 & \frac{B_{m2}}{J_m} \\ 0 & 0 & 0 & 1 \\ 0 & \frac{B_{m2}}{J_L} & 0 & -\frac{B_s+B_{m2}}{J_L} \end{bmatrix} \begin{bmatrix} \theta_m \\ \dot{\theta}_m \\ \theta_L \\ \dot{\theta}_L \end{bmatrix} + \begin{bmatrix} 0 & 0 \\ \frac{1}{J_m} & \frac{1}{J_m} \\ 0 & 0 \\ 0 & -\frac{1}{J_L} \end{bmatrix} \begin{bmatrix} T_{m1} \\ T_{m2} \end{bmatrix} \tag{4.19}$$

$$\mathbf{y} = \begin{bmatrix} 1 & 0 & 0 & 0 \\ 0 & 1 & 0 & 0 \\ 0 & 0 & 1 & 0 \\ 0 & 0 & 0 & 1 \end{bmatrix} \begin{bmatrix} \theta_m \\ \dot{\theta}_m \\ \theta_L \\ \dot{\theta}_L \end{bmatrix} + 0 \begin{bmatrix} T_{m1} \\ T_{m2} \end{bmatrix} \tag{4.20}$$

To assess stability, the eigenvalues must be found by $|\lambda\mathbf{I} - \mathbf{A}| = 0$. This yields

$$\lambda^2((\lambda + \frac{B_{m1} + B_{m2}}{J_m})(\lambda + \frac{B_s + B_{m2}}{J_L}) - (\frac{B_{m2}}{J_m} \cdot \frac{B_{m2}}{J_L})) = 0$$

It follows that

$$\lambda_{1,2} = 0$$

and

$$\lambda_{3,4} = \text{roots}((\lambda + \frac{B_{m1} + B_{m2}}{J_m})(\lambda + \frac{B_s + B_{m2}}{J_L}) - (\frac{B_{m2}}{J_m} \cdot \frac{B_{m2}}{J_L}))$$

Expanding the quadratic, the roots will be guaranteed negative when all coefficients are positive. Hence

$$\lambda^2 + \lambda(\frac{B_{m1} + B_{m2}}{J_m} + \frac{B_s + B_{m2}}{J_L}) + (\frac{B_{m1} + B_{m2}}{Jm} \cdot \frac{B_s + B_{m2}}{J_L} - \frac{B_{m2}^2}{J_m J_L}) = 0$$

As all system parameters are positive,

$$\frac{B_{m1} + B_{m2}}{J_m} + \frac{B_s + B_{m2}}{J_L} > 0$$

and

$$\frac{B_{m1} + B_{m2}}{Jm} \cdot \frac{B_s + B_{m2}}{J_L} - \frac{B_{m2}^2}{J_m J_L} > 0$$

$$(B_{m1} + B_{m2})(B_s + B_{m2}) > B_{m2}^2$$

$$B_{m1}B_s + B_{m2}(B_{m1} + B_s) > 0$$

These inequalities always hold true and hence all four eigenvalues are non-positive.

4.3.4 Suitable friction models

In order to avoid the non-linear regions of friction present within the actuator when $|\dot{\theta}_L| < \epsilon$, the velocities of both motors have to exceed the Stribeck velocity region

and be of constant sign. In this regime - as the motors are not allowed to reverse in velocity - the effective maximum output velocity is therefore that of a single drive actuator. The friction terms B_{m1}, B_{m2} and B_s may be modelled using any of the previously discussed friction models. However, by considering the velocities present in the actuator, it can be seen that a combined Coulomb and viscous model will suffice for both B_{m1} and B_{m2}, as $|\dot{\theta}_m| > 0$ and $|\dot{\theta}_m - \dot{\theta}_L| > 0$. This is because the motion of a single drive is confined to a velocity that is clear of the Stribeck region and is purely viscous (but offset by the Coulomb coefficient).

In the case of B_s, which represents friction arising in the support bearing of the link, a simple Coulomb and viscous model will not suffice. This is due to the nature of the output link velocity that may traverse the stationary region, hence discontinuous friction models are necessary. Model (2.8) is used for this purpose throughout simulation in the next chapter. This model is flexible as it allows for the Stribeck effect, but also captures friction behaviour near the zero velocity region. Its implementation also overcomes the difficulties that arise when simulating discontinuous friction models. A stiff solver, such as *ode15s*, is required when the solution of interest changes on a longer time scale, but the solutions change on a time scale that is very much smaller when compared to the interval of integration [107]. Friction models incorporating a form of Coulomb friction belong to this category, as their effect make very fast changes to the solution, however the overall dynamics is dictated by viscous friction acting over all solutions.

4.3.5 Torque production

The DDA is comprised of two drives and hence the means of output torque production must be investigated.

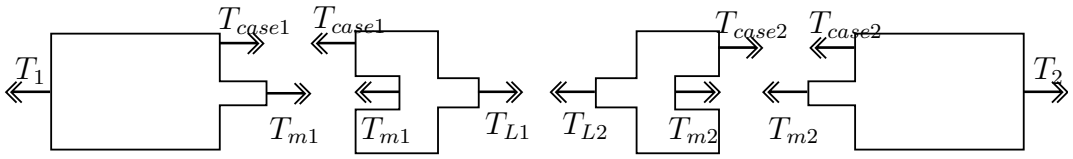

Figure 4.9: Subsystem analysis of torque production

By using subsystem analysis, the torque propagation shown below can be described as:

$$T_1 = T_{case1} + T_{m1} \qquad T_2 = T_{case2} + T_{m2}$$
$$T_{L1} = T_{case1} + T_{m1} \qquad T_{L2} = T_{case2} + T_{m2}$$

Including the effect of the gear-train: $T_{L_i} = r_i T_{m_i}$, in a static case, $T_{L1} = T_1$ and $T_{L2} = T_2$. If T_2 is considered as the output and $T_{m1} = T_{m2}$ then the following holds:

$$T_2 = T_{L2} = -T_{L1} = -T_1 \tag{4.22}$$

This result shows that the torque production is limited to that of a single drive actuator (motor and gearbox combination) and is limited by the 'weakest link' characteristics. For this reason it is beneficial to select drives with similar parameters.

4.4 Summary

This chapter introduces the concept behind the proposed actuator design and presents the formulae which describe the system behaviour. A 4 DoF model is derived first, however it is impractical to assess its stability by finding the eigenvalues of the system matrix **A**. Instead, simplification can be made by assuming that the coupling inertia is negligibly small. The 3 DoF model, although simpler, still captures the behaviour of the DDA yet its stability still cannot be assessed algebraically. A further assumption

of very high coupling stiffness between the two rotors yield a further simplified, 2 DoF model which is shown to be stable algebraically.

Although the DDA combines two single drives, it is shown that this particular series configuration results in an overall torque production of that of a single drive.

Chapter 5

Simulation study

This chapter initially demonstrates that the combined Coulomb and viscous friction model is sufficient at capturing non-linearities which the DDA is capable of linearising. The theoretical Coulomb model is compared with simulation results, following which all DDA mathematical models are simulated using that friction model.

5.1 Simulation parameters and motor properties

Common to all models are the drive characteristics, as shown in Table 5.1. As the physical system is constructed using harmonic drive geared motors, the motor properties reflect the effects of the gearbox.

Table 5.1: Motor parameters

Symbol	Parameter	Value	Unit
J_m	Rotor inertia	$5e^{-4}$	kgm^2
K	Motor constant	2.48	V/rad/s
La	Armature inductance	1.60	mH
Ra	Armature resistance	4.70	Ω
b	Rotor viscous friction coefficient	$3.5e^{-3}$	Ns/rad
C	Rotor Coulomb friction level	$3e^{-2}$	Nm
$\dot{\theta}_{th}$	Rotor friction model velocity threshold	$1e^{-3}$	rad/s

The friction model velocity threshold values are selected such that the simulation time steps will occur within the period of transition. Too small a value results in the solver reducing the time steps of the simulation to unacceptably small levels. The support bearing and load parameters are presented in Table 5.3. To gain an insight into the system, certain coefficients are assigned significantly larger than average values. This is a deliberate choice to highlight certain effects which arise in practice.

The simulations require a number of key motor parameters. The inertia of the stator is a quantity that is not provided by the manufacturer, hence this is calculated here. A representative load inertia of a cantilever is also then derived.

The following table summarises key parameters of a Maxon RE 25 motor that are used in the simulations. Some parameters are converted to SI units as required by the simulations.

Table 5.2: Physical parameters for Maxon p/n 118743

Symbol	Parameter	Value	Unit
	No load speed	507.89	rad/s
	No load current	0.026	A
	Stall torque	0.129	Nm
	Stall current	5.5	A
	Nominal speed	397.94	rad/s
	Nominal torque	0.028	Nm
	Nominal current	1.24	A
	Torque constant	$2.35 \cdot 10^{-2}$	Nm/A
K	Motor constant	0.0235	V/rad/s
J_m	Rotor inertia	$1.08 \cdot 10^{-6}$	kgm^2
	Motor mass	0.130	kg

The inertia along the long axis (J_x) of a hollow cylinder with inner radius a and outer radius b is

$$J_x = \frac{m(a^2 + b^2)}{2} \tag{5.1}$$

The inertia along the long axis (J_x) of a solid cylinder with radius r is

$$J_x = \frac{1}{2}mr^2 \tag{5.2}$$

Assuming that the rotor is a hollow cylinder with $a = 0.5$cm and $b = 0.65$cm, the mass of the rotor is calculated to be 30.93g. Added to this is an estimated further 5g for the rotor's axle. Hence, the mass of the stator is approximately 95g.

Assuming that the stator is a solid cylinder with radius $r = 1.25$cm, the inertia of the stator is approximately $1.85 \cdot 10^{-6}\text{kgm}^2$.

The load is attached to the stator of the secondary motor. In the simulations, the end of an aluminium bar is connected to the stator. The inertia about the short axis, rotation about the end of the rod, for this bar may be calculated using the following equation

$$J_{end} = \frac{\pi \rho r^2 l^3}{3} \tag{5.3}$$

Assuming the density $\rho = 2.7 \cdot 10^3 \text{kgcm}^{-3}$, the inertia of the link is approximately $2.86 \cdot 10^{-3}\text{kgm}^2$.

Table 5.3: Support bearing and load parameters

Symbol	Parameter	Value	Unit
C	Coulomb friction level	$2.56e^{-2}$	Nm
b	Viscous friction coefficient	$1e^{-6}$	Ns/rad
$\dot{\theta}_{th}$	Rotor friction model velocity threshold	$1e^{-3}$	rad/s
J_L	Load inertia	$2e^{-3}$	kgm^2

The applied load torque is a sinusoid of amplitude 0.1 Nm. This value was selected so that Coulomb friction may remain of reasonable value and the velocity of the output within orders of magnitude of the motor velocities. This of course is only the result of the chosen model parameters.

5.2 Friction model

Under ideal conditions, friction is considered to be linear and hence purely viscous in nature. If the sliding block as introduced earlier experiences viscous only friction, the

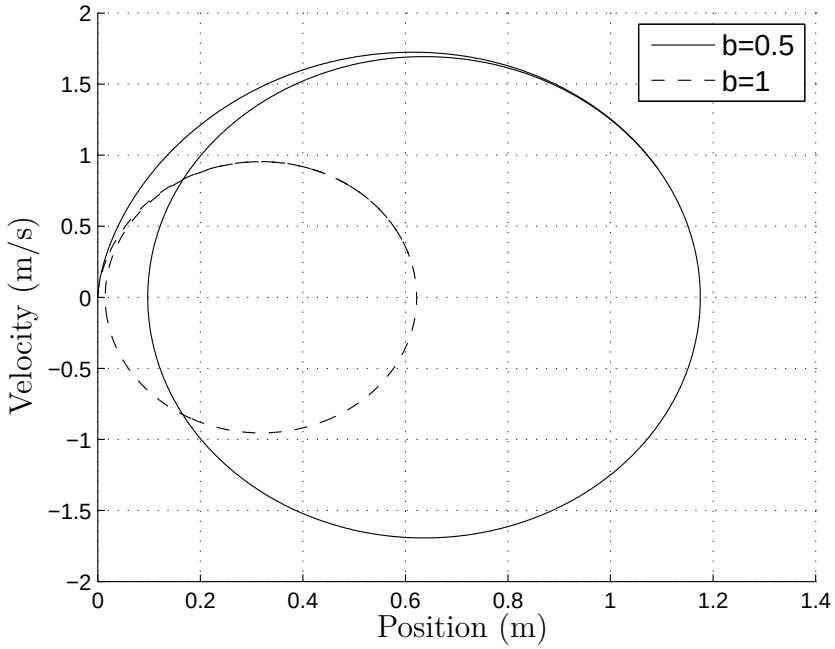

(a) Position/Velocity

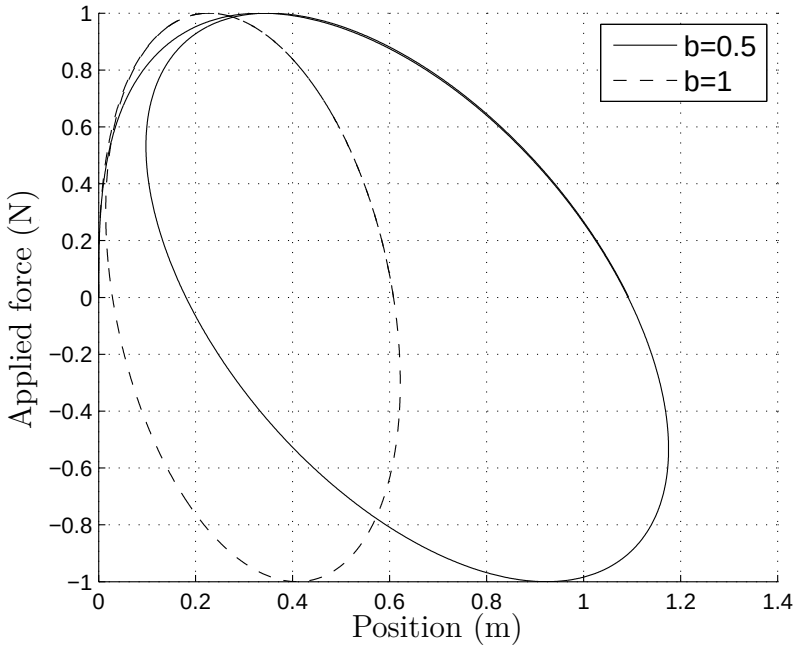

(b) Position/Applied force

Figure 5.1: Motion of a sliding block of mass $m = 0.1$kg, experiencing viscous only friction. The position of the block is compared against a) its velocity and b) the applied external force

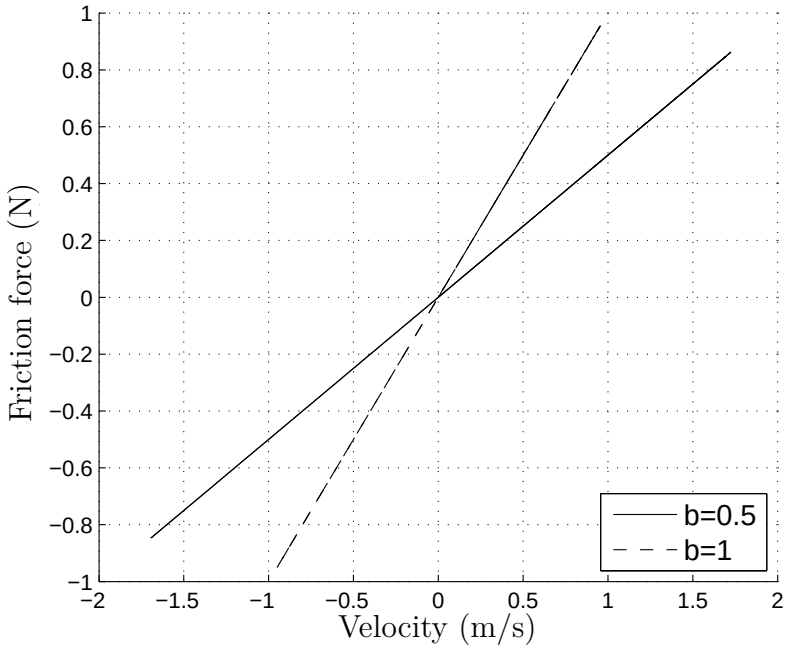

(a) Velocity/Friction force

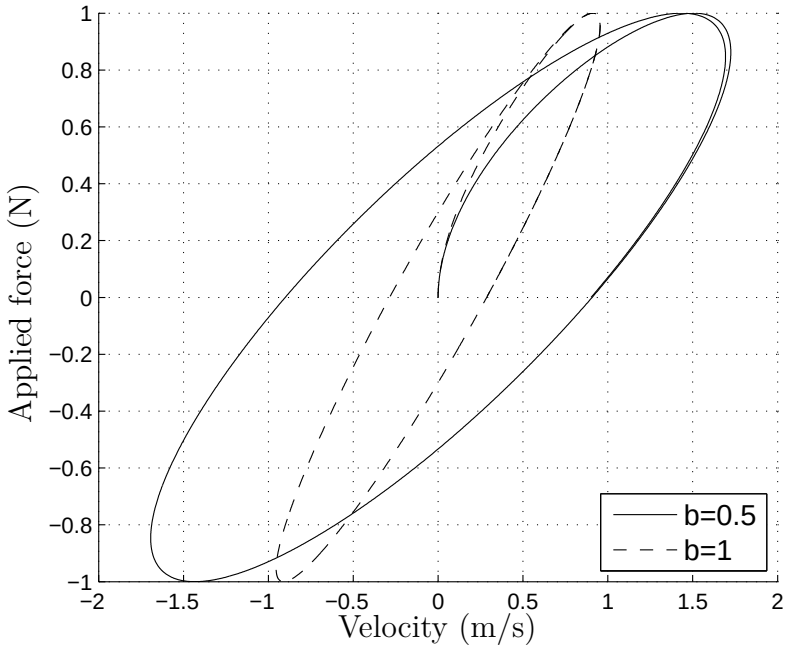

(b) Velocity/Applied force

Figure 5.2: Motion of a sliding block of mass $m = 0.1$kg, experiencing viscous only friction. The velocity of the block is compared against a) the produced viscous friction force and b) the applied external force

motion profile appears as shown in Figures 5.1 and 5.2. The equation governing the motion is given as

$$m\ddot{x} = f_a - b\dot{x}$$

where m is the mass of the block and b is the coefficient of viscous friction and f_a is the applied force.

It is apparent from Fig. 5.1a that the block undergoes linear motion and no discontinuities occur in its travel. This motion is also compared against the external force that results in the motion, as shown in Fig. 5.1b. The velocity of the block also experiences no discontinuities, as shown in Fig. 5.2b. The classic force-velocity gradient, characteristic of viscous only fiction is shown in Fig. 5.2a. Varying levels of viscous friction affects the trajectories such that the lower the value, the larger the velocity of the block may assume for the same force acting upon it.

In order to demonstrate how the theoretical and simulation friction models for the combined Coulomb and viscous model differ, again the sliding block analogy is utilised.

The block with mass m is resting on a surface with force f_a applied to it. As friction is present between the block and the surface, friction force f_c opposes the motion of the block.

$$\ddot{x} = \frac{1}{m}\left(f_a \mp f_c\right)$$

The applied force is a sinusoid and is described as $f_a = a \cdot sin(\omega t)$. If f_a is smaller than the Coulomb force, no motion will take place as the net force on the block will be zero. When f_a is sufficiently large so as to overcome f_c, the resultant net force f_r is no longer zero and the block will accelerate. The time when the block starts moving can be calculated using

$$t_c = \frac{1}{\omega} \sin^{-1}(\frac{C}{a})$$

where C is the constant value of Coulomb friction f_c. It is possible that the block will come to rest before the applied force reaches the Coulomb friction threshold of opposite polarity. This is shown in Fig. 5.3.

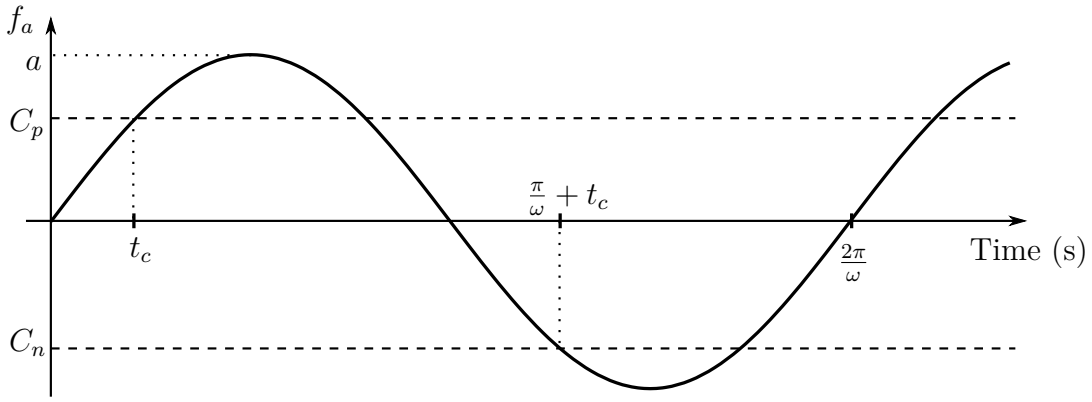

Figure 5.3: Simple Coulomb friction

In this case, after rescaling $\ddot{x}$ by $1/m$ and integrating from t_c to t, the velocity $\dot{x}$ is expressed as

$$\dot{x} = \frac{a}{\omega}(\cos(\omega t_c)) - \cos(\omega t)) \mp (Ct - Ct_c)$$

To find the position, integrating from t_c to t again yields

$$x = \frac{a}{\omega^2}(\sin(\omega t_c) - \sin(\omega t)) \mp \frac{C}{2}(t^2 - t_c^2) + \frac{a}{\omega}\cos(\omega t_c)(t - t_c) \pm Ct_c(t - t_c)$$

As previously, the sliding block has a number of characteristic phase plots that are of interest. The discontinuous nature of Coulomb friction is apparent in Fig. 5.4a, where the position of the block is shown to change in a non-linear fashion around zero velocity. This is expected as the block comes to a halt and takes a larger applied force before motion is resumed, as shown in Fig. 5.4b. The characteristic force-velocity phase plot of Coulomb friction is shown in Fig. 5.5a, whilst the non-linear nature of the velocity of the block is shown in Fig. 5.5b. The shape is highly characteristic of motion that experiences high levels of Coulomb friction.

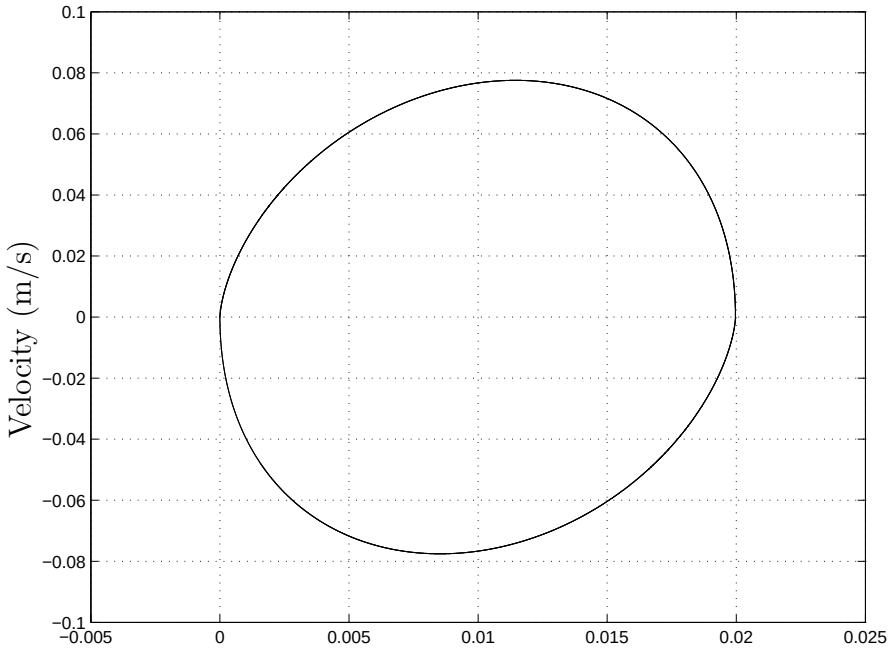

(a) Position/Velocity

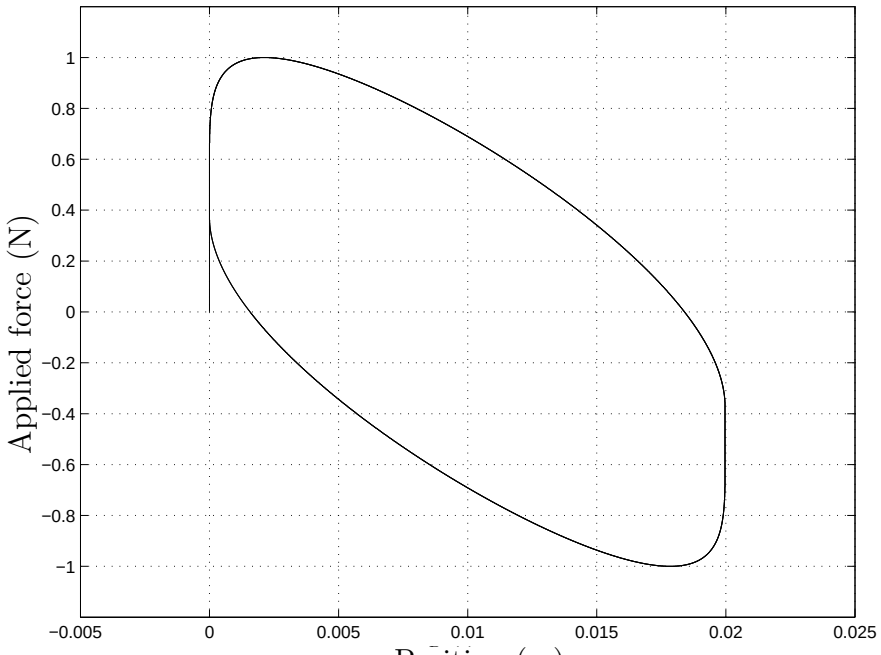

(b) Position/Applied force

Figure 5.4: Theoretical Coulomb friction behaviour

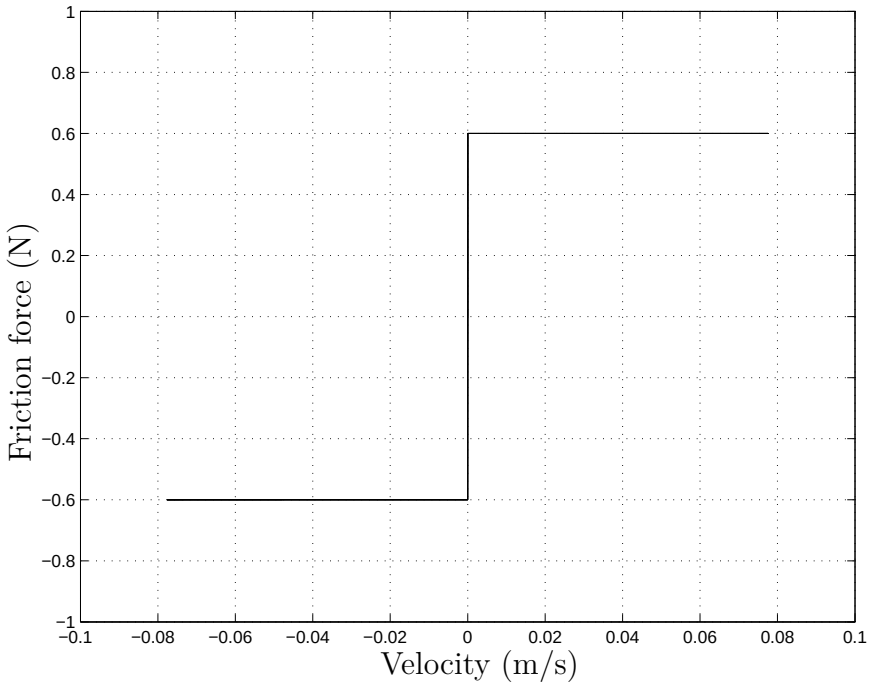

(a) Velocity/Friction force

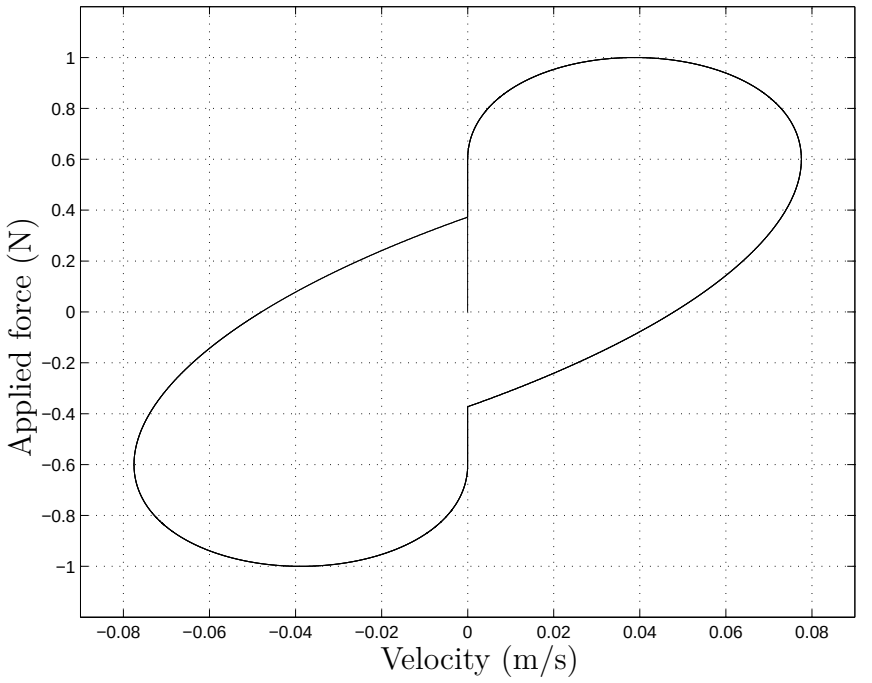

(b) Velocity/Applied force

Figure 5.5: Theoretical Coulomb friction behaviour

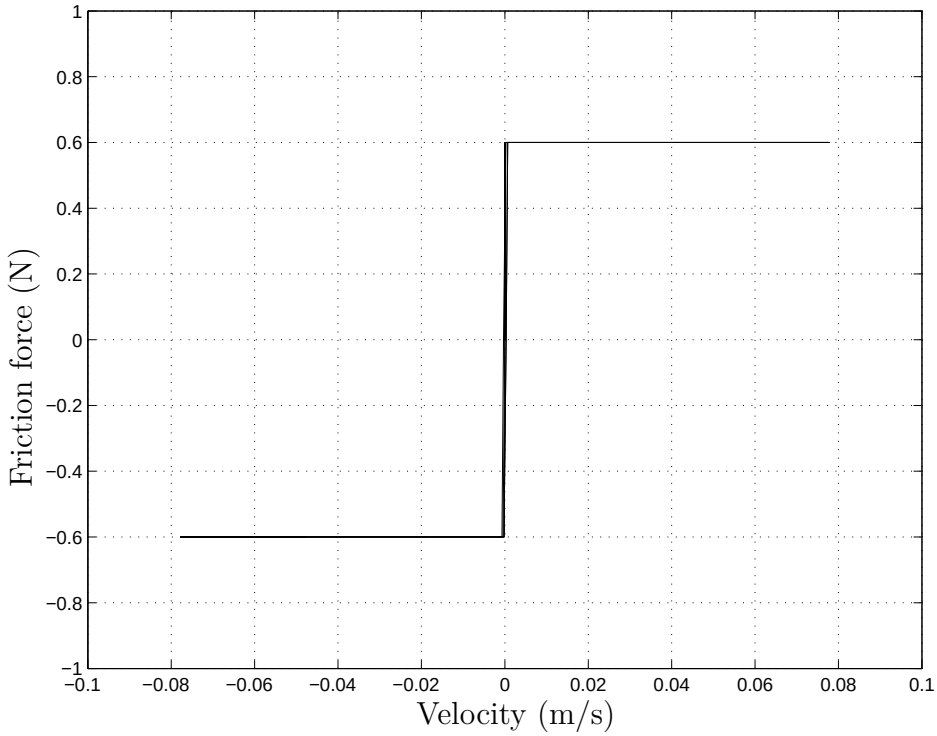

(a) Velocity/Friction force

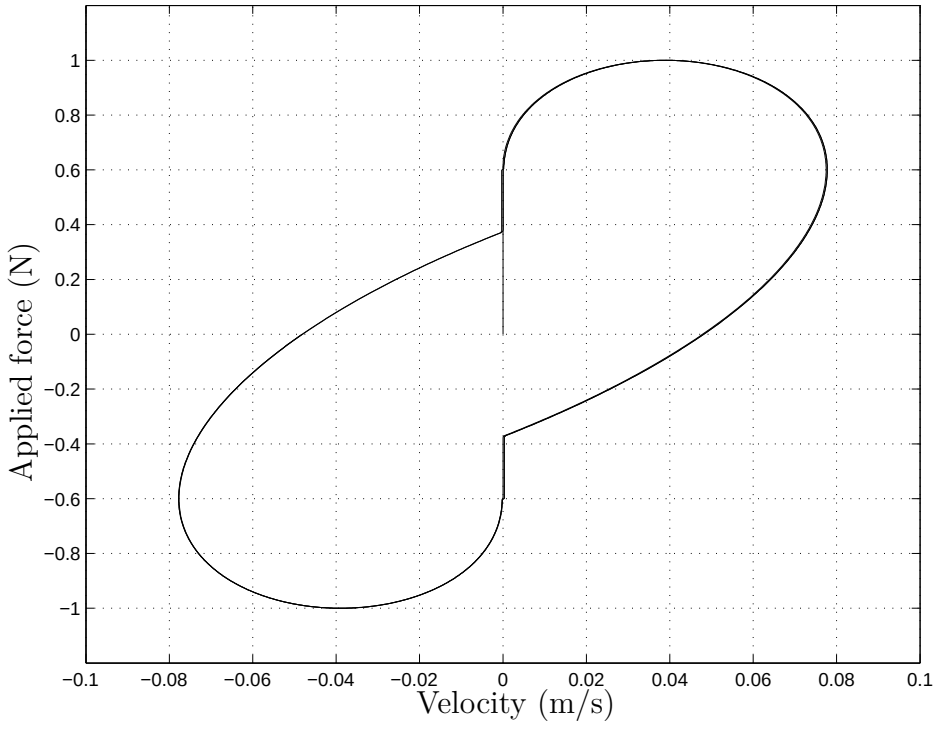

(b) Velocity/Applied force

Figure 5.6: Simulated Coulomb-only friction

For verification purposes, a simulation using classic Coulomb friction block in Simulink was also carried out. As shown in Fig. 5.6a the simulation of Coulomb only friction agrees with that obtained earlier shown in Fig. 5.5a. Similarly, Fig. 5.6b matches the theoretical behaviour of the sliding block, as shown in Fig. 5.5b.

The mathematical model matches the results of the simulation well. Possible emergence of chatter in simulation is due to the velocity dead-band introduced to overcome the difficulties in simulating the non-linear switch in the Coulomb function. This dead-band is generally included in simulations of Coulomb friction.

As was concluded in Chapter 3, for the purposes of this thesis it is sufficient to utilise a static friction model which incorporates Coulomb, viscous and Stribeck effects only. In order to aid the simulation, a continuous form of this combined model may be used in the following form

$$f_f(\dot{x}) = \begin{cases} (C + (F_s - C)e^{-s|\dot{x}|})\text{sign}(\dot{x}) + b\dot{x} & \text{if } |\dot{x}| \geq \dot{x}_{\text{th}} \\ \frac{\dot{x}}{\dot{x}_{\text{th}}}((C + (F_s - C)e^{-s\dot{x}_{\text{th}}}) + b\dot{x}_{\text{th}}) & \text{if } |\dot{x}| < \dot{x}_{\text{th}} \end{cases} \tag{5.4}$$

An external force acts upon a single block which experiences friction according to model (5.4). For comparison with Coulomb only friction, the same phase plots are presented in Figs. 5.7 and 5.8. The non-linear nature of model (5.4) is apparent in the position-velocity plot shown in Fig. 5.7a. The block again comes to a halt and only resumes motion once a sufficient external force is applied as shown in Fig. 5.7b. The characteristic force-velocity phase plot of the combined Coulomb-viscous-Stribeck friction model is shown in Fig. 5.8a, showing the discontinuity due to Coulomb friction, the decrease in friction force due to the Stribeck effect and finally the viscous only region. The velocity-applied force plot shown in Fig. 5.8b is comparable to that in Fig. 5.5b, having the same characteristic non-linear shape.

The model parameters are summarised in Table 5.4. Due to the very fast changes in the solution to the differential equations describing this model, a stiff solver is

required to deal with changes shorter than the integration time step. The solver *ode15s* is selected and used throughout this section as it is intended for such scenarios.

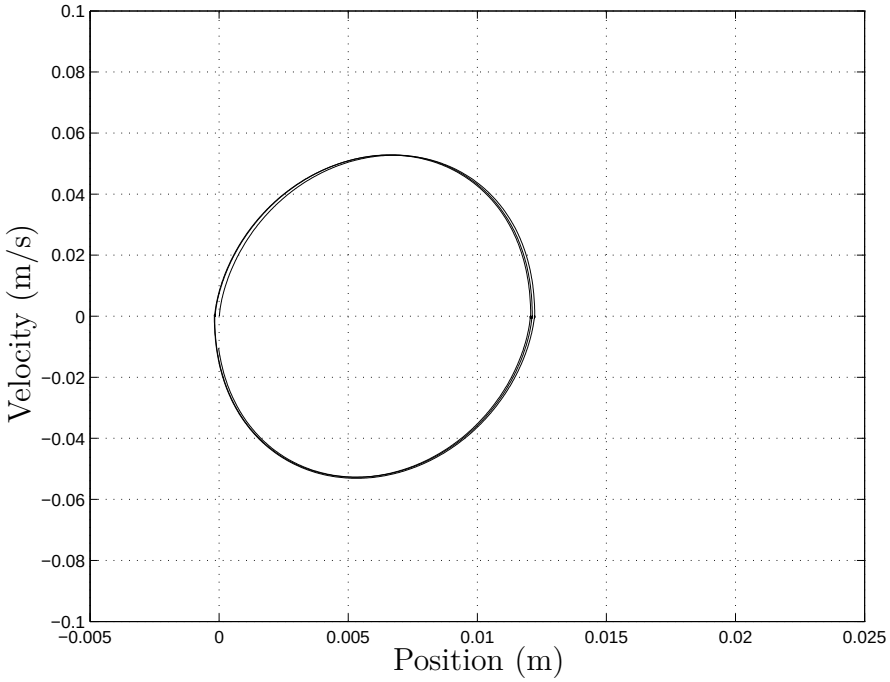

(a) Position/Velocity

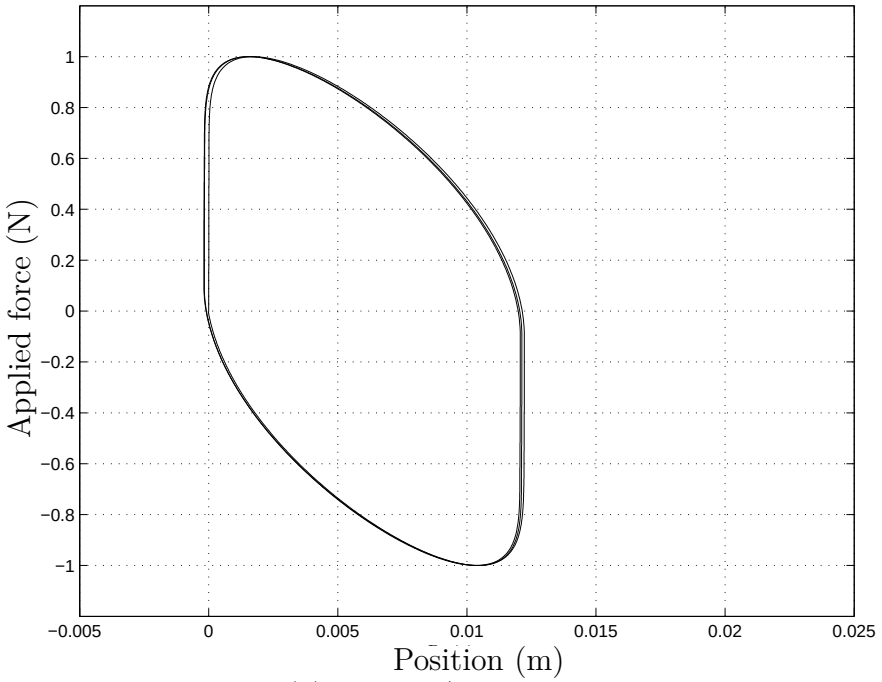

(b) Position/Applied force

Figure 5.7: Combined continuous Coulomb, viscous and Stribeck friction model

The model (5.4) captures the discontinuity near zero relative surface velocity

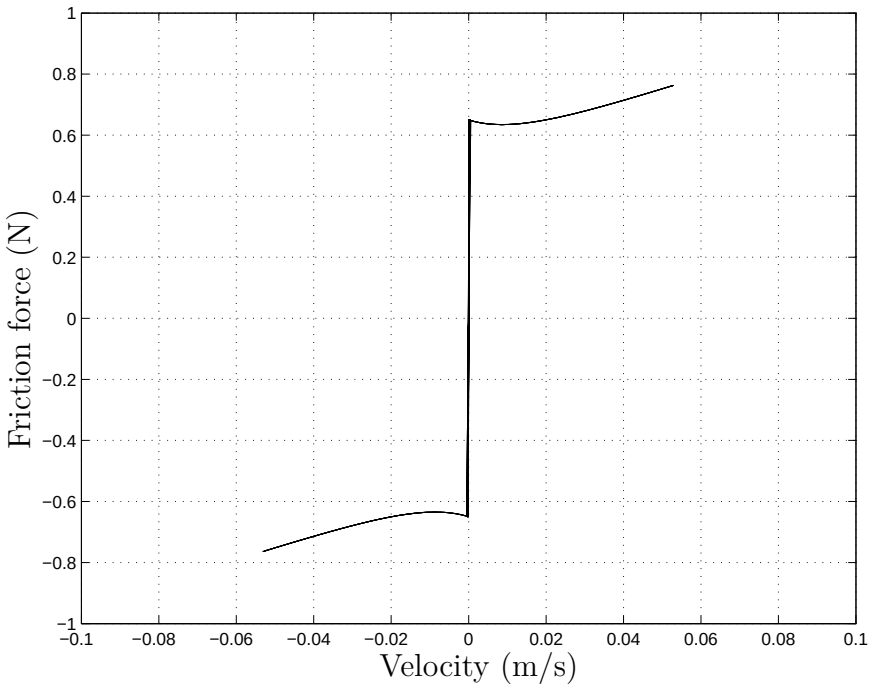

(a) Velocity/Friction force

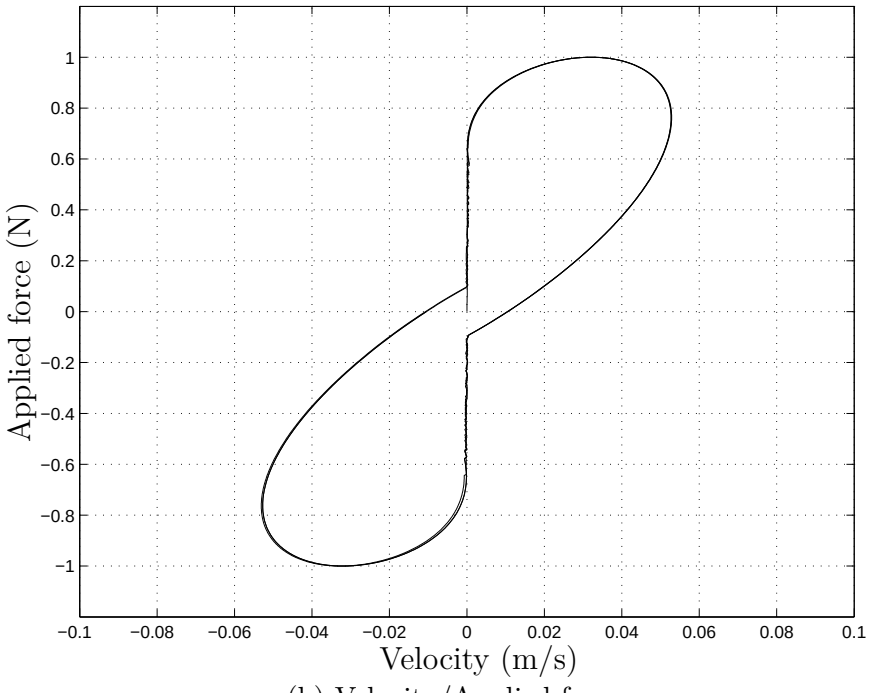

(b) Velocity/Applied force

Figure 5.8: Combined continuous Coulomb, viscous and Stribeck friction model

(where $|\dot{x}| < \dot{x}_{\text{th}}$). In this velocity region the function assumes a value a fraction of the breakaway force proportional to the current velocity $\dot{x}$. Due to the presence of this fractional force, the surfaces may move relative to one another at a velocity less

than x_{th}. In practice this is not a problem as this value is chosen to be very small and the region with such small velocity is encountered for very short periods of time in the proposed design.

Table 5.4: Continuous static friction model coefficients

Symbol	Parameter	Value	Unit
F_s	Maximum static friction	0.65	N
C	Coulomb friction	0.55	N
s	Stribeck coefficient	80	
b	Viscous coefficient	4	Ns/m
$\dot{x}_{th}$	Minimum velocity threshold	1e-4	m/s
m	Mass of block	1	kg

5.3 DDA simulation results

The dual drive actuator as presented in this thesis is a rotary actuator. All previously utilised friction models are directly applicable by a simple change of variable, from x to θ and its derivatives. As the following chapter presents a physical system constructed using harmonic drive actuators, the simulation model parameters were selected to approximate such a configuration.

Simulation analysis begins with the 4 DoF model, following the structure of the development of the mathematical models. In case of each of the models, the output behaviour is investigated under powered and unpowered conditions.

The 2 DoF model is analysed most comprehensively as it is also the easiest to parameterise. Higher order models require the estimation of parameters that are difficult to measure in the system. The 4 DoF model is especially sensitive to correct parameterisation as otherwise oscillations of the coupling mechanism may occur.

5.3.1 Four degree-of-freedom model

When the system is not powered, the output experiences non-linear friction. As shown in Fig. 5.10b the velocity of the output is discontinuous and can be compared to Coulomb friction in Fig. 5.5b. The position-applied torque phase plot in Fig. 5.10a is also comparable to Fig. 5.4b. This is expected due to the high level of Coulomb friction present in the support bearing model.

Once power is applied to the system, the output exhibits linear friction properties. The position-applied torque phase plot shown in Fig. 5.11a is comparable to that exhibited by viscous only friction in Fig. 5.1b. The velocity in Fig. 5.11b remains continuous and closely resembles that of viscous only behaviour, as shown in Fig. 5.2b.

The closest mathematical model to the physical system is implemented using Eqs. (4.5 - 4.8) as shown in Fig. 5.9. By the introduction of finite coupling inertia J_c, the coupling stiffness K_c and friction B_c are split into two, one either side of the coupling as shown in the beginning of Chapter 4, Fig. 4.5.

Although symbolic analysis of system poles is difficult, as all parameters are known, numerical values can be found for the eigenvalues. It is, however, suspected that the chain formed of the motor inertias and the coupling $J_{m1} - K_{c1} - J_c - K_{c2} - J_{m2}$ may exhibit high frequency oscillations. Energy is taken out of this system by friction terms B_{m1}, B_{m2} and possible yet very small coupling friction B_{c1} and B_{c2}. Oscillations arise as transmitted motion between J_{m1} and J_{m2} lags in phase. The higher the coupling stiffness coefficients, the lower the lag and hence oscillations of higher frequency are likely to arise. The effects of low K_c and J_c can be seen in Fig. 5.12a. By increasing the inertia of the coupling J_c, the oscillations can be reduced (see Fig. 5.12b) as friction contributed by either drive become more effective. Also, higher rotor velocity results in higher friction forces and hence more damping is available to the system.

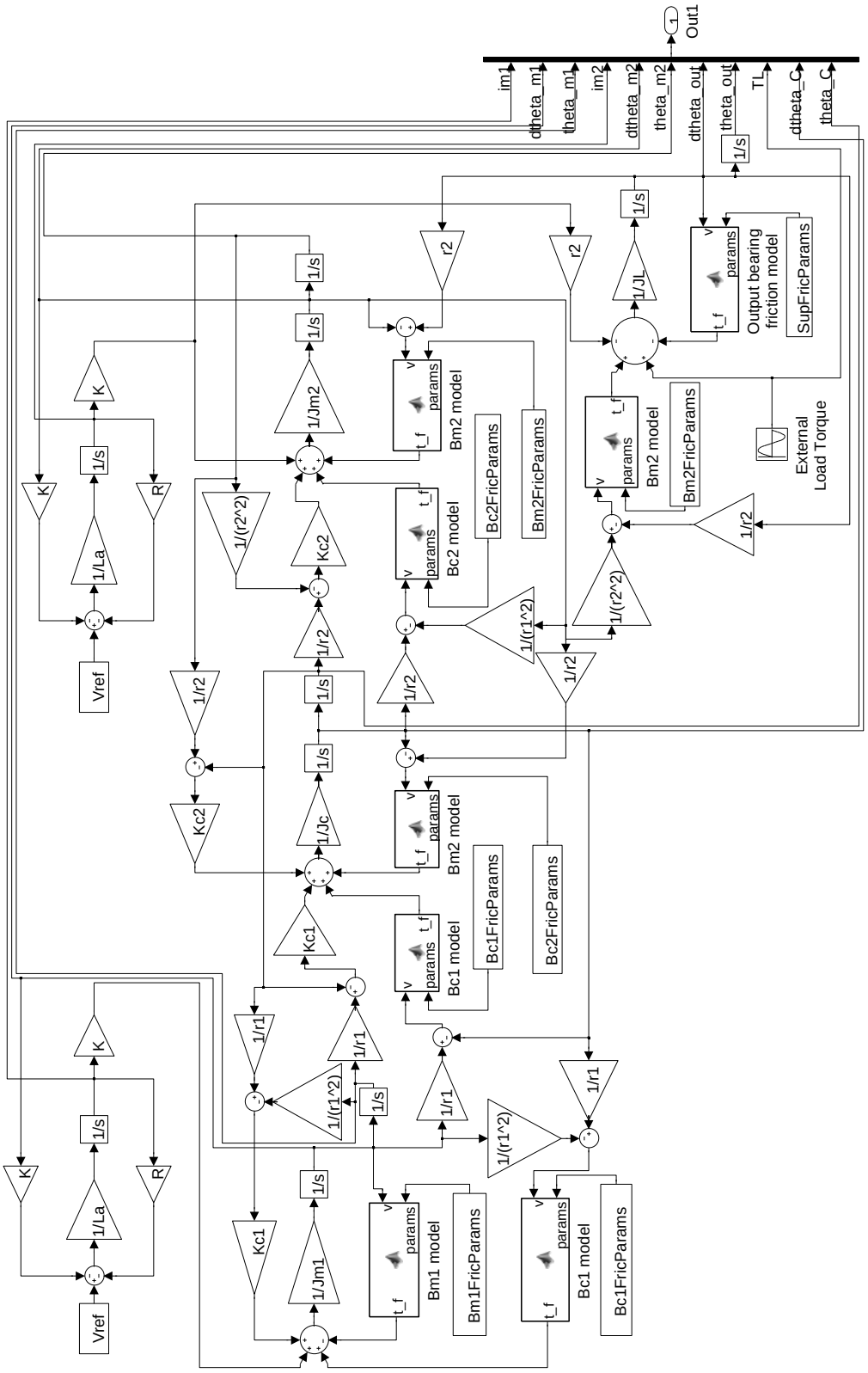

Figure 5.9: 4 DoF Simulink model - open loop, constant voltage supply

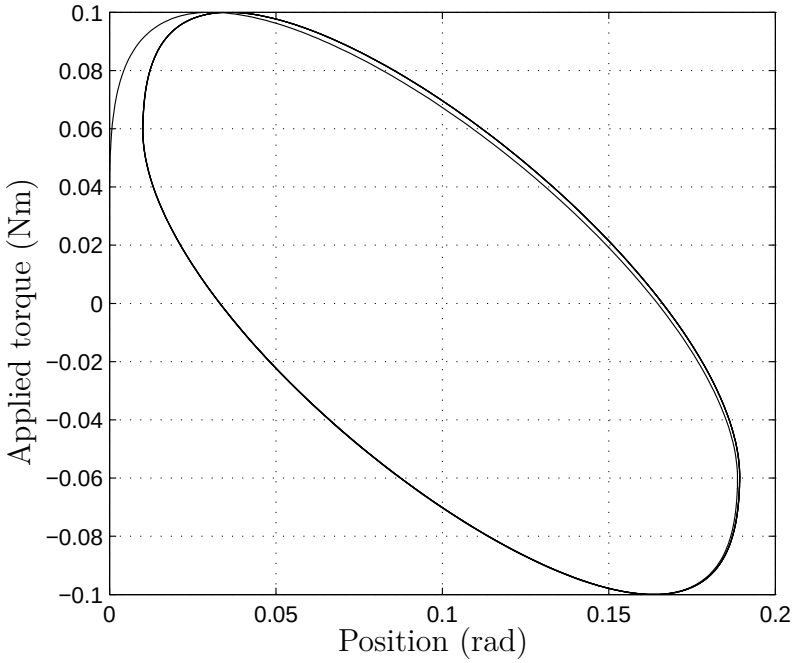

(a) Position/Applied torque

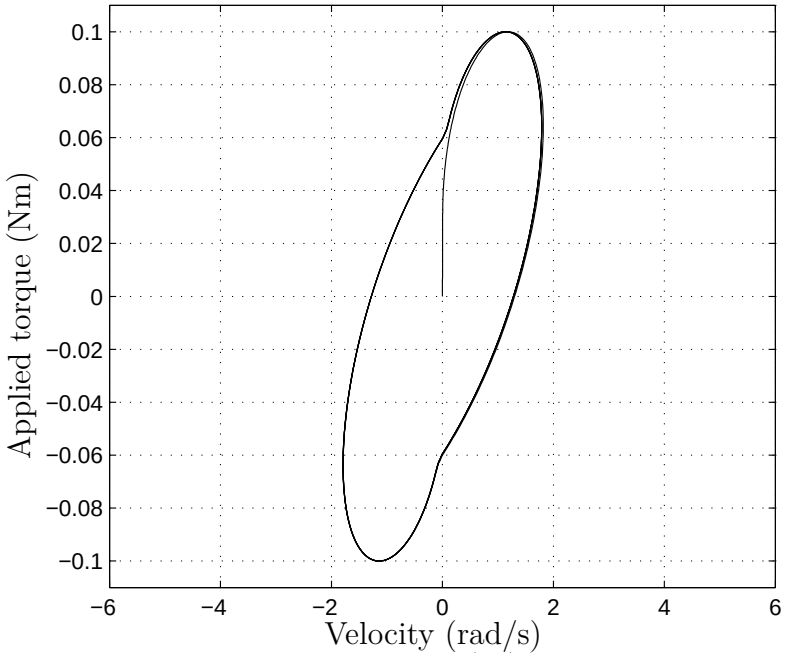

(b) Velocity/Applied torque

Figure 5.10: Unpowered 4 DoF Dual Drive Actuator output behaviour. The applied load torque against a) output position and b) output velocity

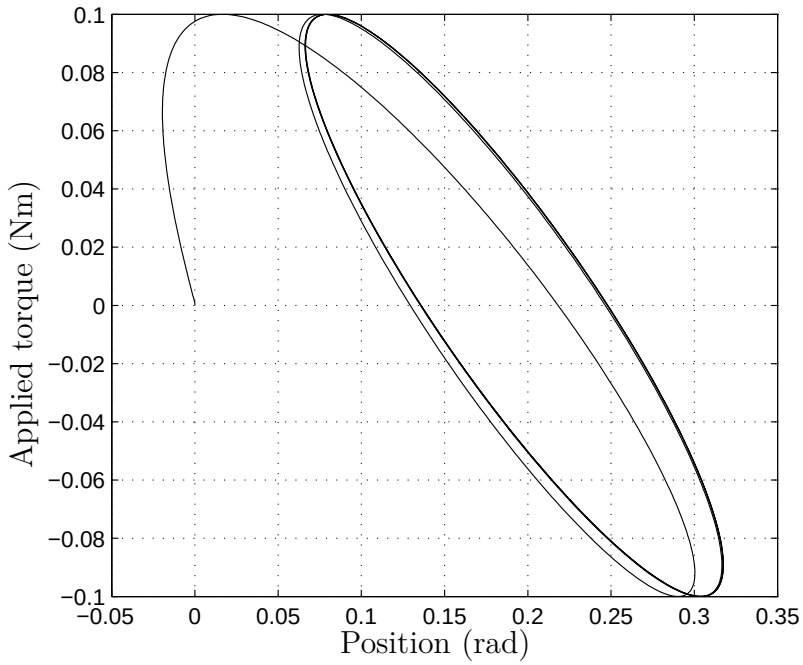

(a) Position/Applied torque

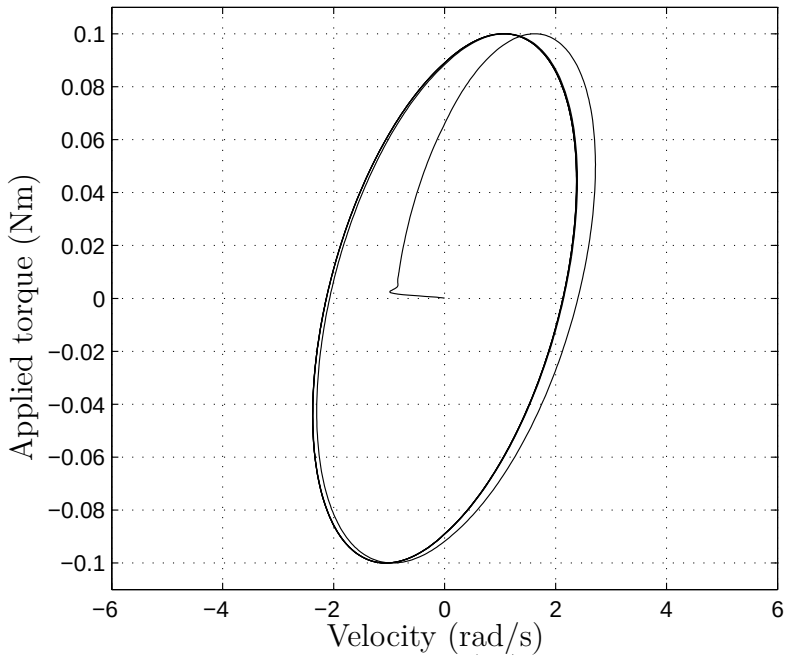

(b) Velocity/Applied torque

Figure 5.11: Powered 4 DoF Dual Drive Actuator output behaviour. The applied load torque against a) output position and b) output velocity

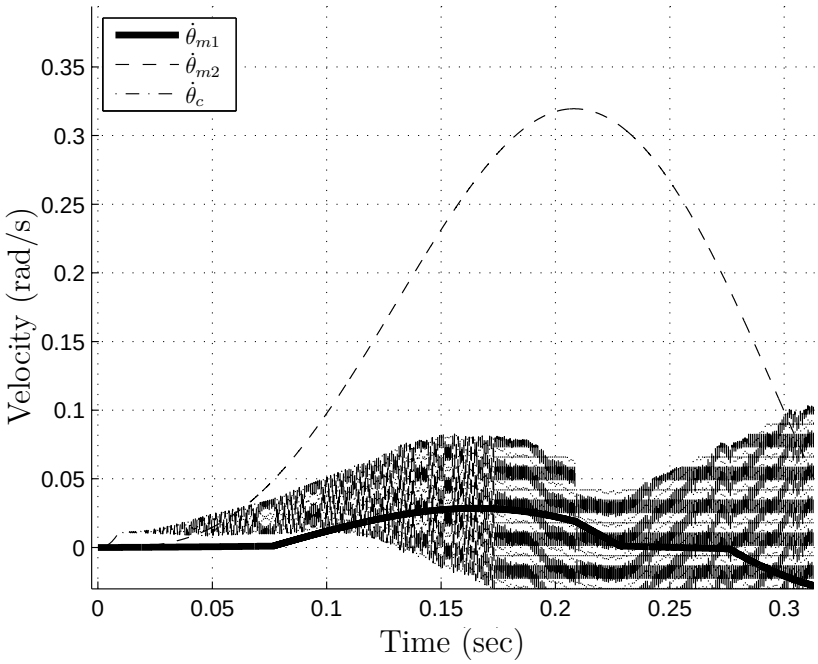

(a) $K_c = 30\text{Nm/rad}$, $J_c = 1e^{-6}\text{kgm}^2$

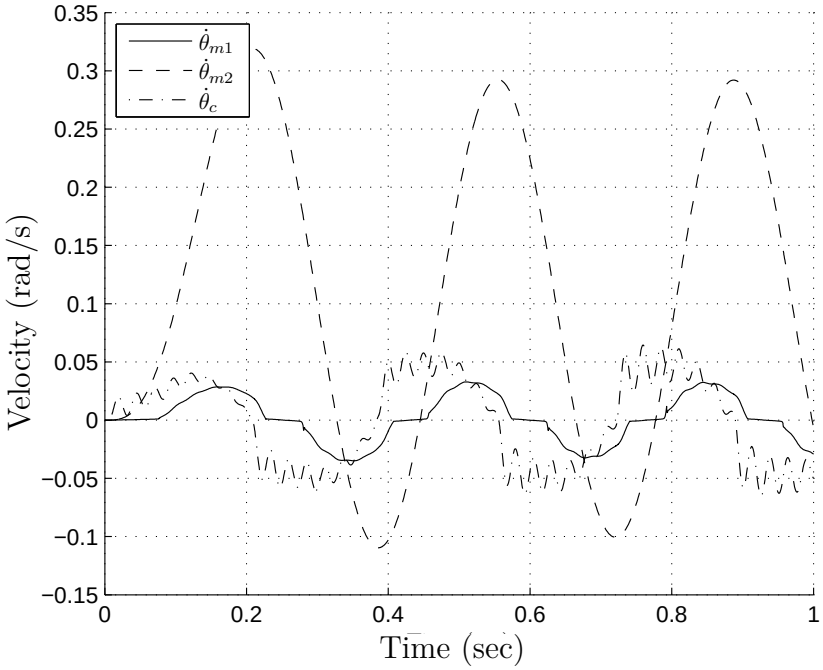

(b) $K_c = 30\text{Nm/rad}$, $J_c = 2e^{-3}\text{kgm}^2$

Figure 5.12: 4 DoF Dual Drive Actuator behaviour. (a) Coupling oscillations arise due to high stiffness and low inertia of coupling mechanism. (b) Such oscillations can be mitigated by increasing the coupling inertia.

5.3.2 Three degree-of-freedom model

This model, as shown in Fig. 5.13 is based on Eqs. (4.12 - 4.14). By allowing the coupling mechanism between the two rotors to be of limited torsional stiffness, the inertias J_{m1} and J_{m2} are treated as separate entities. The stiffness K_c may vary greatly, from over 10^4Nm/rad (when the two rotors are connected using rigid steel tubing) to around 30Nm/rad (in case of a helical coupling).

Under no power, external torque is applied to the DDA. The velocity of each motor is shown in Fig. 5.14a. In this case, the coupling mechanism has a stiffness of $K_c = 30$Nm/rad, which allows the output to rotate significantly without producing sufficient torque for the primary motor to move. The velocity of the output if shown in Fig. 5.14b. This configuration allows for a lag between the movement of J_{m2} and J_{m1}, and in turn B_{m1} has little effect and B_{m2} has also lesser effect on the output of the DDA. In Fig. 5.15a K_c is increased to 1000Nm/rad, which in turn transfers more torque for a given deflection. Hence less movement between J_{m2} and J_{m1} will result from the same torque and both B_{m1} and B_{m2} have greater effect on the output. This greater - non-linear - effect is more apparent in Fig. 5.15b. However, low stiffness coupling mechanism may limit the torque production of the DDA.

Once power is applied ($v_m = 9V$), the motors rotate as shown in Fig. 5.16a. The output of the actuator, even in the case of highly stiff coupling of $K_c = 1000$Nm/rad exhibits linear friction, as shown in Fig. 5.16b. The motor velocities are affected differently between the two models. The higher order model more accurately predicts the actual motor velocities as friction torque from the load acts on J_{m2}, deflection of which in turn is transferred to J_{m1} through a coupling mechanism. This is a closer approximation to the physical system.

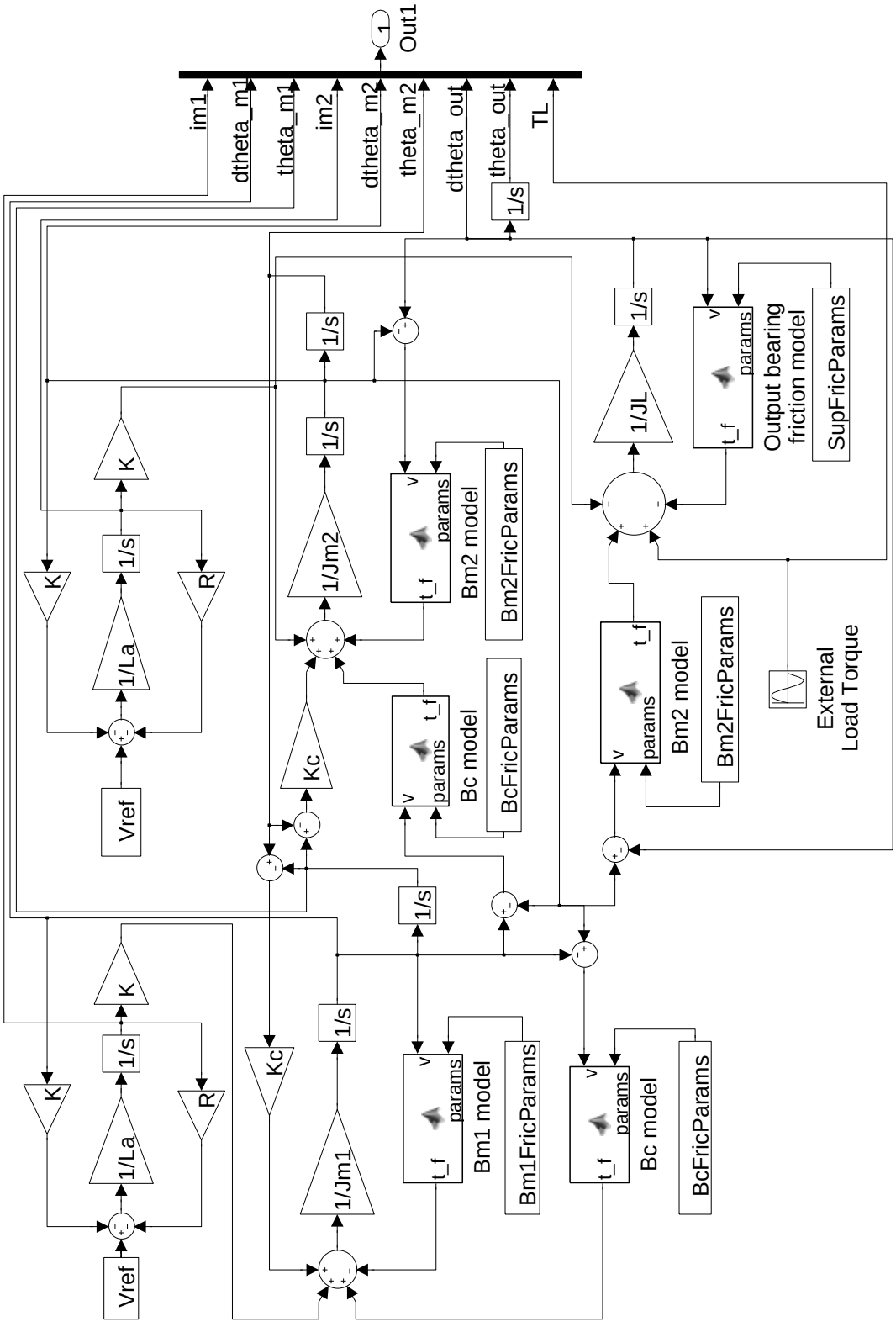

Figure 5.13: 3 DoF Simulink model - open loop, constant voltage supply

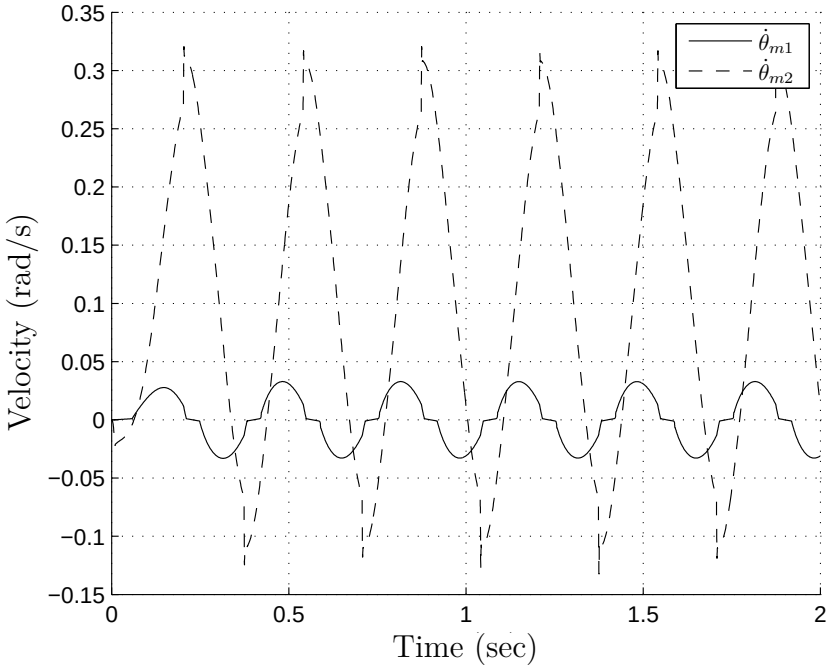

(a) Motor velocity/Time

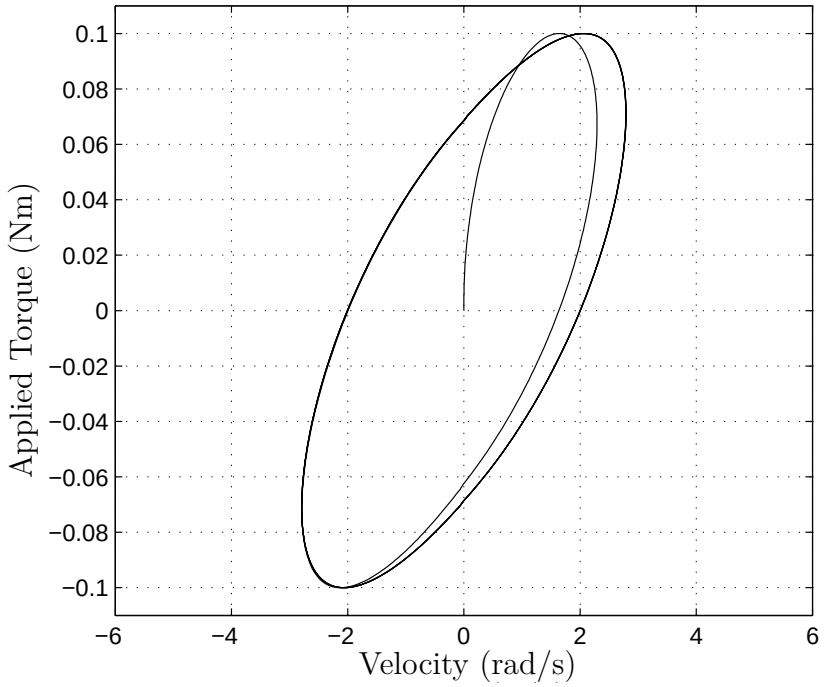

(b) Velocity/Applied torque

Figure 5.14: 3 DoF DDA Output friction behaviour - helical coupling, $v_m = 0V$

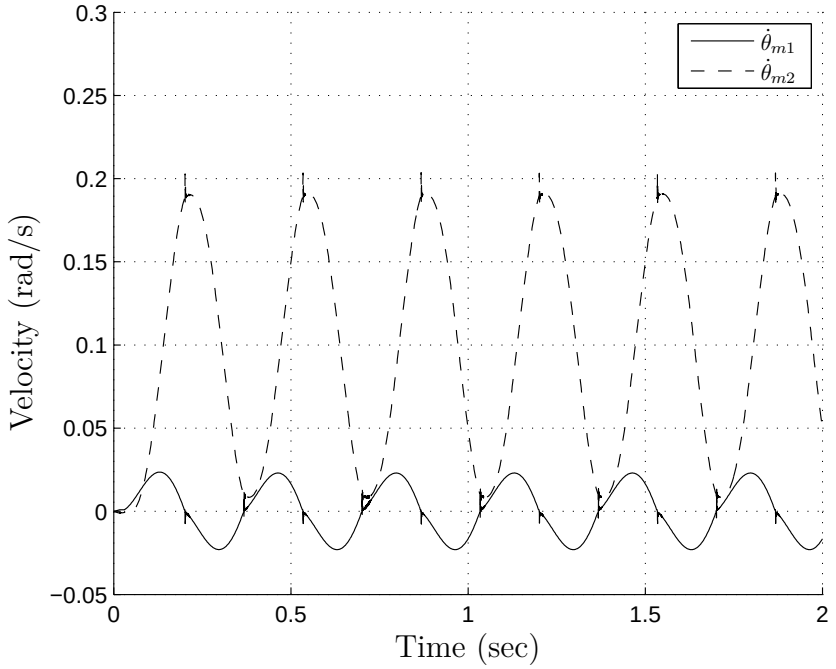

(a) Motor velocity/Time

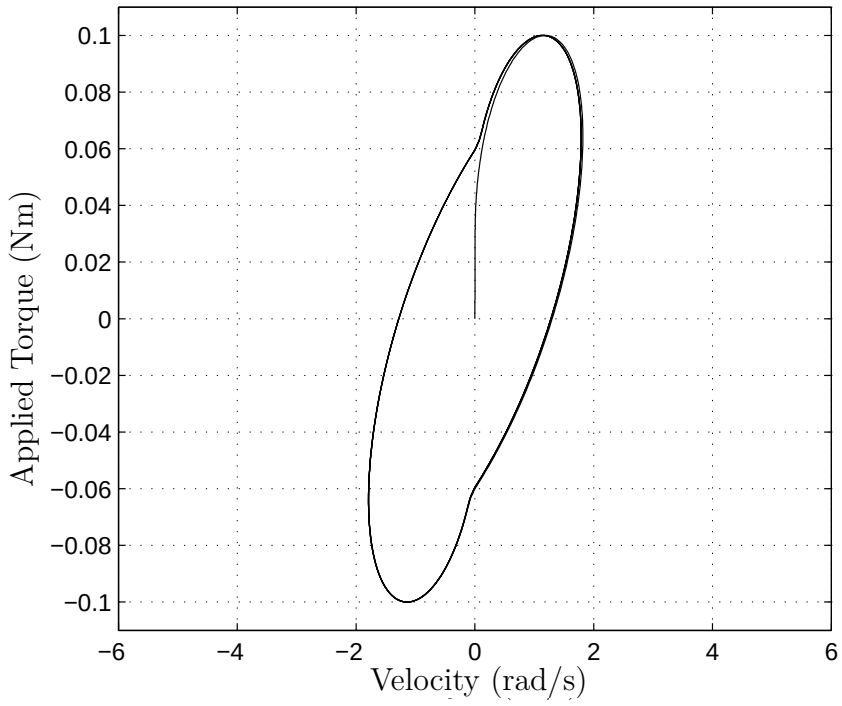

(b) Velocity/Applied torque

Figure 5.15: 3 DoF DDA Output friction behaviour - rigid coupling, $v_m = 0$V

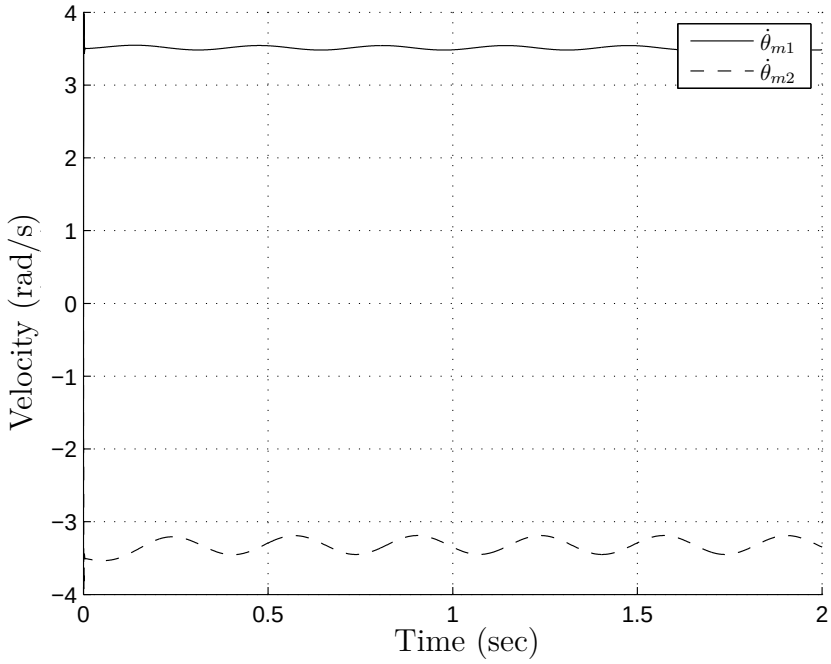

(a) Motor velocity/Time

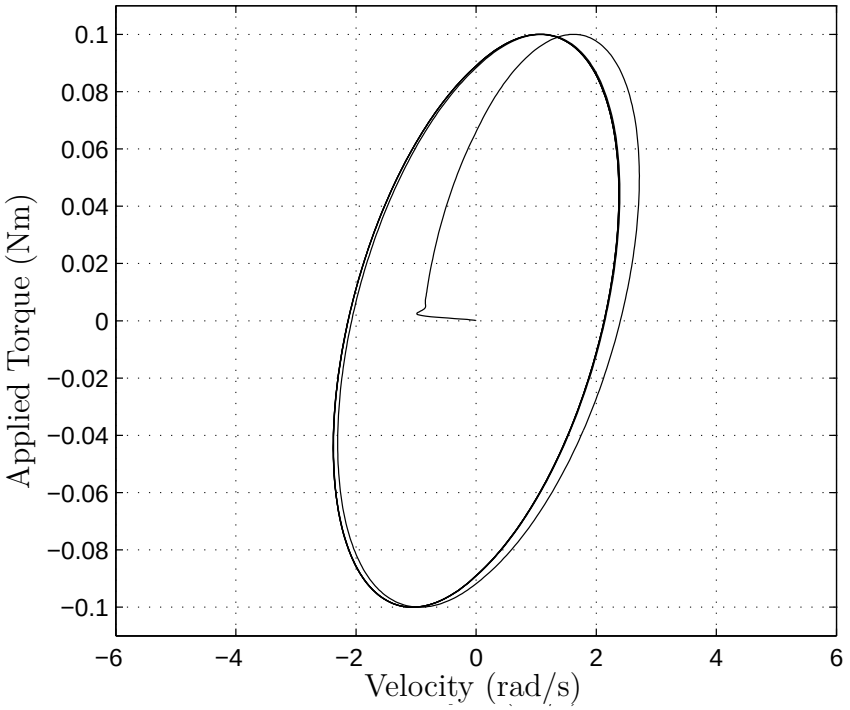

(b) Velocity/Applied torque

Figure 5.16: 3 DoF DDA Output friction behaviour - rigid coupling, $v_m = 9$V

5.3.3 Two degree-of-freedom model

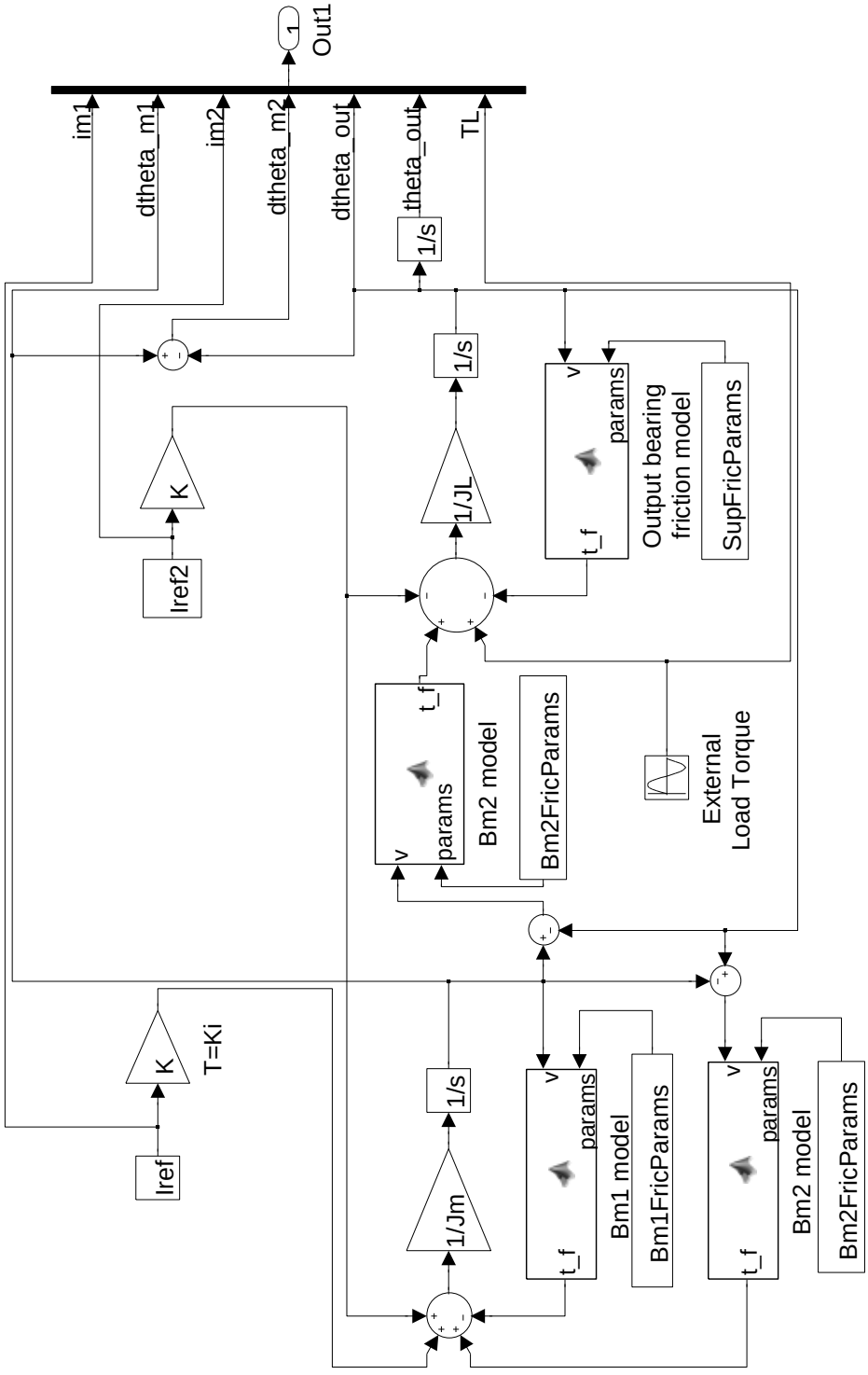

Figure 5.17: 2 DoF Simulink model - open loop, constant current supply

The mathematical model described by Eqs. (4.15) and (4.16) is implemented in Simulink as shown in Fig. 5.17. The motors are driven using constant current sources and the system is open loop. The transient response of the each motor is shown in Fig. 5.18a.

The rotors are accelerated until the motor torque is balanced by friction torques and the motor velocities settle. The output velocity is the sum of the two motor velocities, hence it also settles as shown in Fig. 5.18b. During the initial start-up period, the output swings as the two motor velocities are unmatched. Within one second, all velocities settle.

Initially, the secondary drive is supported by the coupling mechanism to the primary drive and hence no support bearing is present. In this configuration, only friction inherent to the drives are present. Under open loop conditions, the motor velocities will only be matched (and hence the output velocity zero) when the two motor parameters including friction coefficients are equal. In a practical system this will not be the case, hence the system must incorporate velocity feedback loops to compensate for any mismatch in parameters. Fig. 5.19a shows the effect of such mismatch, including the output velocity shown in Fig. 5.19b. For the investigation, however, the parameters may be assumed to be identical.

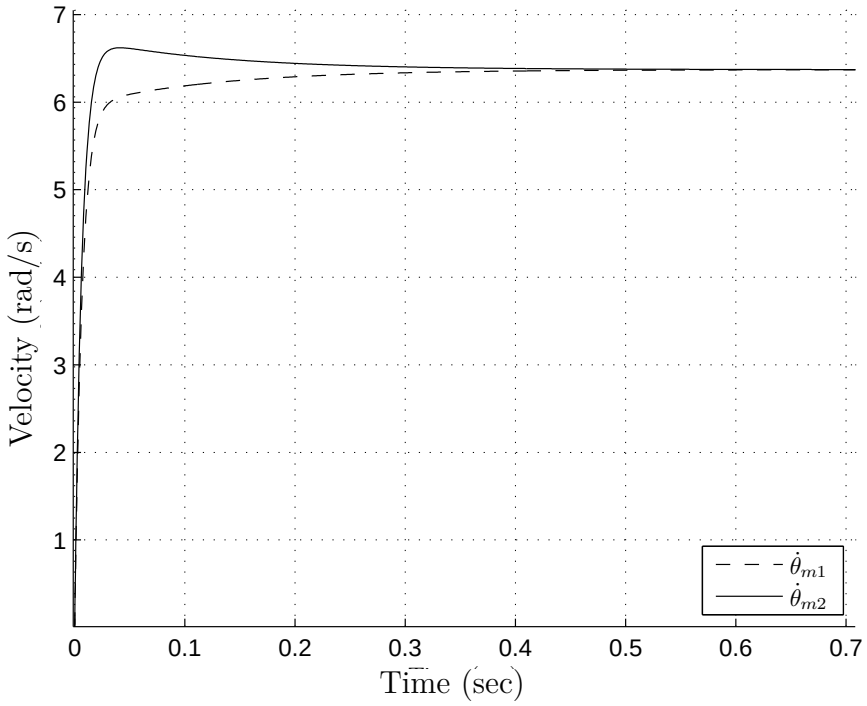

(a) Motor velocities

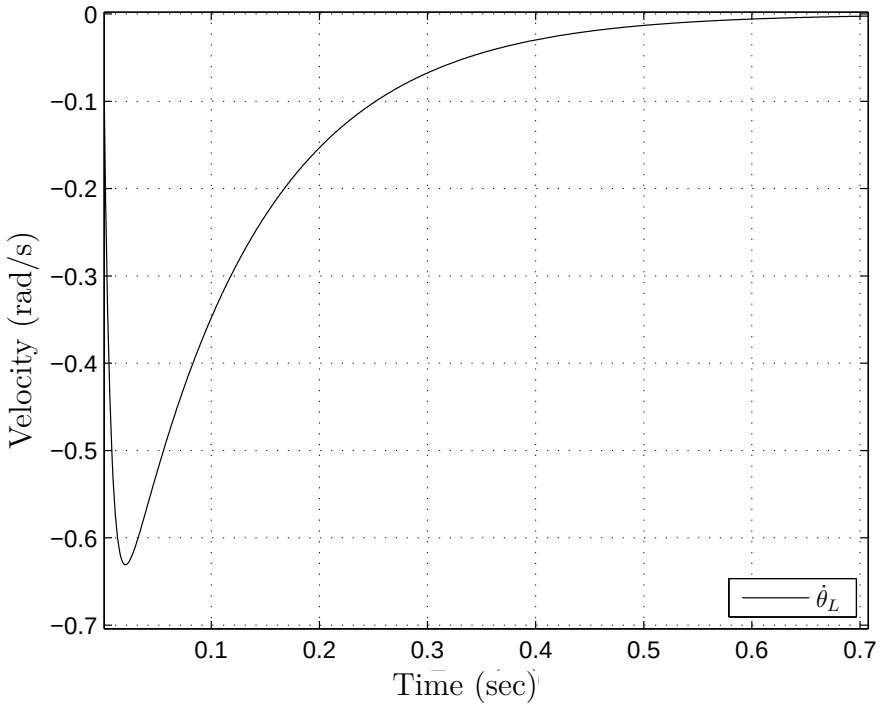

(b) Load velocity

Figure 5.18: 2 DoF transient response - matching parameters

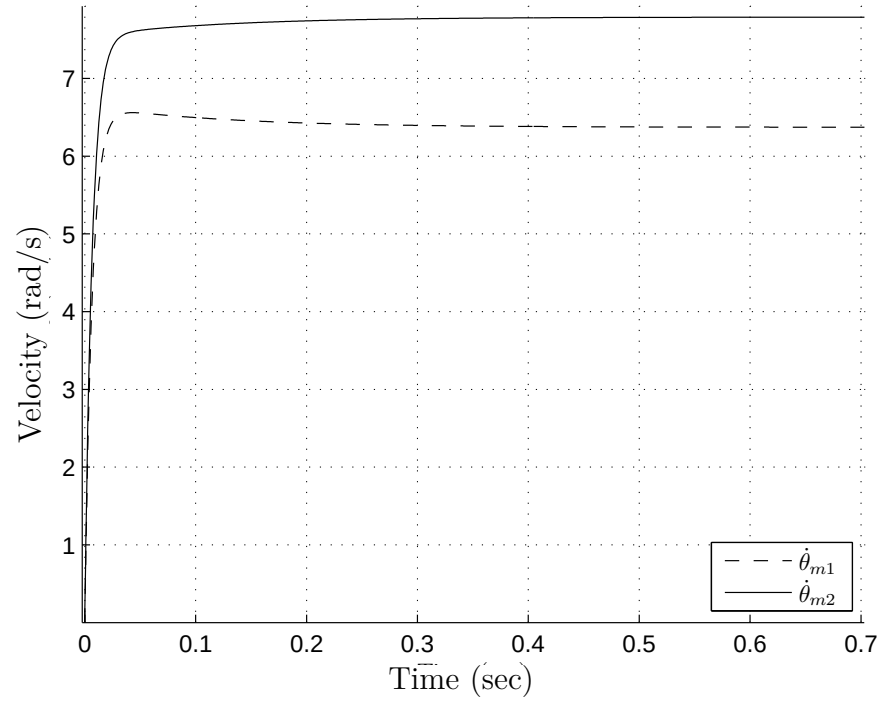

(a) Motor velocities

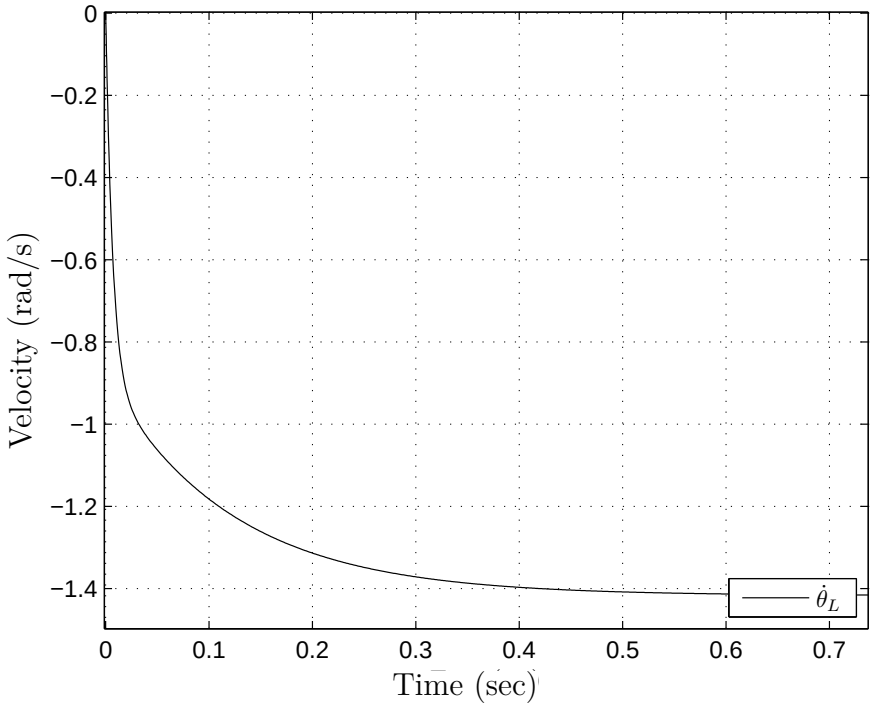

(b) Load velocity

Figure 5.19: 2 DoF transient response - mismatched parameters

As shown in Fig. 5.21b, if a load torque is applied when the motors are supplied no current ($i = 0$A) and hence the rotors are not spinning shown in Fig. 5.21a, then the DDA exhibits strong non-linear friction. The premise of the DDA structure is that once the combined rotor spins, the inherent non-linear friction effects in each motor are eliminated and the resultant behaviour is that of an actuator with linear friction. By supplying sufficient current to each motor so as to bring the rotors into motion ($i = 0.1$A) as shown in Fig. 5.20a, friction arising from the motors is now linear, and hence the output experiences linear friction as well, as shown in Fig. 5.20b.

However, the constant current open loop supply to the motors limits the acceleration of the rotors. An alternative Simulink model, as presented in Fig. 5.24, instead incorporates the electrical model of the motor and allows a constant voltage supply to be introduced. This effectively acts as closed loop current control and provides higher accelerations by admitting more current through the armature when the actual velocity and velocity at supply do not match. Once the supply voltage is set to zero and torque is applied on the output of the DDA, the motor velocities shown in Fig. 5.22a and output velocity shown in Fig. 5.22b. These clearly indicate highly non-linear behaviour. The output position in Fig. 5.23a and velocity in Fig. 5.23b clearly demonstrate the presence of high Coulomb and viscous friction.

As the rotor is forced to turn, it generates a voltage proportional to its velocity. In a closed circuit this voltage creates current which in turn opposes the motion of the rotor. This results in larger apparent viscous friction in the motors and hence on the output of the actuator. This further compounds the friction present in each drive. When sufficient voltage is provided to the motors, the rotors spin and clear the non-linear region of drive friction and the resultant friction behaviour of the DDA is again linear. However the effective viscous friction is now greater. This is an intrinsic property of the drives when voltage sources are used to supply power.

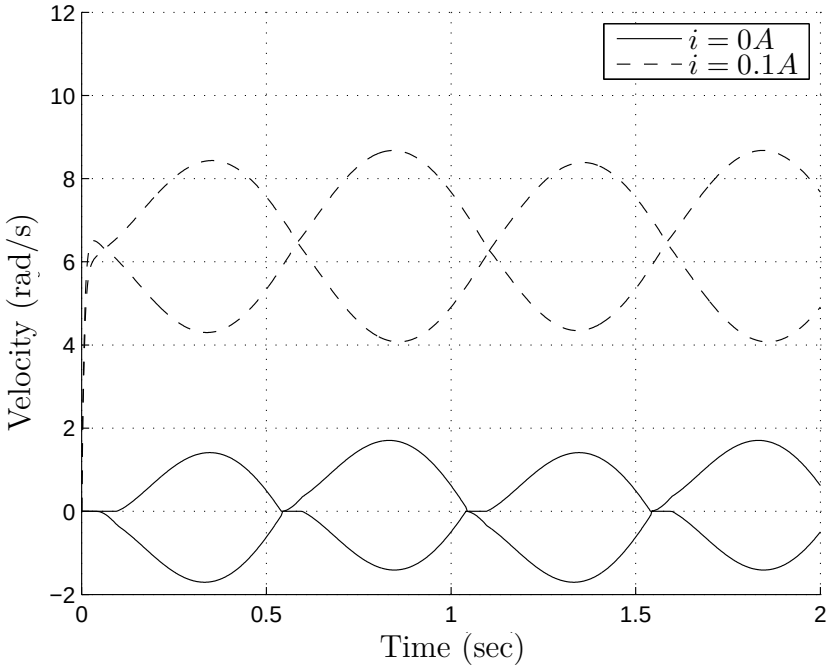

(a) Motor velocities

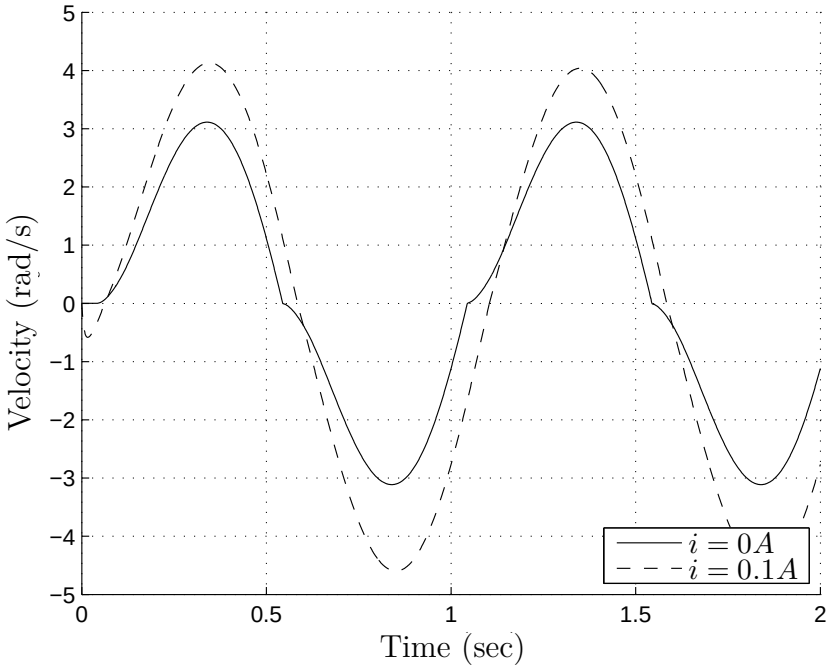

(b) Output velocity

Figure 5.20: 2 DoF DDA Friction behaviour with external torque applied, (a) drive velocities and (b) output velocity

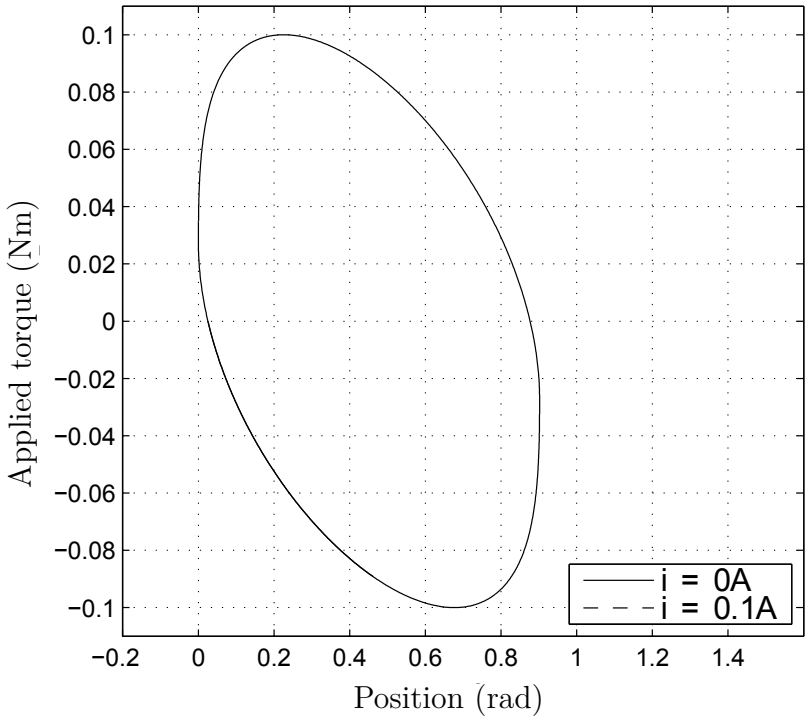

(a) Position/Applied torque

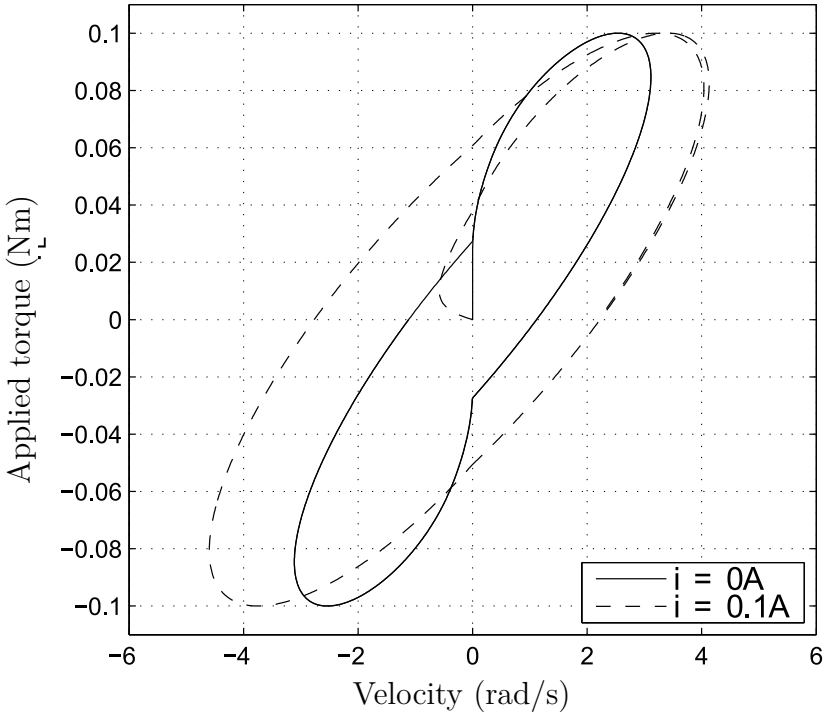

(b) Velocity/Applied torque

Figure 5.21: 2 DoF DDA Friction behaviour with external torque applied, (a) output position and (b) output velocity

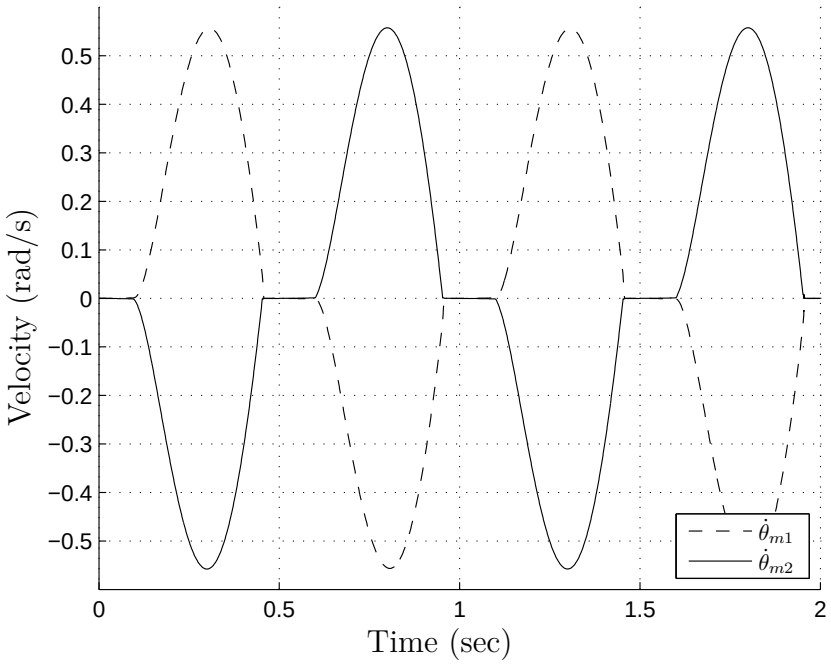

(a) Motor velocity/Time

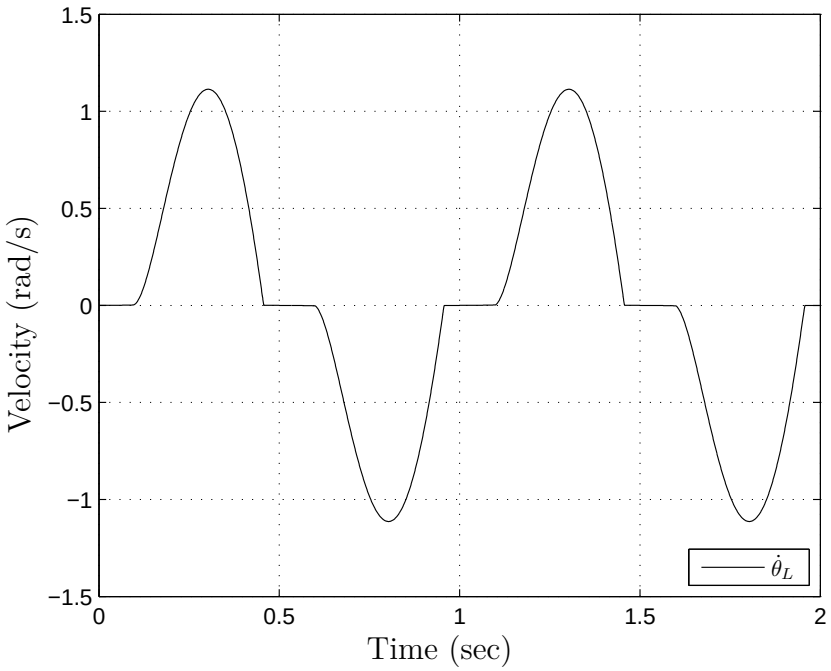

(b) Output velocity/Time

Figure 5.22: 2 DoF DDA Output friction behaviour with external torque applied, (a) drive velocities and (b) output velocity

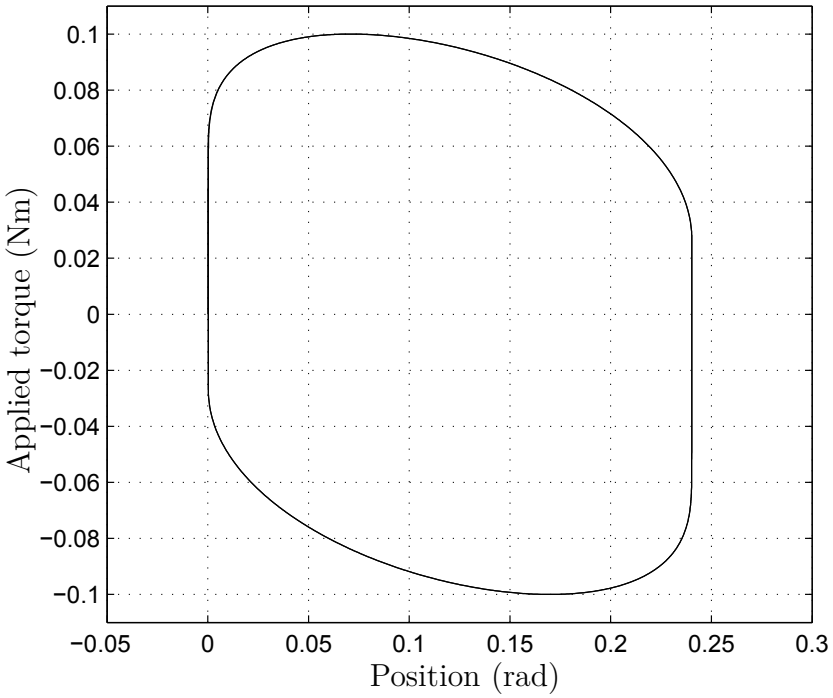

(a) Position/Applied torque

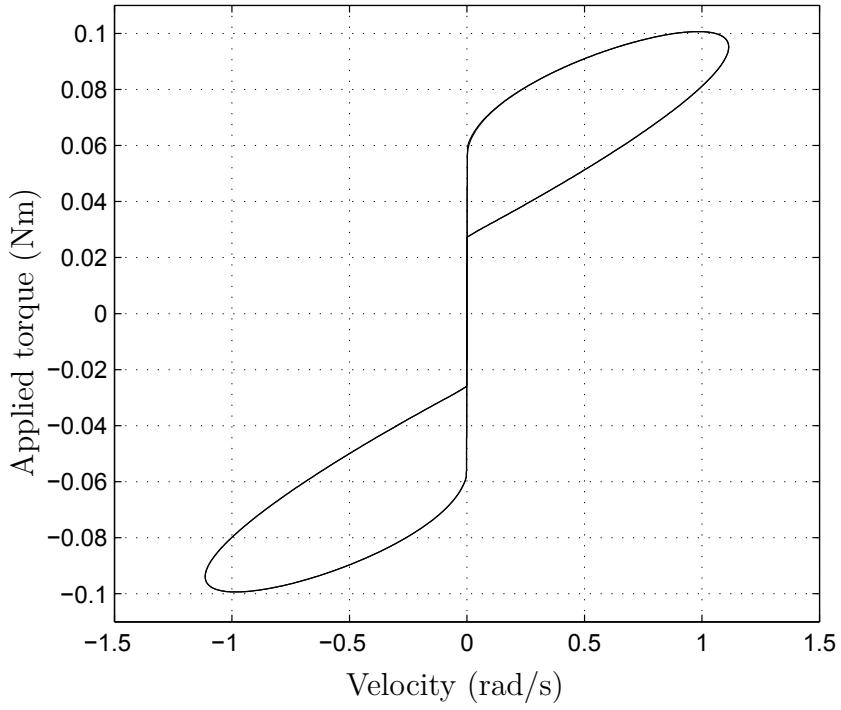

(b) Velocity/Applied torque

Figure 5.23: 2 DoF DDA Output friction behaviour, unpowered - Applied torque effect on (a) output position and (b) output velocity

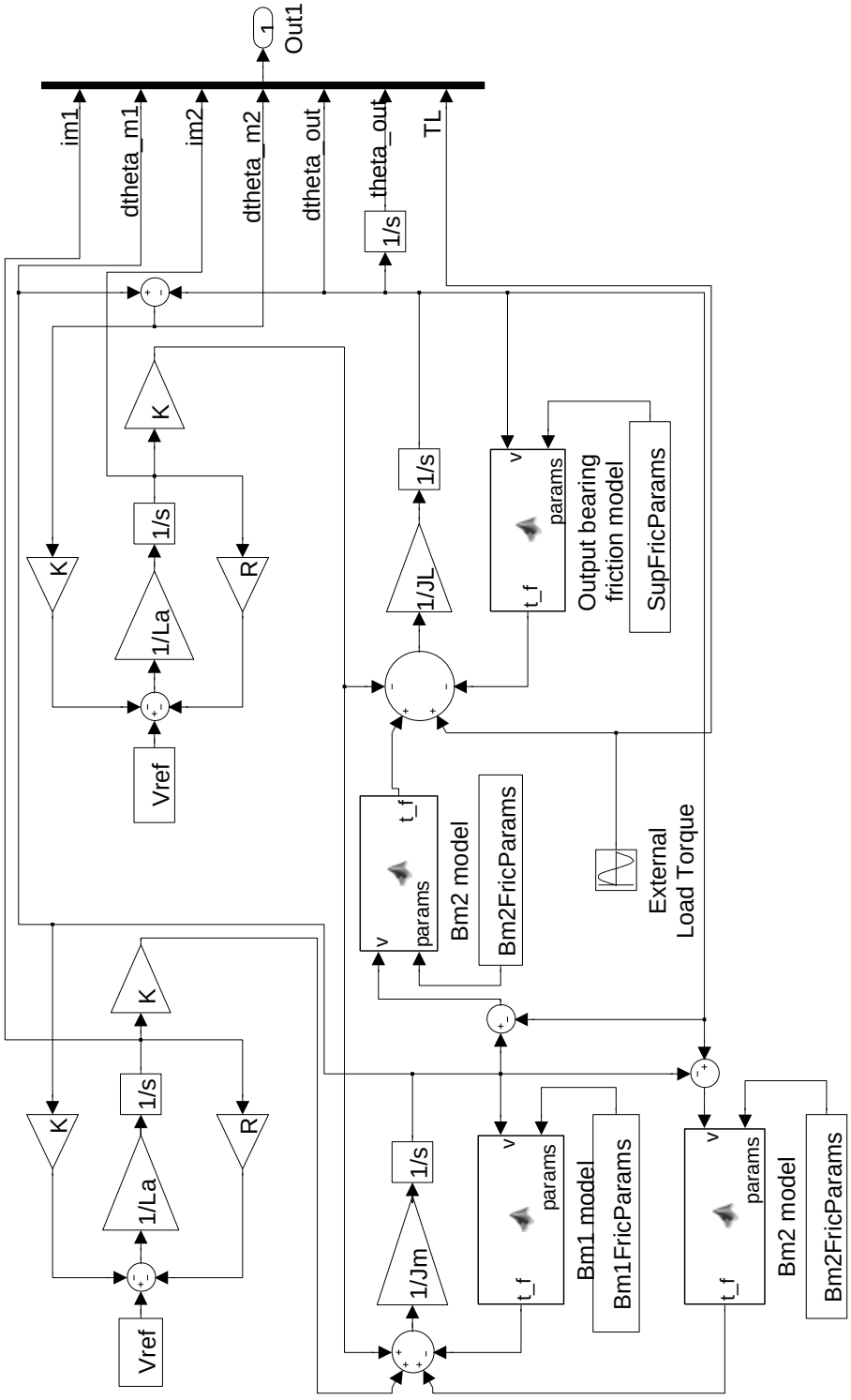

Figure 5.24: 2 DoF Simulink model - open loop, constant voltage supply

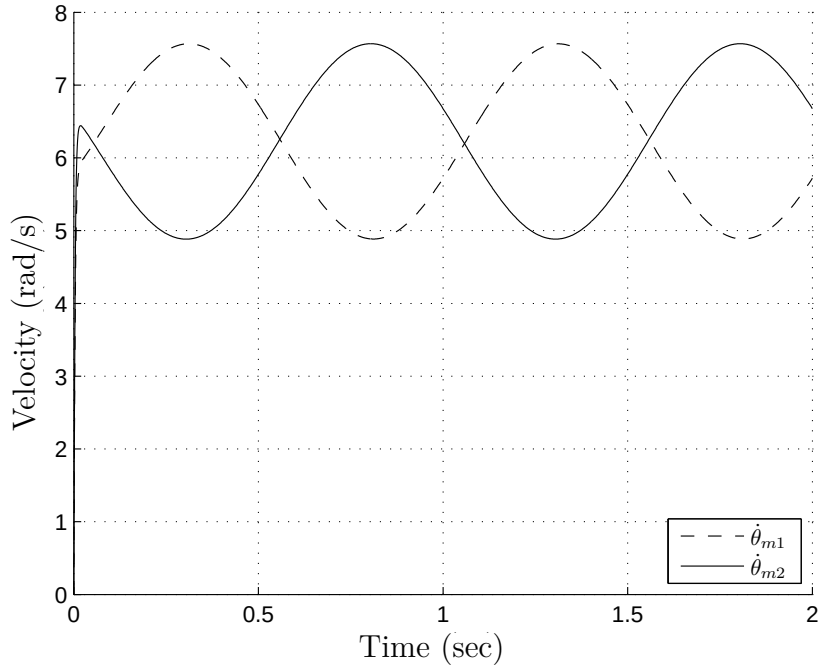

(a) Motor velocity/Time

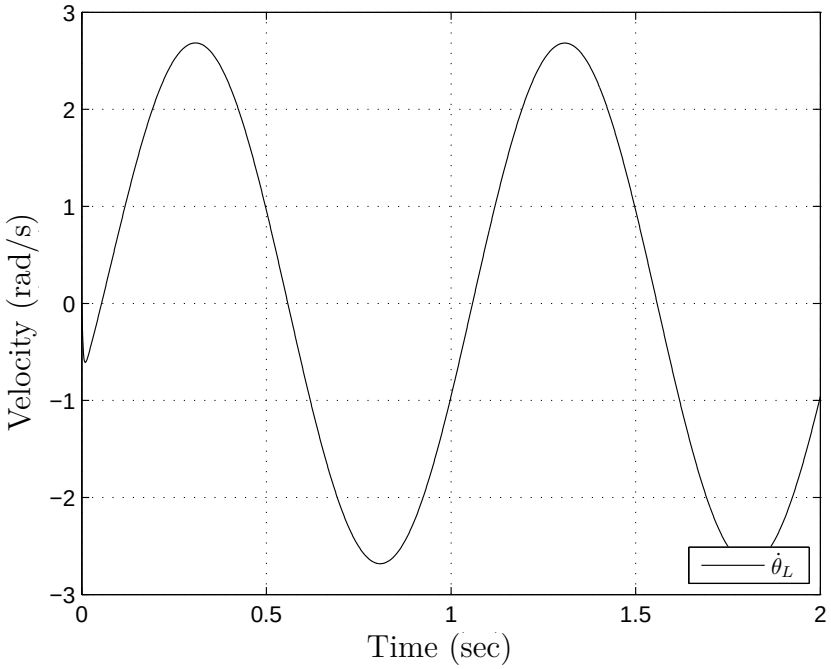

(b) Output velocity/Time

Figure 5.25: 2 DoF DDA Output friction behaviour, powered - Applied torque effect on (a) motor velocities and (b) output velocity

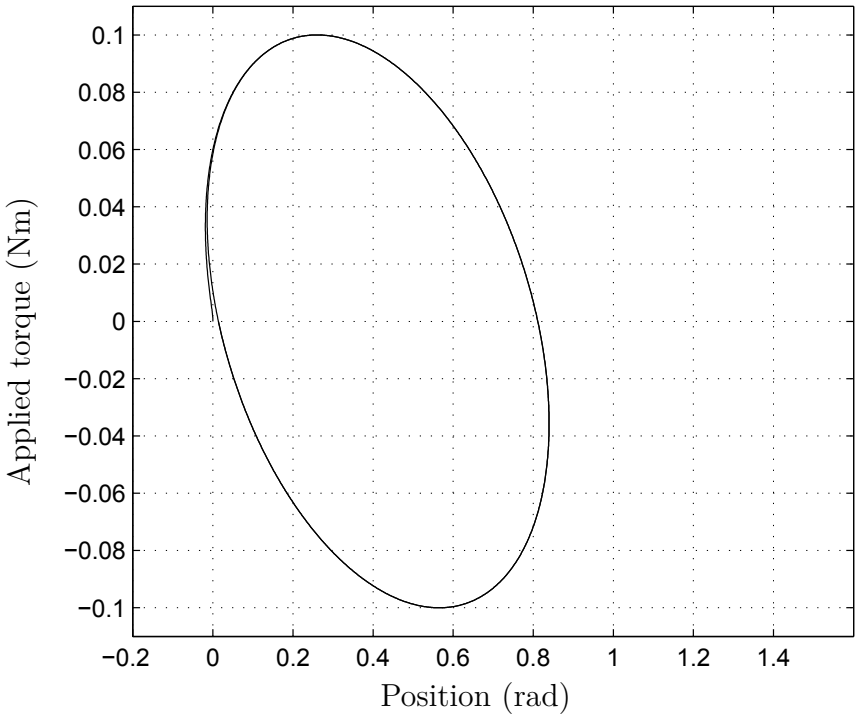

(a) Position/Applied torque

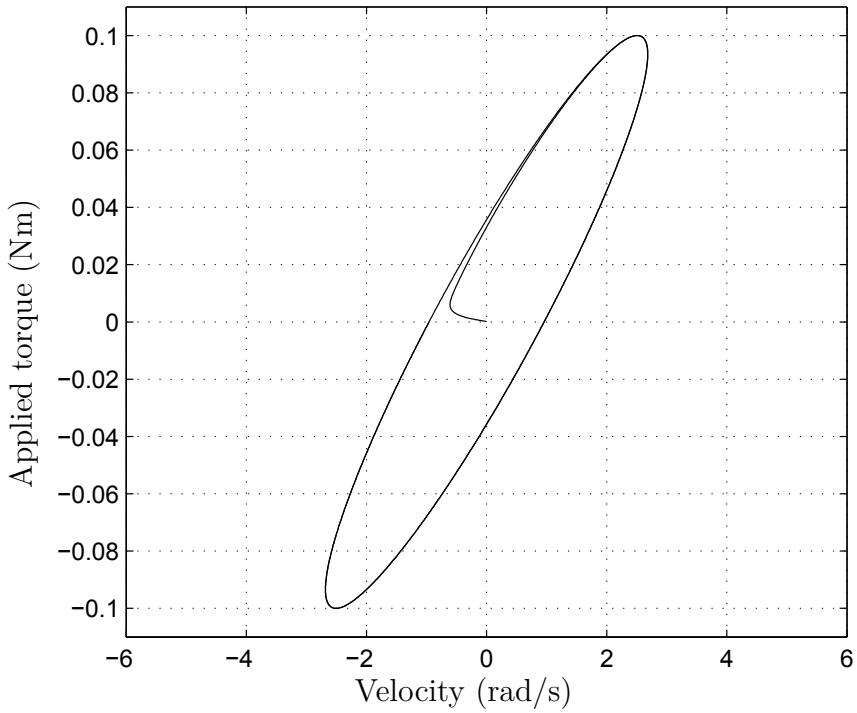

(b) Velocity/Applied torque

Figure 5.26: 2 DoF DDA Output friction behaviour, powered - Applied torque effect on (a) output position and (b) output velocity

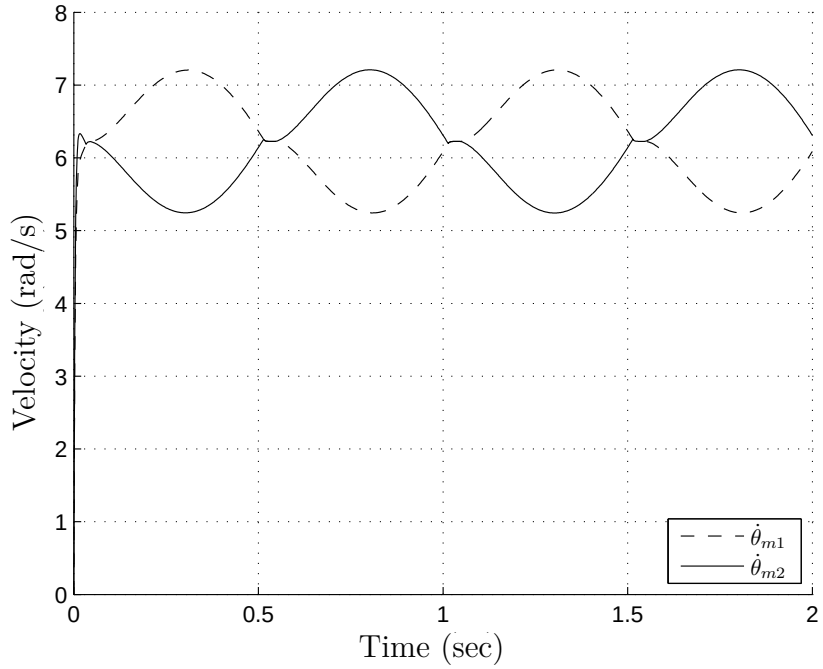

(a) Motor velocity/Time

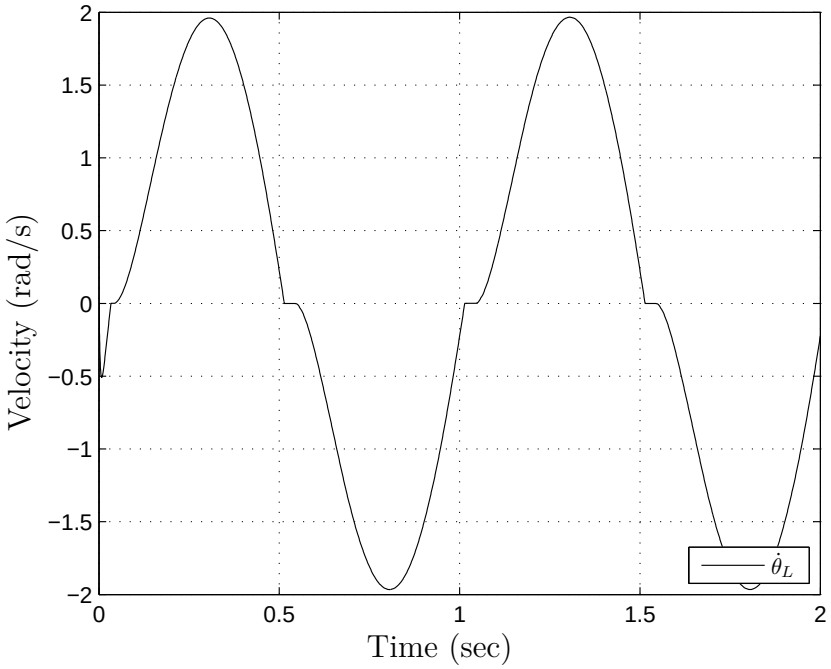

(b) Output velocity/Time

Figure 5.27: 2 DoF DDA Output friction behaviour incl. support bearing - Applied torque effect on (a) motor velocities and (b) output velocity

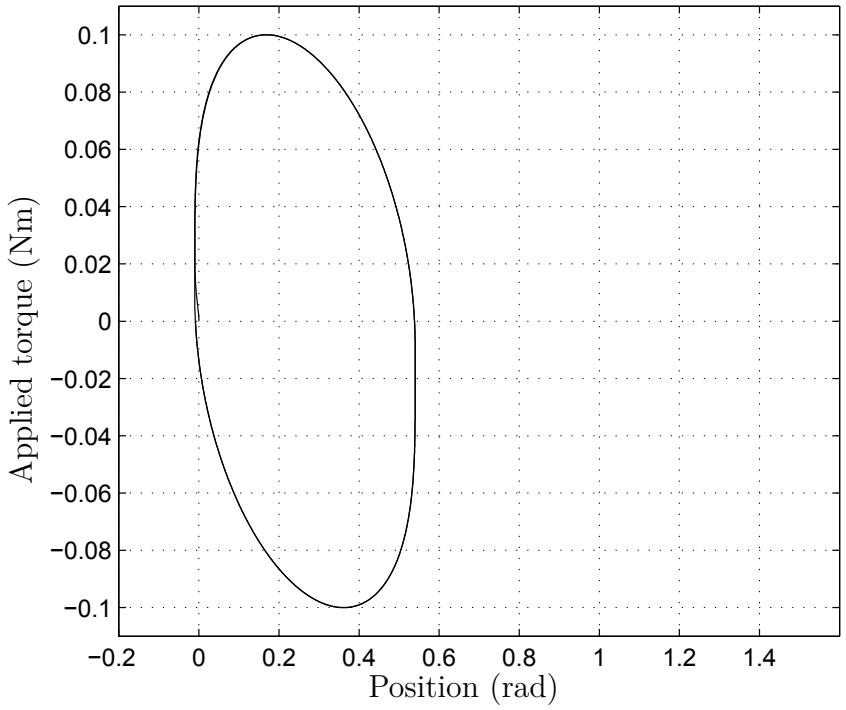

(a) Position/Applied torque

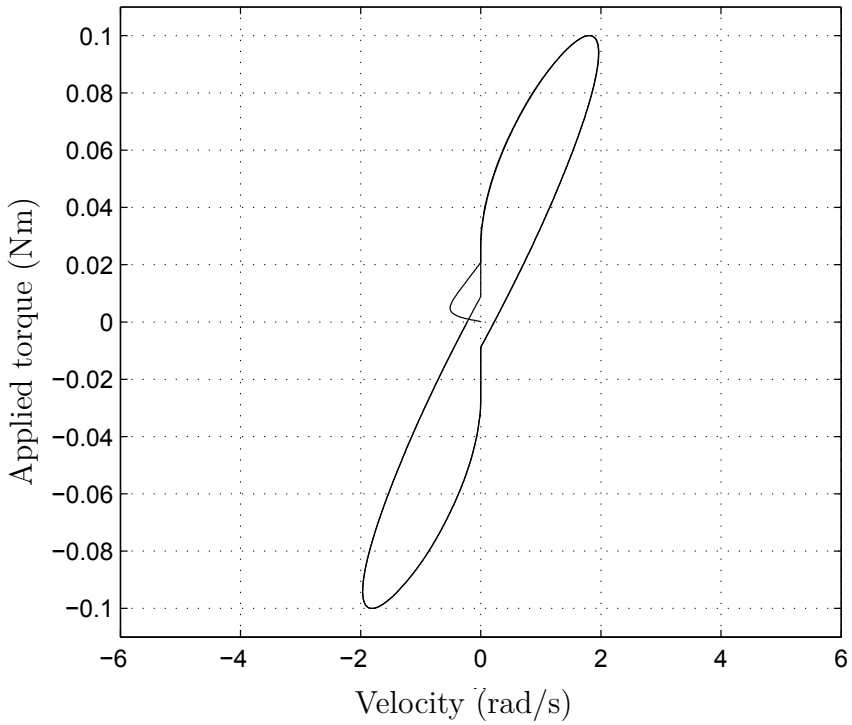

(b) Velocity/Applied torque

Figure 5.28: 2 DoF DDA Output friction behaviour incl. support bearing - Applied torque effect on (a) output position and (b) output velocity

The DDA is demonstrated to be capable of eliminating non-linear friction due to the drives, as shown in Fig. 5.25a, and hence at the output in Fig. 5.25b. This results in a linear motion profile of the output as shown in Figs. 5.26a and 5.26b.

The effects of friction present in the support bearing on the output is shown in Fig. 5.28a. Although the drives are clearly spinning as shown in Fig. 5.27a and hence only contribute viscous friction, the bearing supporting the output provides a source of non-linear behaviour, see Fig. 5.28b.

The results suggest that although the DDA itself is capable of displaying an output friction profile that is purely viscous in nature, components external to it, such as the output support bearing will still affect the overall performance.

5.4 Closed loop position step response

A common actuator in robotics applications is the geared motor. As discussed in Chapter 2, such arrangements suffer from increased friction and non-linearities such as stiction and potentially backlash. A simulated dc motor with high coulomb friction as a result of its gearbox is used for comparison with the performance of the simulated 2 DoF DDA system.

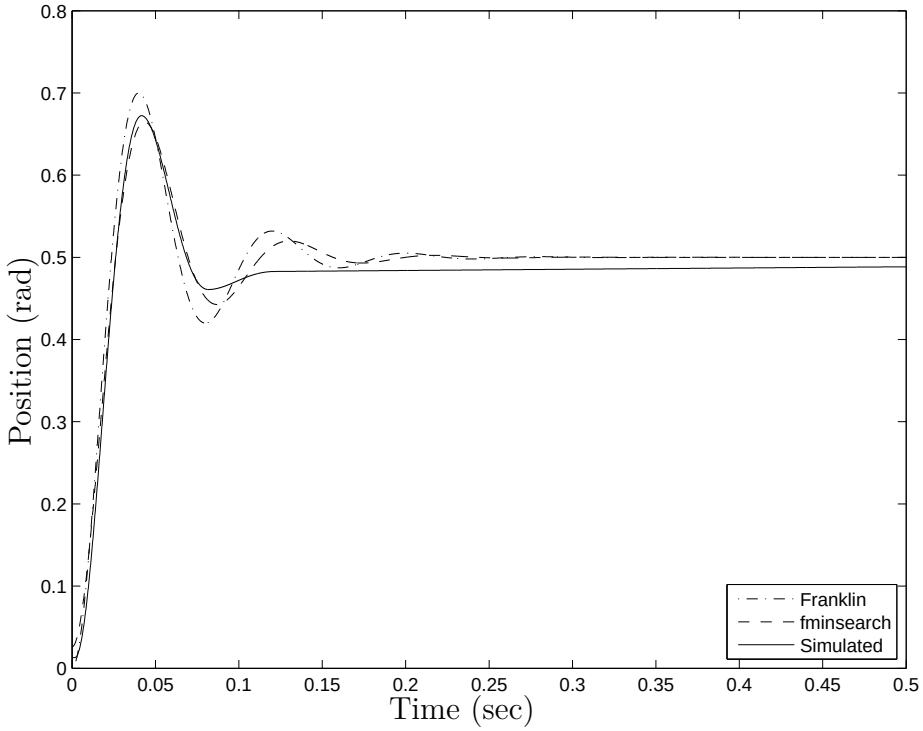

Figure 5.29: Simulated step response of a geared dc motor with high levels of static friction. The output settles prematurely and in error of the reference position.

The step response of a 0.5 rad step is shown in Fig. 5.29 under P only control. The gain of the controller was found by increasing it to the point when the response exhibited sustained oscillations, and then decreased by 10%. The same method is applied later in the empirical results of the physical implementation.

As the vast majority of closed loop step response appears to exhibit characteristics of a second order system (from which this system is no exception), an equivalent second order transfer function may be derived for comparison. Franklin [108, Chap-

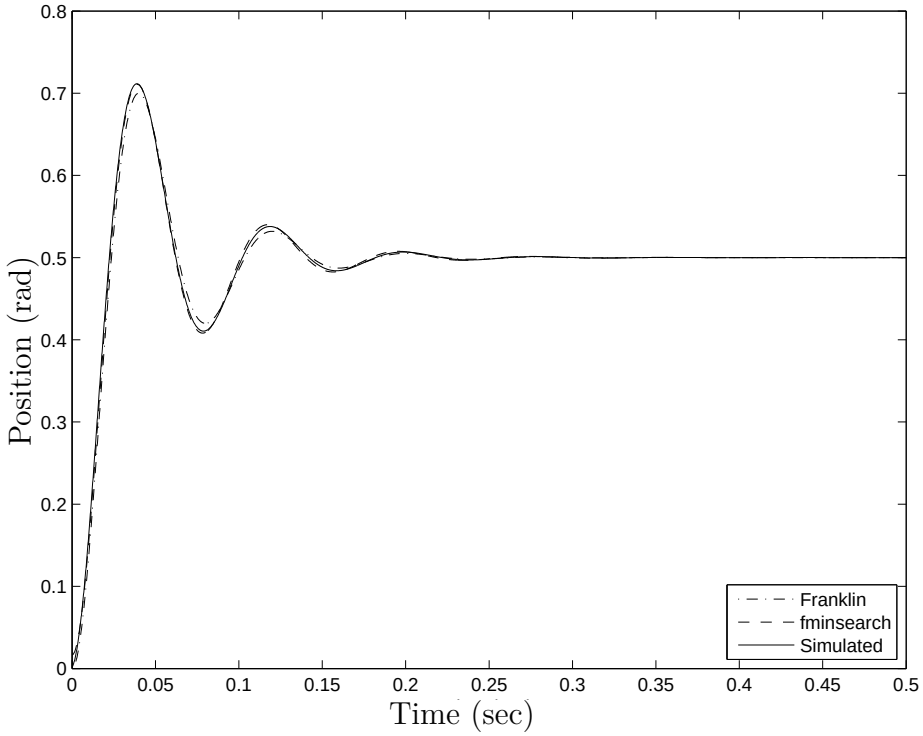

Figure 5.30: Simulated step response of the 2 DoF DDA model. When constructed such that the support bearing has very little stiction, the output settles close to the desired value even under P only control.

ter 3] describes how such an estimation may be made, by measuring the overshoot and rise time of the response to compute estimates for parameters ω_n and ζ. A second method uses the *fminsearch* function in MATLAB (shown in Appendix B3) to find a suitable pair of values for the same parameters, by minimising the sum of the square of the residuals between the actual step response and the simulated second order response.

The response of the estimated transfer functions appear to closely resemble that of the drive simulation, however due to the presence of high levels of Coulomb friction, the simulated output comes to a halt prematurely and results in a steady state error. This is characteristic of all geared actuators, and it is the main driving force behind the large body of research into control systems that mitigate this effect.

The step response of the 2 DoF DDA model also follows the second order characteristic step response, in fact it is possible to match these very accurately using the

two estimation methods, as shown in Fig. 5.30. Furthermore, as the support bearing exhibits very low levels of static friction, the position of the output settles very close to the reference position.

5.5 Summary

As outlined in the previous chapter, the DDA operates with the two rotors continuously spinning. This means that under controlled conditions interface velocities are always much greater than the threshold for stiction to occur and also large enough to clear the Stribeck region. In this area of operation the friction forces are purely viscous and therefore linear in nature. An important aspect of operation is the idle velocity of the rotor. If this velocity is too low, one or both motor velocities may approach zero in operation and the output will experience non-linear behaviour. If, however, the velocity is selected to be very high, the power required to combat viscous friction of the drives will be wasted and the efficiency of the actuator falls.

For the simulation as shown in this chapter, the friction profile of the bearing is highly exaggerated. This is to demonstrate the effects it may have on the DDA. Practical bearings have much lower Coulomb friction coefficient and hence - although not insignificant - the overall contribution is small when compared to that provided by the gearbox of a single actuator.

When constructing the DDA system, care must be exercised when selecting a coupling method. The drives may contribute a high amount of friction through gearboxes which result in dissipating energy and hence vibrations will not occur. However, in configurations which lack gearboxes and feature low friction drives, a couplings with low stiffness and low inertia should be avoided.

The closed loop behaviour of the 2 DoF model predicts a second order response of the output of the DDA. This is expected as this model only captures a very simplified

dynamics of the whole system. Higher order models have not been simulated due to the difficulty in parameterising the models correctly. This deficiency is highlighted in the future works section and should be carried out to aid controller design for industrial applications.

Chapter 6

Experiments and results

The previous chapter presents a number of simulation results of the functioning of the DDA. These demonstrate that the friction behaviour of the output of the DDA is solely viscous in nature and non-linear effects are governed only by the output bearing. This chapter presents a physical implementation of the system, along with experimental results of its behaviour. Example application of position control and a haptic wall is presented to demonstrate the characteristics of the system.

6.1 Test bed construction and properties

The DDA can generally be constructed using two drives coupled together by their rotor. Gearboxes may also be incorporated. A practical implementation is shown in Fig. 6.1.

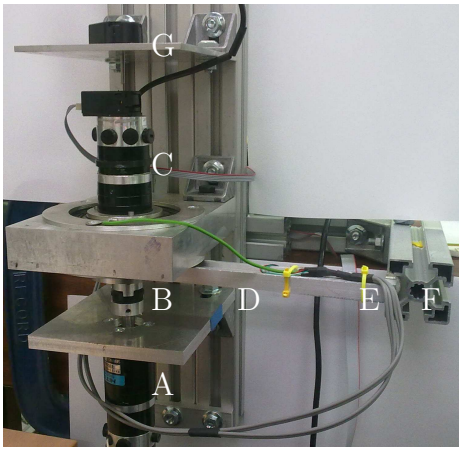

Figure 6.1: Experimental setup

Two *harmonic drive* servo actuators (A and C) are coupled together (B) in a vertical configuration to eliminate load torques due to gravity. The primary drive (A) is fixed to the rail, and the secondary drive (C) is attached to the same rail through a support ball bearing. The arm - which is attached to the stator of the secondary drive (D) - is fitted with a load cell (E) for tip-force measurements. Both drives are fitted with incremental encoders along with a third encoder (G) fitted for measuring the output arm angle. The load cell may come into contact with the rigid bar (F) or may be held by hand and load torque T_L can hence be introduced.

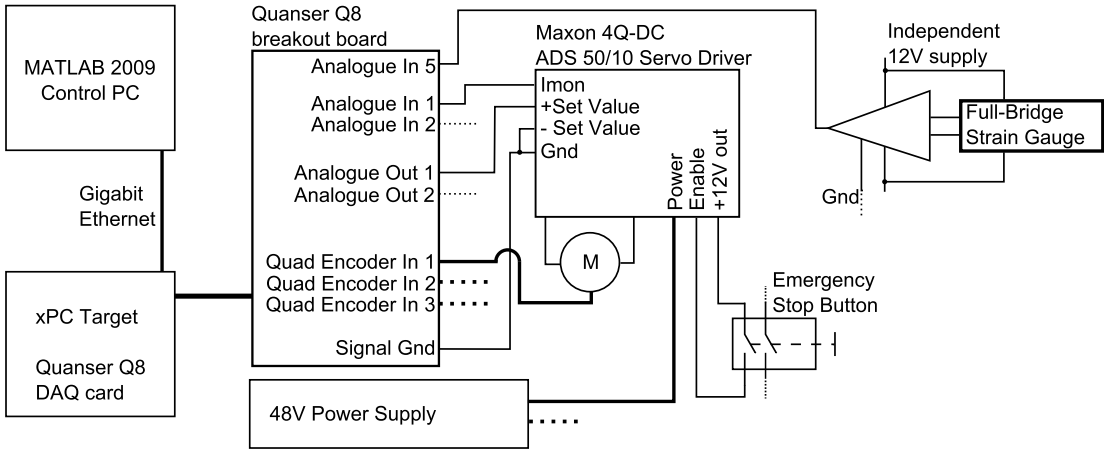

Figure 6.2: Connection diagram of experimental system

Two Maxon current mode motor drivers amplify the control signals provided by a personal computer running xPC Target outfitted with a Quanser Q8 data acquisition

board as shown in Fig. 6.2. For clarity, one only drive is shown attached to analogue input and output channels 1, the second drive is attached to channels 2 respectively. The strain gauge amplifier, powered independently is connected to analogue channel 5. The two motor encoders (A) and (C) are connected to encoder channels 1 and 2, the overall output encoder (G) is attached to encoder channel 3. The motor drives are supplied by a 48V power supply and an emergency stop latching switch is included for safety.

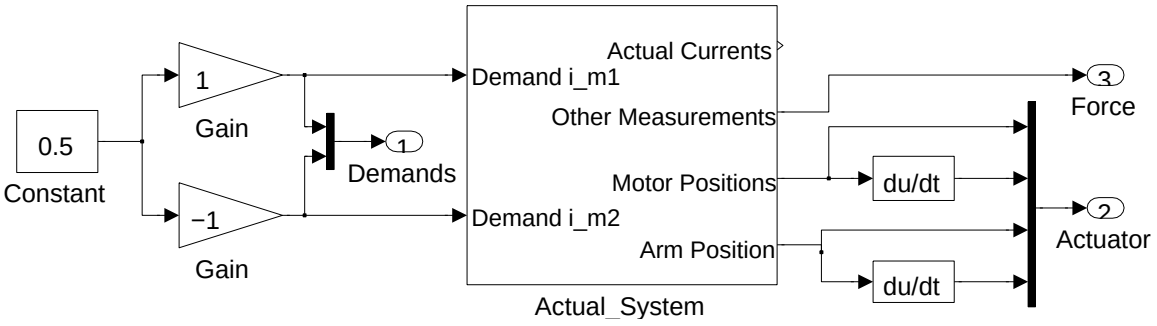

Figure 6.3: Simulink model for data acquisition

Figures 6.3 and 6.4 show the Simulink model used to drive the system and to acquire data. Due to the settings of the motor amplifiers, the gain and offset are tuned for each driver such that the actual measured current are the same for a given demand value from the Quanser Q8 board.

Load force F_a at the tip of the actuator is applied manually. The force is measured by the load cell, amplified by a strain gauge amplifier and fed to the Quanser Q8 board along with the two motor and arm position measurements. The torque produced by the arm is $T_L = F_a d$, where d is the distance between the rotor and the force sensor.

The Simulink model is a discrete model with step size of 1 ms, measurements are saved into xPC Target output space using the sink *out* blocks. The values recorded include acquisition time, current demands and raw current measurements, strain gauge measurement, motor and arm positions and velocities.

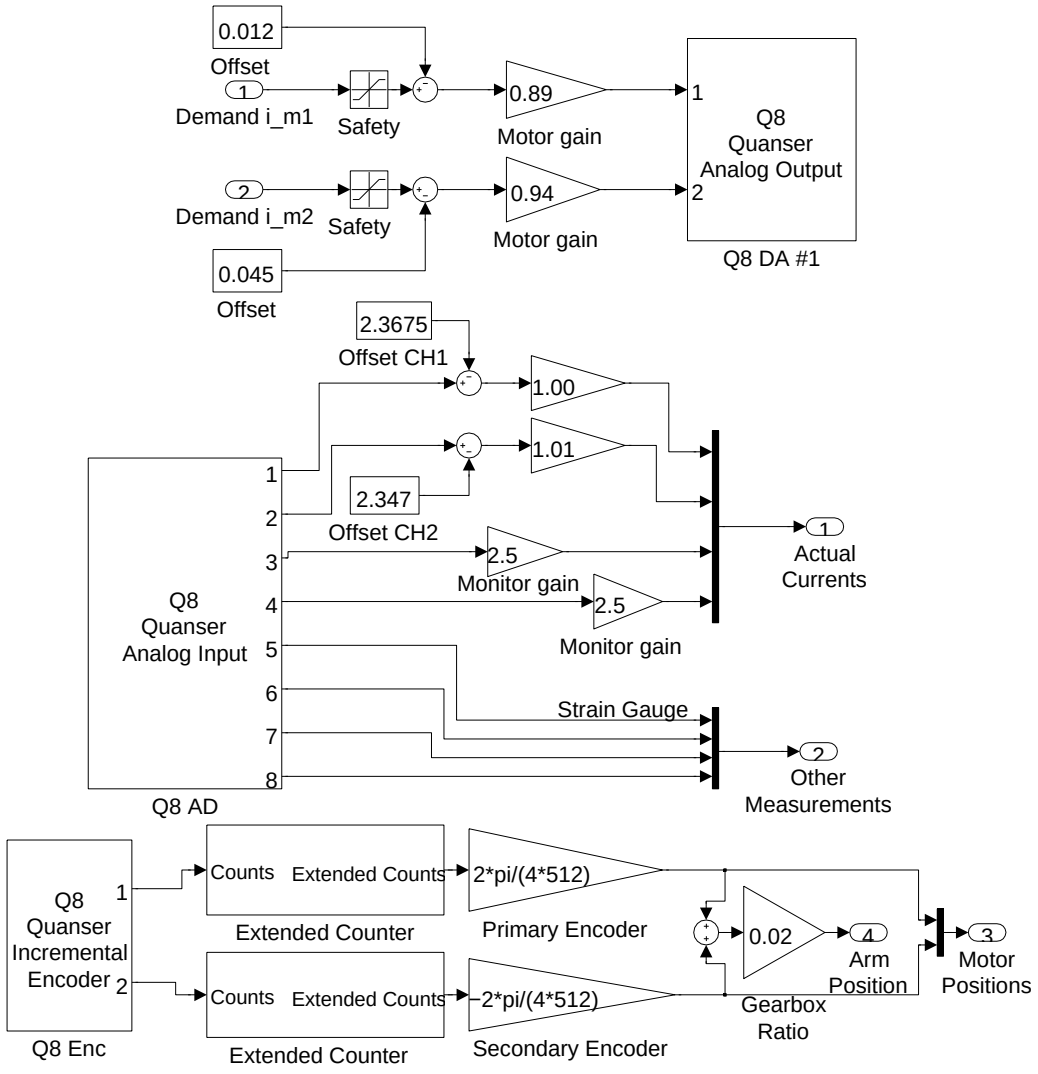

Figure 6.4: Simulink model for data acquisition, detail of block ActualSystem

6.2 Unpowered behaviour

When the system is supplied with no power ($v_m = 0$V), all components are at rest. When a torque is applied at its output as shown in Fig. 6.6, the friction experienced is the result of the superposition of all friction present in the system. The applied torque has to overcome the stiction in the output bearing, the secondary drive and the primary drive. As expected, the response is therefore highly non-linear. The presence of Coulomb friction is evident in the velocity-torque plot shown in Fig. 6.6b, where there is a discontinuity near the zero velocity region. This effect is also visible in the position-applied torque plot shown in Fig. 6.6a. The viscous friction effects are also visible, showing the characteristically high value for a harmonic drive gearing. The simulation results with altered parameters as presented in Fig. 6.7 compare directly with the experimental results shown in Fig. 6.6.

During operation however, the power applied to the system keeps the rotor at a constant non-zero velocity. When torque is applied the output, the motor velocities change as shown in Fig. 6.5.

The behaviour is most readily comparable to that of Fig. 5.16a. The secondary drive experiences greater velocity as the load rotates its stator. These findings are consistent with the highly non-linear friction model presented in Section 5.

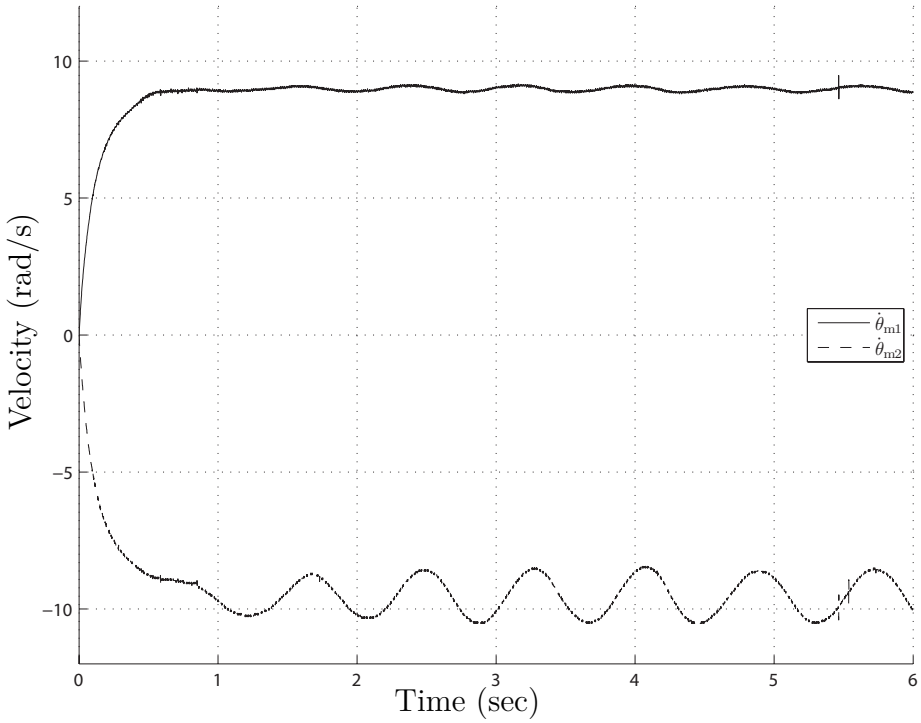

Figure 6.5: Dual Drive Actuator transient response. Open loop operation, drive motor current is at 200mA. Motor velocities are affected by the externally applied load torque.

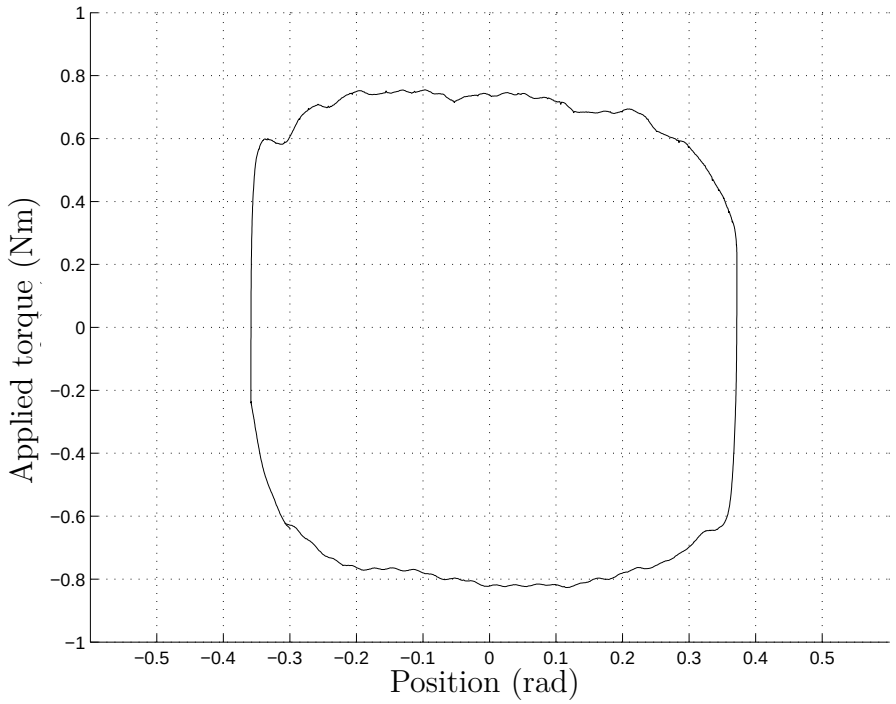

(a) Applied torque / Load position

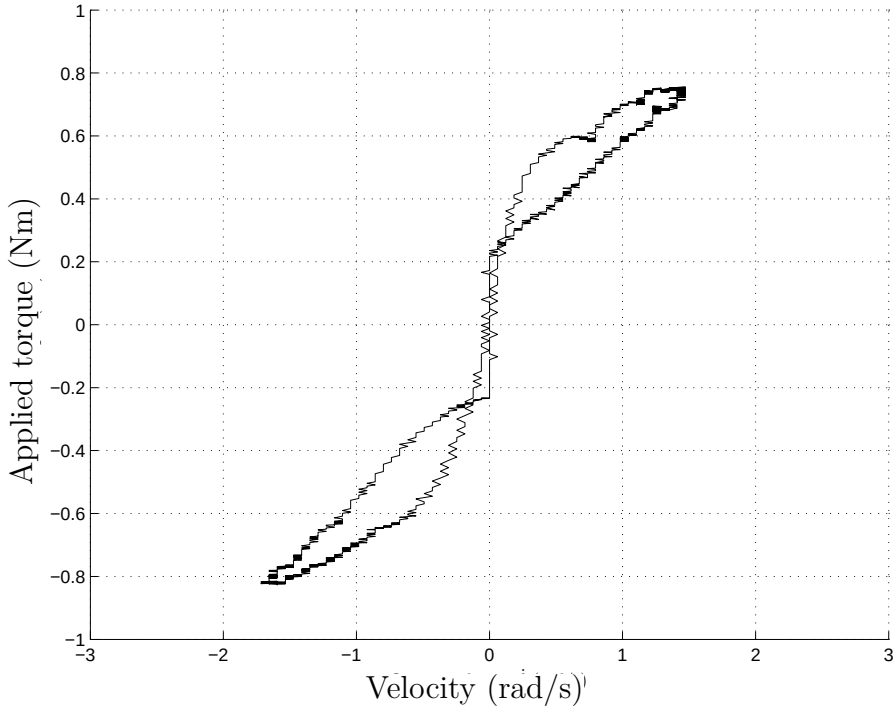

(b) Applied torque / Load velocity

Figure 6.6: Measured Dual Drive Actuator output response to an applied cyclic load torque - No power applied to the drives yield a friction profile consistent with the non-linear friction model

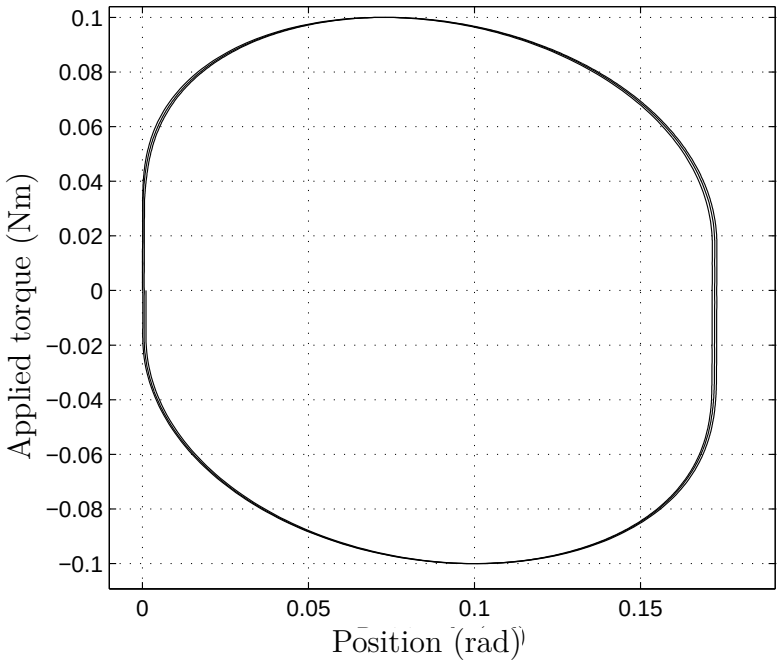

(a) Applied torque/Load position

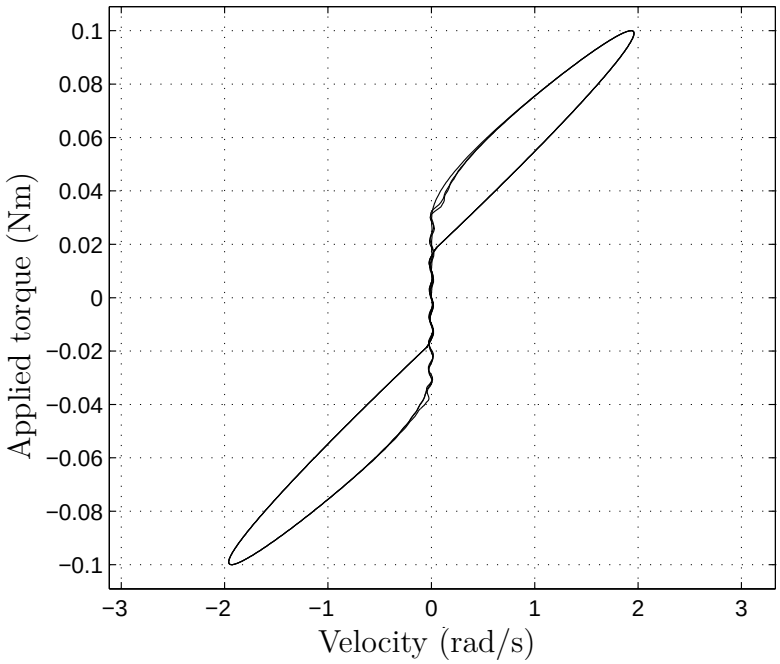

(b) Applied torque/Load velocity

Figure 6.7: Simulated Dual Drive Actuator output response to an applied cyclic load torque - As the drives are not running, the resulting friction profile is exhibits non-linear behaviour with a high Coulomb coefficient

6.3 Powered behaviour

Once power is applied to the system, the output exhibits linear friction properties as shown in Fig. 6.8.

Fig. 6.9 shows the simulation result of the same 4 degree-of-freedom model. The simulated response is a good match to that of the physical system, although some some parameters are still incorrect.

Fig. 6.8a shows the position/torque profile of the output of the physical actuator. It closely resembles that produced by the simulation as shown in Fig. 5.10a. However, the harmonic drive gearing introduces a position dependent component of torque transmission ripple, which has been a topic of research by Tuttle et al. [15]. This property is not included in the simulation model, hence it is not observed in the simulated response.

Fig. 6.8b shows the velocity/torque profile of physical system. It also closely resembles that produced by the simulation in Fig. 6.9b, however it is more difficult to ascertain the actual shape of the response due to measurement noise. This is the result of the velocity being estimated from the measured position.

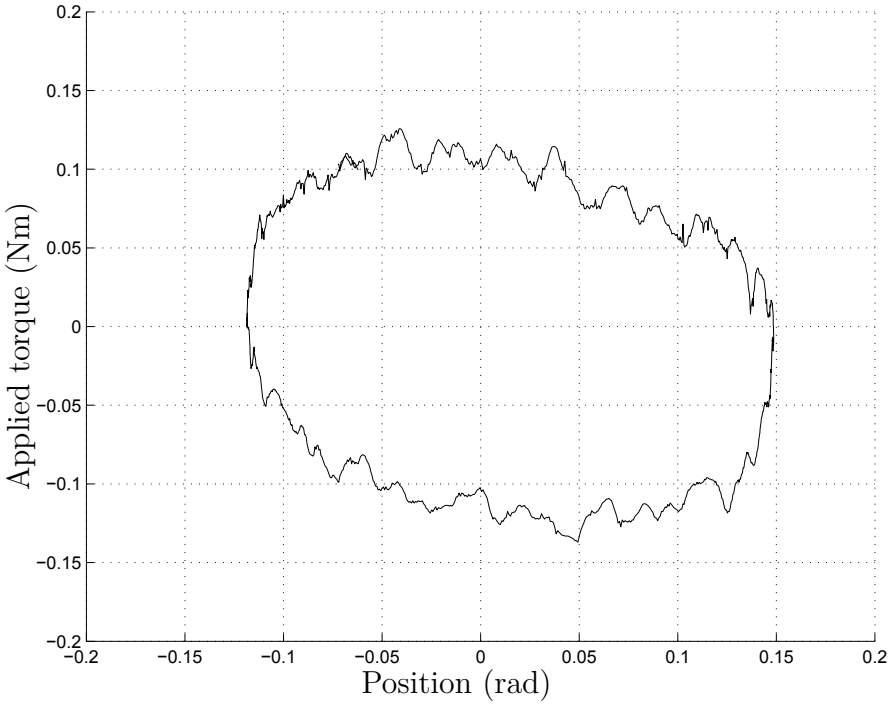

(a) Load position/Applied torque

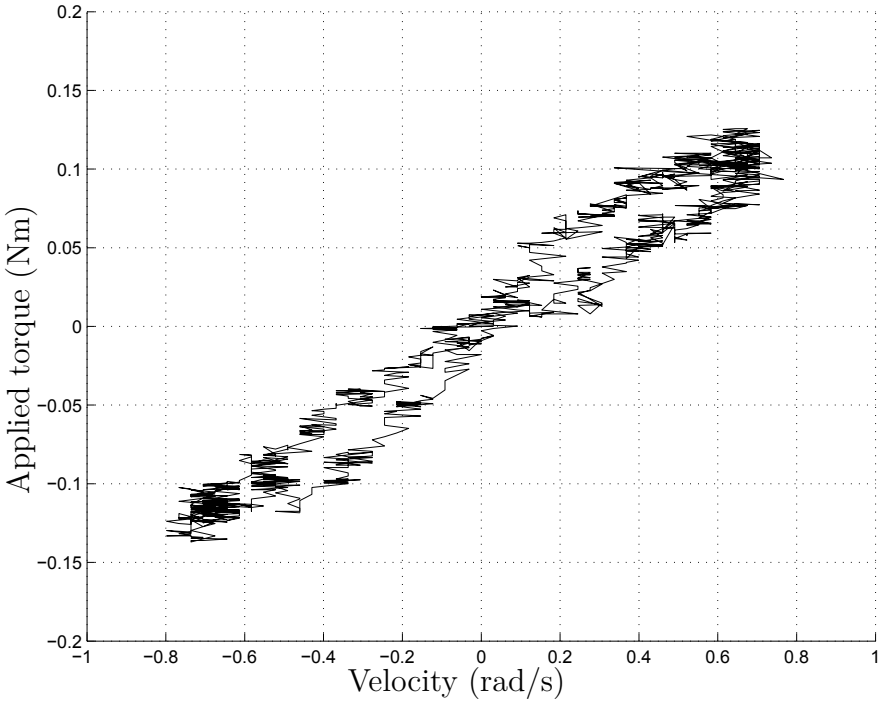

(b) Load velocity/Applied torque

Figure 6.8: Measured response of the Dual Drive Actuator to an externally applied load torque, drives supplied with $V_m = 9$V

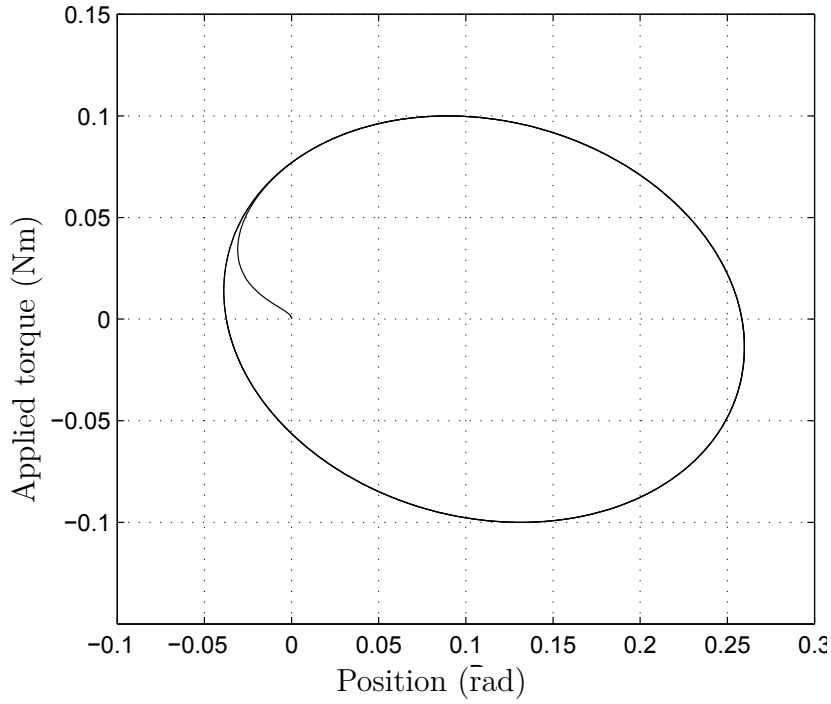

(a) Position/Applied torque

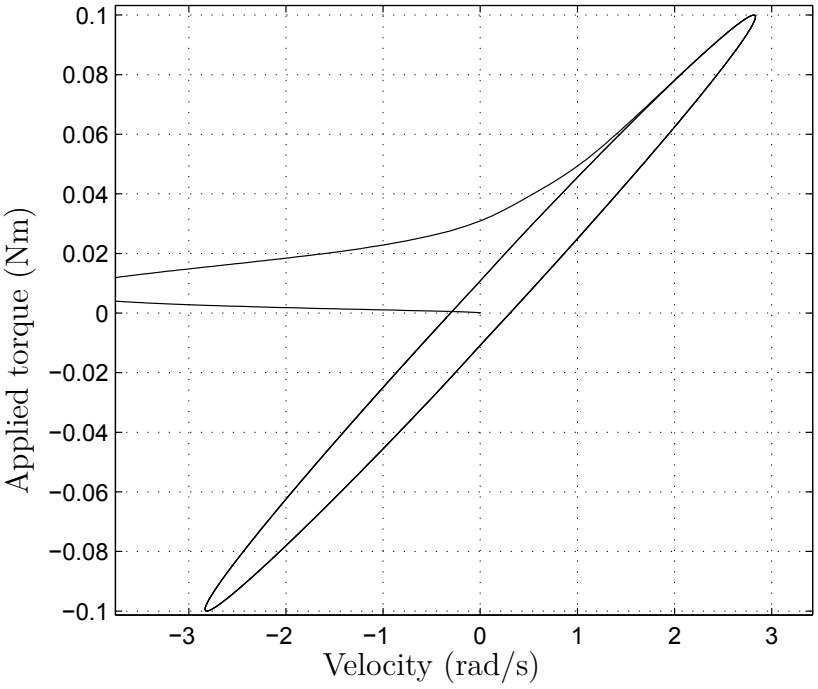

(b) Velocity/Applied torque

Figure 6.9: Simulated response of the Dual Drive Actuator to an externally applied load torque - simulation parameters of $K_c = 1000\text{Nm/rad}$, $J_c = 1e^{-6}\text{kgm}^2$, $V_m = 9\text{V}$

6.4 Closed loop analysis

As single drive actuators are prevalent in most robotic applications, such an actuator provides a good basis for comparison. Such an actuator is constructed from a drive and usually a gearbox. As discussed in Chapter 2, this arrangement may suffer from high levels of friction and non-linearities including backlash and stiction. As the DDA is prototyped using harmonic drive actuators, the same construction may be utilised for single drive applications. Simulink model as shown in Fig. 6.10 shows a SDA position controller. Either the primary or secondary drives may be 'locked' in position, meaning that an independent position loop is applied to that drive.

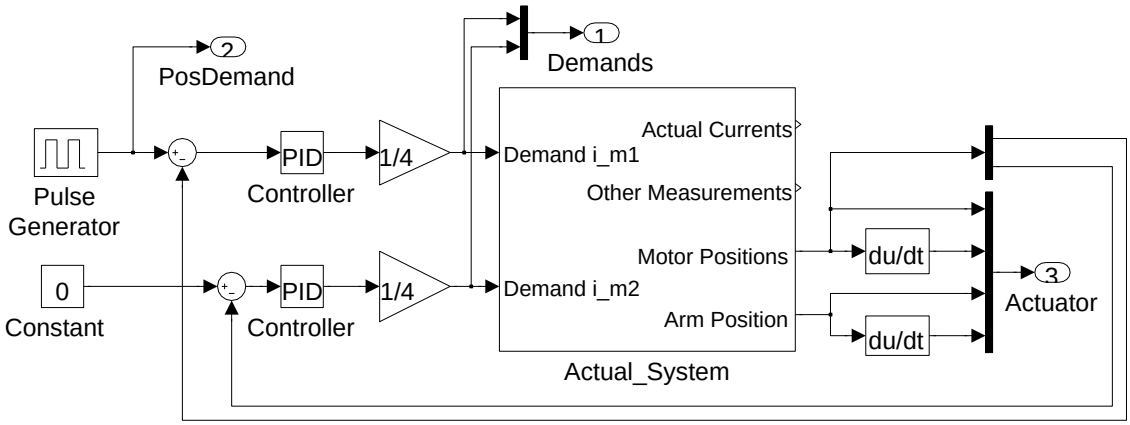

Figure 6.10: Simulink model for position control of a single geared actuator

A reference position signal is applied to the other position loop and the results of a step input is shown in Fig. 6.11. As the response appears to exhibit characteristics of a second order system, an equivalent second order transfer function may be derived for comparison. Similarly to the way described in Chapter 5, an estimate may be made using Franklin's method from the measured overshoot and rise time of the response. The second *fminsearch* method is also utilised to find a suitable pair of values for the parameters ω_n and ζ.

As can be seen in Fig. 6.11, the two estimated responses do not correctly capture the dynamics of the SDA. Although the rise time and overshoot are within 1% of that

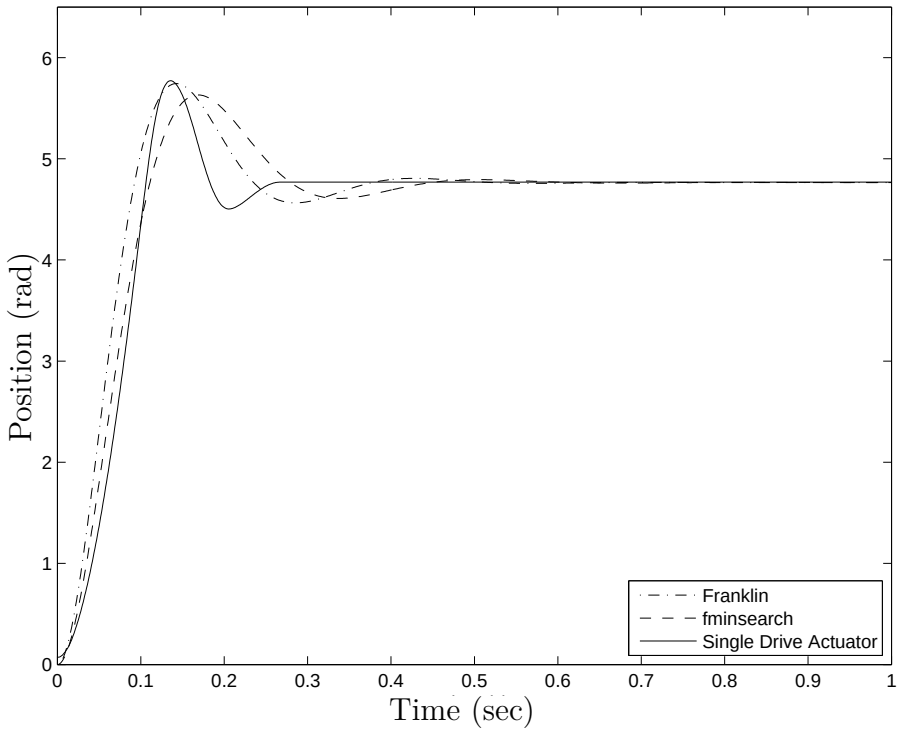

Figure 6.11: Position step response of a Single Drive Actuator constructed using a harmonic drive Actuator, along with estimated equivalent second order step response curves. Output in steady-state error to reference step size of 5 rad.

of the actual response, the settling time for both estimated systems are much longer. This is a typical result for systems where non-linear friction effects are dominant. In the case of the SDA, the harmonic drive gearbox presents high Coulomb and viscous friction and the output comes to rest in the vicinity of the required position thus leading to steady-state error. It is also apparent that the step response of the system is not purely second order, as convergence to the final value is faster than that of a second order system. This is the result of the second 'locked' position loop in the construction of the SDA, along with the unmodelled dynamics of the motor electrical circuit and amplifier.

An example position controller for the Dual Drive Actuator is shown in Fig. 6.12. This model utilises a single position feedback loop to create symmetric control signals that are fed to each drive simultaneously.

Two second order equivalent transfer functions were found using the same meth-

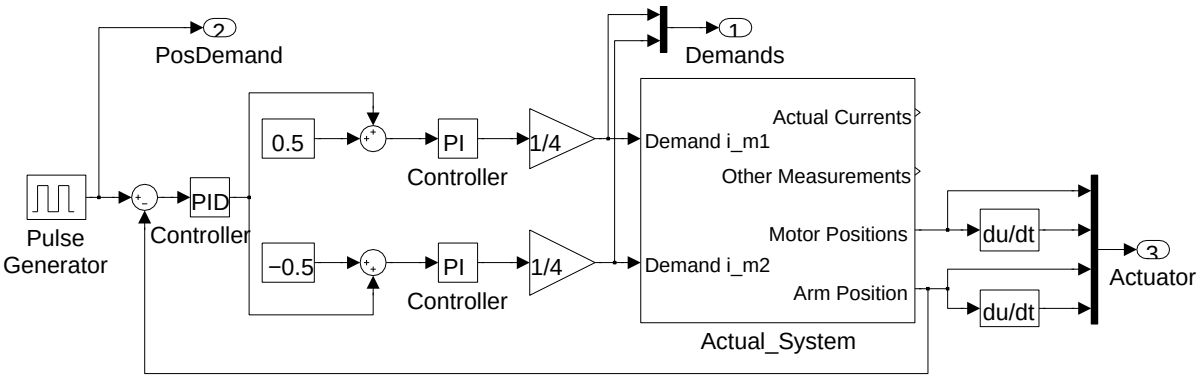

Figure 6.12: Simulink model for position control of a Dual Drive Actuator

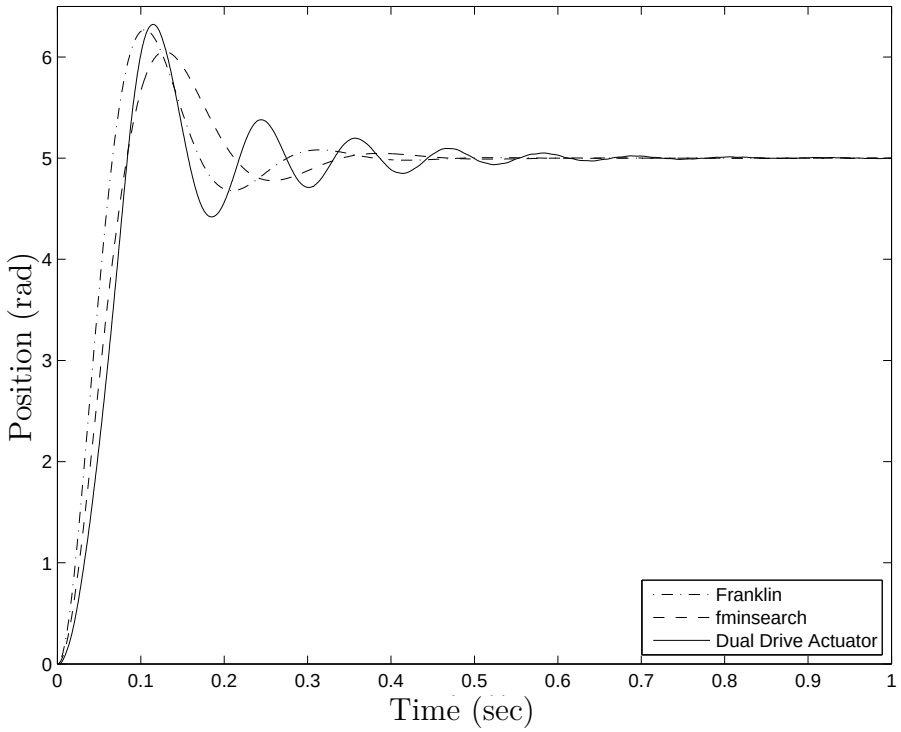

Figure 6.13: Position step response of a Dual Drive Actuator constructed using harmonic Drive Actuators, coupled using an Oldham coupler. Output settles at the reference step size of 5 rad.

ods as in the case of the SDA. It is notable, however, that the DDA exhibits very much reduced friction and the output takes a longer time to settle than it does in the case of the SDA. This is a direct consequence of the output friction linearisation and is therefore a desirable effect.

Both estimated second order response curves under-predict the overshoot and

do not capture the longer settling time of the actual system. The measured response exhibits higher order characteristics as expected from the mathematical models in Chapter 4, however the estimated models still provide useful a useful measure as the basis for comparison.

Table 6.1: Model values for the simulated equivalent transfer functions

		SDA	DDA
Actual System	Overshoot (%)	20.93	26.36
	t_r (sec)	0.073	0.055
Franklin equivalent	ω_n (rad/s)	24.65	32.72
	ζ	0.450	0.400
	Overshoot (%)	20.40	25.45
	fit	1653	132.1
fminsearch equivalent	ω_n (rad/s)	21.20	27.22
	ζ	0.477	0.444
	Overshoot (%)	18.05	20.99
	fit	1146	78.13

Although the SDA exhibits a much shorter settling time than the DDA, it suffers from highly non-linear friction and there is a steady state error in output position. The DDA takes longer to settle due to having a linear output friction characteristic, but tends to a very small steady state error, even under P only control. Both controller values were found in an iterative process of increasing the P gain until sustained oscillations are found, then reducing the gain by 10%. The rise time and therefore bandwidth of the DDA appears to be higher than that of the SDA by around 32%, which is the result of the output again experiencing linear friction around zero velocity and hence the time delay between an actuation command and response are much reduced.

6.4.1 PID position control

Many robotic actuators utilise the well-established linear PID controller as the basic form of position controller. A classic heuristic tuning method for PID controllers is Ziegler-Nichols method [108], which was applied to both the SDA and DDA. The the results of a tuned position controller for an SDA is shown in Fig. 6.14. The position response of the DDA is shown in Fig. 6.15b. The drive and scaled output velocities are shown in Fig. 6.15a. The scaling of the output velocity is necessary as it is very small compared to the two drive velocities.

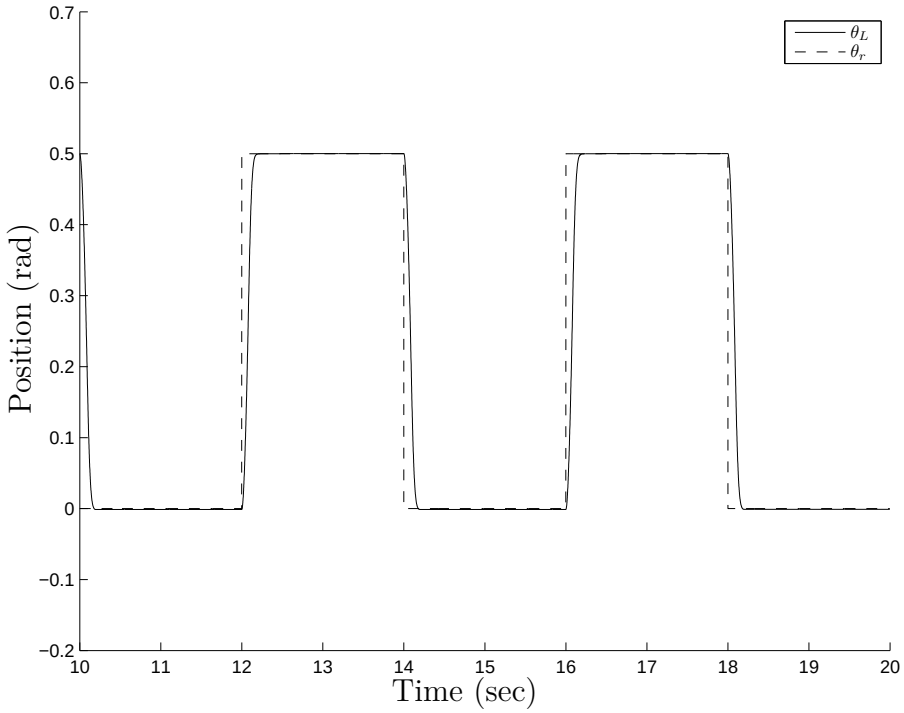

Figure 6.14: PID Position control step response of a single harmonic drive actuator

As can be seen, the SDA yields a response with no overshoot and once settled, the output remains stationary. The DDA however retains a slight overshoot of 2% and the output, although is within 1% after the settling time, remains in constant motion about the reference position. This behaviour is largely due to the highly position-dependent friction behaviour of the harmonic drive gearbox, and is also the result of low friction forces at the output.

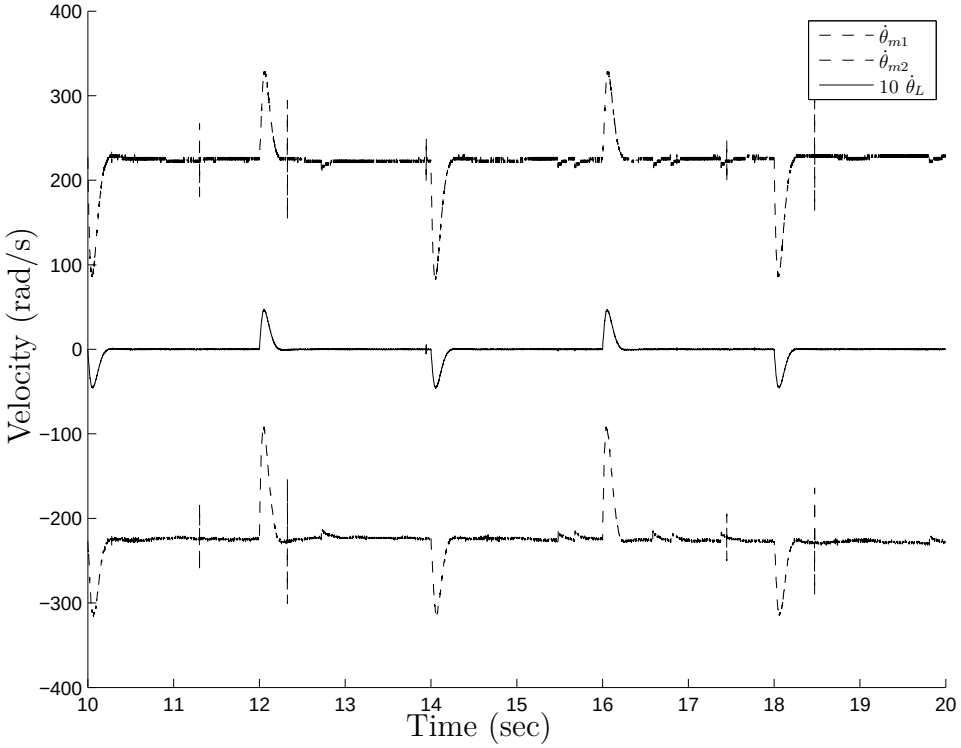

(a) DDA drive and output velocities

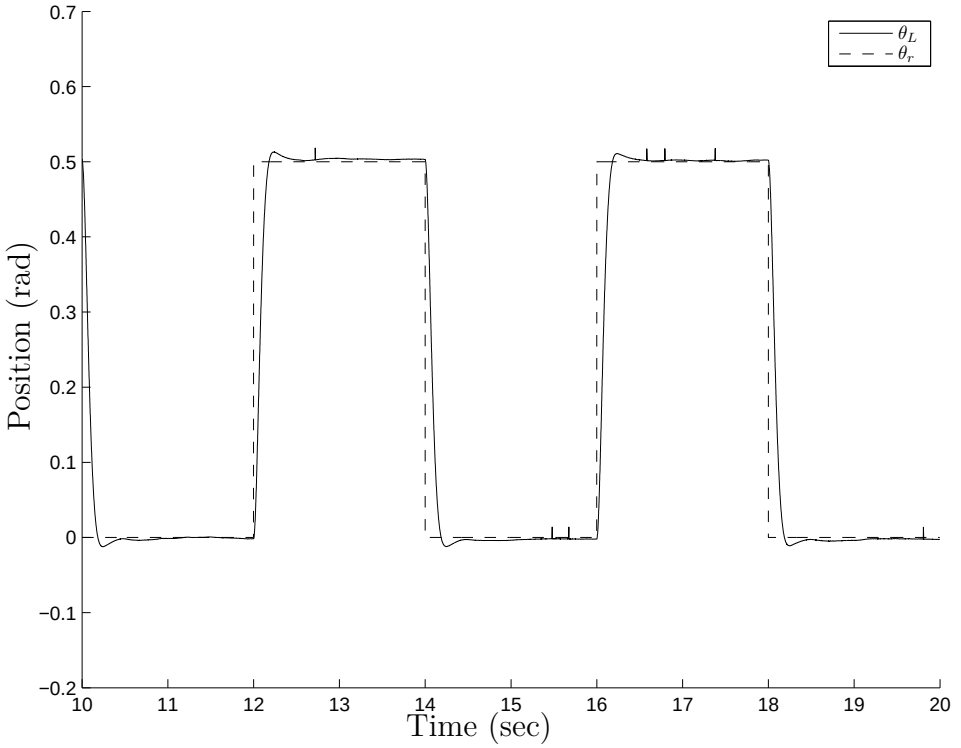

(b) DDA position response

Figure 6.15: Position control step response of a Dual Drive Actuator

6.4.2 Example Application - A haptic wall

A common field in robotics is haptic actuation, where the robotic manipulator is coupled to a human operator at its end effector and provides force feedback. In such applications, a controlled amount of torque must be developed by the robot to act on the operator. This may be accomplished using impedance control, where the user's motion is resisted by the manipulator. An example control law would be

$$F = k(x_d - x_m) \tag{6.1}$$

where F is the force applied by the robot, x_d is the desired and x_m is the actual manipulator position, and k is a constant. This equation effectively models a spring force F with stiffness k. An example haptic application is a haptic wall, where the user is free to move until a contact with the wall is encountered. If the user pushes towards the wall and contact is made, the manipulator applies Eq. 6.1 control law and develops a spring force to push the arm back 'out' of the wall. The most basic haptic interface requires only one degree of freedom and so the test bed construction of the SDA and DDA are suitable for such an application.

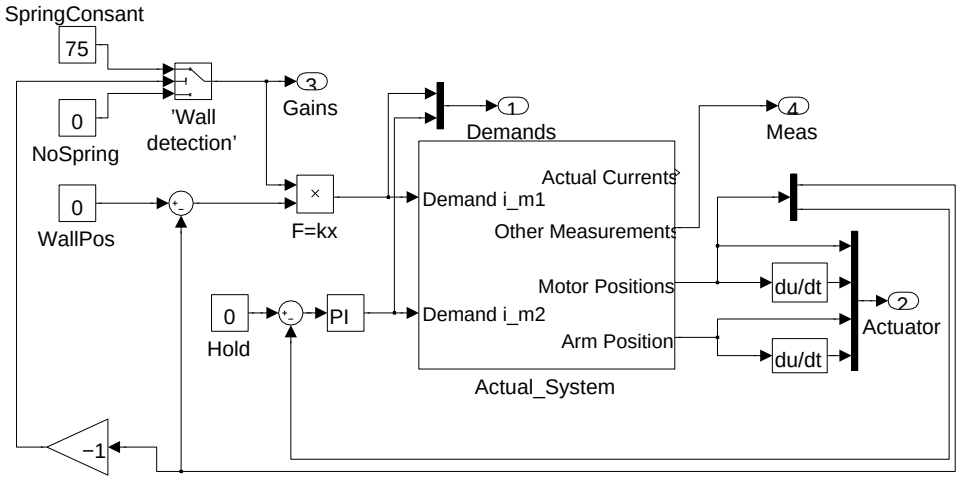

Figure 6.16: Haptic wall controller for a Single Drive Actuator. If the sensed position is less than zero, then a motor torque proportional to distance is applied

The controller for the SDA is shown in Fig. 6.16. The reference wall position

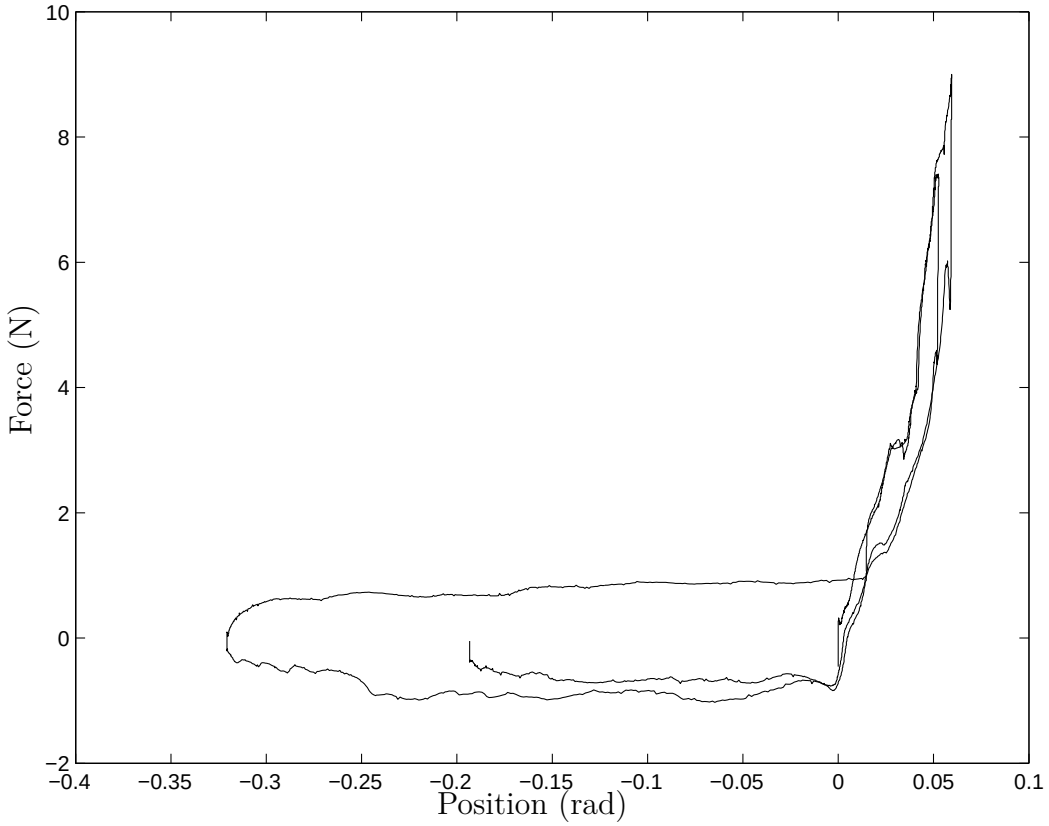

Figure 6.17: Position/Force response curve of the Haptic Wall using a Single Drive Actuator. The high levels of friction is evident in the large forces required to move the actuator arm when not in contact with the wall.

is set at 0 rad, any negative excursion by the actuator arm is unresisted and zero torque is applied to the motor as k is switched to zero. However, if the arm position increases past 0 rad, the controller is activated by assigning a value to k.

This model utilises a P controller, as this approach exactly describes Eq. 6.1, with $x_d = 0$ and yields $F = -Px_m$. As this is an SDA simulation, a second position loop is applied in order to 'lock' the other drive of the DDA. Any effect of the dynamics of this loop if negligible on the output. The response of the SDA is measured using the force sensor at the end of the effector arm and is shown in Fig. 6.17. The arm is first pushed into the wall, then taken out of it and then return.

The same controller can be extended to the Dual Drive Actuator as show in Fig. 6.18. In this case the control signal, once formed are fed to both drives to alter the

current demanded from each. The imbalance in drive current results in torque being applied to the arm to counter the externally applied force. Hence the DDA is suitable for haptic applications.

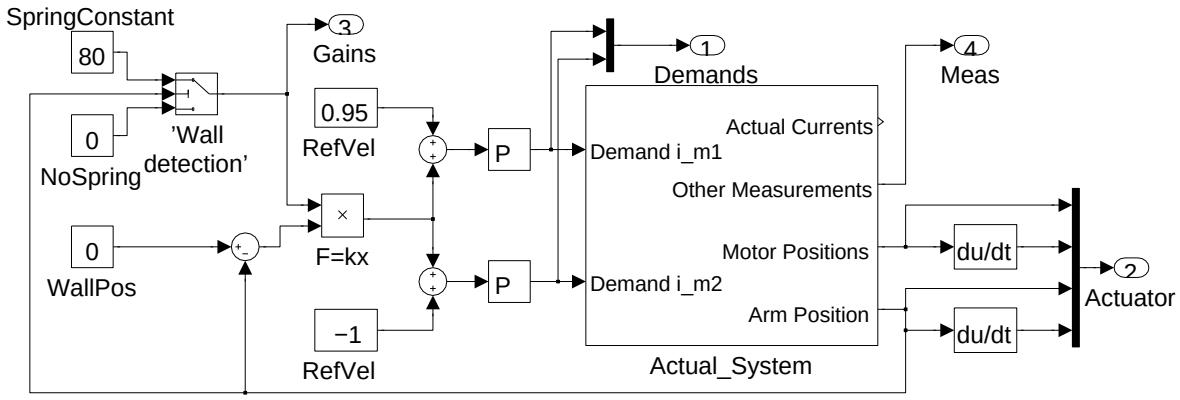

Figure 6.18: Haptic wall controller for a Dual Drive Actuator. The control signal is fed to both drives to cause an imbalance in torque production, which yields the actuator output torque.

The position/force response of the DDA as shown in Fig. 6.19. Although the spring-like behaviour of DDA closely resembles that of the SDA, the 'free space' behaviour is significantly different. Whereas the SDA becomes un-powered when no force is required to be produced and hence its friction must be overcome by the user; the DDA actively linearises and minimises the effects of friction around low output velocities. Hence the force applied by the user outside of the wall is substantially smaller.

Force measurement values are mostly artefacts of electrical and measurement noise, and are less than 10% that exhibited by the SDA. Contact with the wall in both cases result in high forces, although the relative change in force in the DDA yields a more convincing experience. The transition from a very low reaction force of free-space motion to a stiff surface is more pronounced. Using the SDA, the transition yields a change of reaction force of around 200, with the DDA this increases to around 2000. The perceived fidelity of the simulated wall is therefore higher.

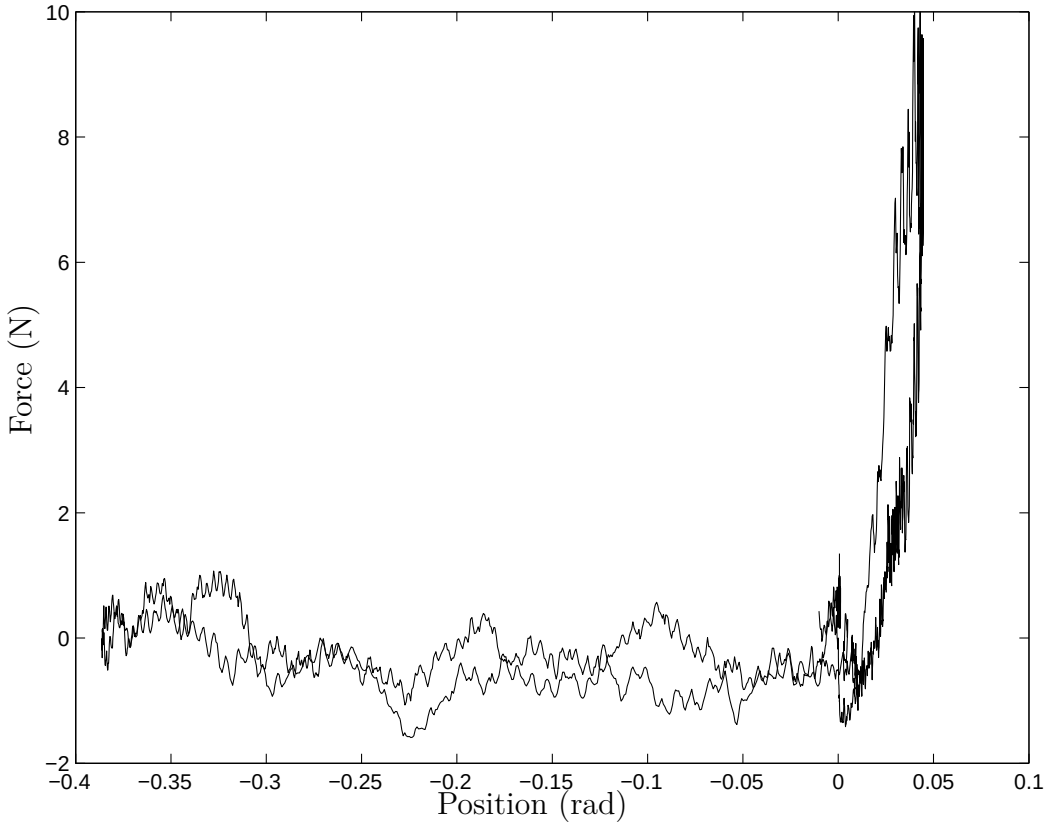

Figure 6.19: Position/Force response curve of the Haptic Wall using a Dual Drive Actuator. The output arm experiences very low friction levels at low velocities when not in contact with the wall, as consistent with the analysis in Chapter 5.

6.5 Summary

A Dual Drive Actuator may be constructed using any direct drive or geared actuators by combining their rotors. The test bed utilises two harmonic drive actuators that can deliver high torque and eliminate backlash at the expense of greatly increasing both Coulumb and viscous friction in each drive. This chapter demonstrates the effect of the DDA arrangement on such drives; once powered up the overall output is shown to exhibit viscous only, linear friction.

The step response of the SDA and DDA are compared using estimated second order equivalent transfer functions. Although both SDA and DDA exhibit higher order response characteristics, a second order response is largely representative of the overall closed loop response of both systems. It is found that the DDA has a higher

bandwidth and much reduced friction related effects when compared to the SDA, which implies its usefulness in robotic applications.

A simple haptic application is also presented where the operator can push the actuator arm against a virtual wall. It is found that the DDA performs equally well in creating haptic feedback, and it excels in free-space motion as friction of the actuator arm is much reduced when compared to the SDA.

This chapter demonstrates that the DDA may be utilised in a number of different areas in robotics successfully.

Chapter 7

Discussion and Conclusions

The field of robotic actuation has seen a great deal of research into friction dynamics, modelling and compensation thereof. As described in Chapter 2 the phenomenon of friction is complex and hence there are a number of models of varying degree of complexity describing certain aspects of it. It has been found that compensation schemes struggle to provide a robust solution to eliminate these non-linear effects. Those that are successful still exhibit certain undesirable properties, which means that in certain applications they are unsuitable and may lead to additional problems.

Apart from friction, actuators may also suffer from backlash, which in most circumstances may be mitigated by design or through the application of certain types of gearing. There are also effective compensation methods available, although similar to friction compensation, they are also not universally applicable. Together these two characteristics have a major impact on the performance of any robotic manipulator. In certain tasks, such as free motion, these effects may be negligible. However, most industrial processes require the manipulator to come into contact with its environment, when the effects become considerable.

In theory, if actuators with strictly linear friction profile were used to construct the manipulator, then currently difficult problems - such hard contact tasks - would

become more feasible. The cause of most of the non-linear effects in friction is that the relative velocity of the surfaces in contact reduce to zero. If motion were maintained at all times, friction would reduce to simply viscous - hence linear - in nature.

Dual drive actuators are constructed for very specific purposes, usually forming a higher bandwidth device over what would be possible with either of the drives by themselves. By exploiting the nature of redundancy within the actuator, it is possible to isolate a friction surface which is kept in continuous motion. By configuring the actuator as shown in Chapter 3, the combined rotor can be kept rotating even when the output comes to a halt. As neither the base nor the output experiences zero relative velocity to the combined rotor, the friction forces arising will tend to be only linear in nature.

As two drives are present in the actuator, the nature of their coupling plays a role in shaping the performance of the actuator. Three mathematical descriptions are derived that are each shown to be capable of capturing the linear response of the system. The lowest order model captures the basic behaviour of the actuator, whilst the higher order models take into account the dynamics of the coupling for the drives.

Simulation results are presented in Chapter 4, first by demonstrating how Coulomb friction is a main contributor to the observed output friction dynamics. Then the dynamics of the proposed actuator are investigated. Experimental results are then shown in Chapter 5. The theoretical and empirical results are compared with the findings as follows.

7.1 Main findings

As previously demonstrated, each model captures the key behaviour of the actuator and hence the models are correct.

- Every model predicts that the *output friction to be linear when the support bearing introduces no additional non-linear friction effects*. This may be achieved using air bearings in practice, or ball bearings with low friction. The latter will suffice in most applications as the major source of non-linear friction - in the gearbox and the drive motor - is linearised.

- *The presence of coupling between the two motor inertias predicts vibrations*. This is found to be the case in the four degree-of-freedom model with small coupling inertia. Very high coupling stiffness ($K_c = 1000$Nm/rad) leads to a small amplitude high frequency oscillation, and relatively low stiffness - such as provided by a helical coupling - allows for very low frequency and small amplitude oscillation. Both of these die down due to the effective damping provided by the friction present in both drives. However, a coupling is stiffness of $K_c = 600$Nm/rad leads to undamped high frequency, large amplitude vibration of the coupling. When the inertia of the coupling is increased, the oscillations reduce in amplitude and in frequency, as expected.

- The results form the physical system compare well with the simulation results. The general shape of the velocity-friction curve for both stationary and rotating rotors are very similar. The harmonic drive gearboxes provide a large amount of friction which, once the actuator is powered up, reduce to linear viscous friction as shown at the end of the previous chapter. There are discrepancies between the results in amplitude and torque, this is due primarily to the parameter selection of the model.

- *The idle velocity of the rotor appears to have little effect on the friction exhibited by the actuator*. Torque to overcome friction within the actuator are supplied by the two motors continually. When the output is at rest, these torques balance. The rotor velocity produces a friction torque as described by the linear viscous

term. Any perturbation of velocity produces a new friction torque that is also linear and of the same gradient at any velocity. Hence, the contribution of friction due to the change in velocity is the same, regardless of the idle velocity of the rotor.

- As the output position is determined by the mathematical sum of the two motor positions, *the current output position is readily available and requires no additional measurement*. Furthermore, as both motor velocities are measured at a relatively high rate, *position updates are available with greater accuracy* over ones that originate from the output directly. This means that the DDA should be highly applicable to contact tasks where the two major performance limiting factors are the uncertainty of position measurements and non-linear actuator friction.

7.2 Contributions to knowledge

The thesis presents a viable structure for a dual drive actuator for robotic and automation purposes.

- Suitable *mathematical models of the dual drive actuator for 2, 3 and 4 degrees-of-freedom models* are derived. Gearboxes can be incorporated into the design and hence torque magnification can be provided. A great benefit of this DDA design is that non-linear friction effects as contributed by the gearboxes are also linearised. This is a major improvement on geared single drive actuators which require complex friction compensation.

- The extent to which the *actuator linearises friction* is shown in both simulation and a practical implementation. The idle velocity of the combined rotor is demonstrated to have little effect on friction exhibited by the actuator.

- Stable control of the actuator is presented and its performance is compared to that of a single drive actuator.

- The actuator is shown to be applicable in a number of areas in robotics. In particular, it is demonstrated in a haptic wall application and the actuator may form the basis of more novel haptic devices.

7.3 Limitations of the work

The simulation results show that the mathematical models are capable of capturing the behaviour of the DDA.

- When compared to the actual physical system, the *simulation results differ* slightly. This is due primarily to the parameterisation of the models. Although more complex models may improve performance and prediction, there is marginal value in predictive power beyond the 4 degree-of-freedom model with Coulomb, viscous and Stribeck terms used. Although correctly parameterised, the 2 DoF model is capable of demonstrating the linearised nature of friction within the actuator, higher order models have not been parameterised due to the difficulty in obtaining a functioning set of parameters for these systems.

- During start-up, the *output may assume a high initial velocity* due to the motors experiencing different levels of friction and hence their acceleration rate are different as well. This requires careful consideration in practice as inclusion of devices such as brakes might contribute to the output friction and hence non-linear effects may return as these are external to the actuator.

- Although some examples of applications and results are presented in Chapter 6, the actuator is suitable for use in other systems. It is apparent that the *main*

challenge in applying the actuator is the structure and tuning of the controller and its parameters.

7.4 Future work

Better parameterisation of the model would yield a closer match in predicted performance and actual performance of the physical system. Techniques, such as system identification should be carried out on the physical system to ascertain parameters with higher precision. Also, non-linear programming and search algorithms could better tune the parameters using the knowledge of the actual physical system response.

The current investigation focuses on the DDA assuming a constant rotor velocity, which is unchanged in direction for both drives. It is, however, possible to lift this constraint and allow the reversal of velocity once the output inertia is non-stationary. During reversal, the output will experience an impulse torque due to the non-linear drive friction taking effect for a fraction of time. This impulse will have little or negligible effect on the output. The velocity reversal requires careful consideration as the selection and maintenance of constant idle rotor velocity has an impact on the response of the system.

A number of closed loop experiments have been carried out using the DDA. The actuator is a general purpose rotary actuator and hence it may be used in a multitude of systems under closed loop control. The viability of the DDA is demonstrated by the development and testing of closed loop position and haptic wall controllers. Once the DDA is established, properties such as highly accurate output position measurements can be exploited in hard-contact tasks. Also, as the design is inherently redundant, it may be used to implement the suggested control schemes in [75, 76] without adding more links than necessary to the manipulator.

The drives in the actuator are continually rotating and hence store mechanical

energy. This may be made available to the application as to create a more responsive output. Investigation into the implementation of controllers that exploit this possibility is strongly recommended.

Bibliography

[1] D. J. T. N. G. Hockstein, C. G. Gourin, R. A. Faust, "A history of robots: from science fiction to surgical robotics," *Journal of Robotic Surgery*, vol. 1, no. 2, pp. 113–118, 2007.

[2] A. Kuttan, *Robotics*. I.K. International Publishing House Pvt. Limited, 2007.

[3] C. J. J, *Introduction To Robotics: Mechanics And Control, 3/E*. Pearson Education, 2008.

[4] N. Mallon, N. van de Wouw, D. Putra, and H. Nijmeijer, "Friction compensation in a controlled one-link robot using a reduced-order observer," *IEEE Transactions on Control Systems Technology*, vol. 14, pp. 374–383, Mar. 2006.

[5] P. Atkinson, *Feedback Control Theory for Engineers*. London: Heineman Educational Books, 1978.

[6] D. Dudley, *Gear Handbook*. New York: The Macmillan Company, 1962.

[7] H. D. A. GmbH, "Harmonic Drive Product Manual," 1998.

[8] R. Maiti, "A Novel Harmonic Drive With Pure Involute Tooth Gear Pair," *Journal of Mechanical Design*, vol. 126, pp. 178–182, Mar. 2004.

[9] G. H. Benedict and B. W. Kelley, "Instantaneous Coefficients of Gear Tooth Friction," *A S L E Transactions*, vol. 4, pp. 59–70, Jan. 1961.

[10] A. Saada and P. Velex, "An Extended Model for the Analysis of the Dynamic Behavior of Planetary Trains," *Journal of Mechanical Design*, vol. 117, pp. 241–247, June 1995.

[11] Y. Michlin and V. Myunster, "Determination of power losses in gear transmissions with rolling and sliding friction incorporated," *Mechanism and Machine Theory*, vol. 37, no. 2, pp. 167–174, 2002.

[12] N. BAYDAR and A. BALL, "A Comparative study of acoustic and vibration signals in detection of gear failures using wigner-ville distribution," *Mechanical Systems and Signal Processing*, vol. 15, pp. 1091–1107, Nov. 2001.

[13] A. Singh, D. R. Houser, and S. Vijayakar, "Detecting Gear Tooth Breakage Using Acoustic Emission: a Feasibility and Sensor Placement Study," *Journal of Mechanical Design*, vol. 121, pp. 587–593, Dec. 1999.

[14] J. R. Colbourne, "The Law of Gearing," in *The Geometry of Involute Gears*, pp. 9–23, Springer New York, 1987.

[15] T. D. Tuttle, "Understanding and Modeling the Behavior of a Harmonic Drive Gear Transmission," tech. rep., Massachusets Institute of Technology, 1992.

[16] J. R. Phillips, "Computational geometry in the synthesis of skew gear teeth," in *Advances in Robot Kinematics*, (Dordrecht, Boston, London), pp. 101–108, Kluwer Academic Publishers, 1994.

[17] J. R. Phillips, "The Fundamental Law of Gearing," in *General Spatial Involute Gearing*, pp. 41–61, Springer Berlin Heidelberg, 2003.

[18] H. Olsson, K. J. Astrom, C. de Wit, M. Gafvert, and P. Lischinsky, "Friction models and friction compensation," *Eur. Journal of Control*, vol. 4, pp. 176–195, 1998.

[19] P. R. Dahl, "A Solid Friction Model," tech. rep., Space and Missile Systems Organization, 1968.

[20] C. de Wit, H. Olsson, K. J. Astrom, and P. Lischinsky, "A new model for control of systems with friction," *IEEE Transactions on Automatic Control*, vol. 40, pp. 419–425, Mar. 1995.

[21] C. C. de Wit and P. Lischinsky, "Adaptive friction compensation with partially known dynamic friction model," *International Journal of Adaptive Control and Signal Processing*, vol. 11, no. 1, pp. 65–80, 1997.

[22] B. Bona and M. Indri, "Friction Compensation in Robotics: an Overview," in *44th IEEE Conference on Decision and Control*, pp. 4360–4367, 2005.

[23] V. Lampaert, J. Swevers, and F. Al-Bender, "Modification of the Leuven integrated friction model structure," *IEEE Transactions on Automatic Control*, vol. 47, pp. 683–687, Apr. 2002.

[24] V. Lampaert, F. Al-Bender, and J. Swevers, "A generalized Maxwell-slip friction model appropriate for control purposes," in *Proceedings of International Conference Physics and Control*, vol. 4, pp. 1170 – 1177 vol.4, 2003.

[25] J. Zhao and D. J. Hill, "Dissipativity Theory for Switched Systems," *IEEE Transactions on Automatic Control*, vol. 53, no. 4, pp. 941–953, 2008.

[26] F. Al-Bender, V. Lampaert, and J. Swevers, "A Novel Generic Model at Asperity Level for Dry Friction Force Dynamics," *Tribology Letters*, vol. 16, pp. 81–93, Feb. 2004.

[27] K. Salisbury, F. Conti, and F. Barbagli, "Haptic rendering: introductory concepts," *Computer Graphics and Applications, IEEE*, vol. 24, pp. 24–32, Mar. 2004.

[28] J. E. Colgate and J. M. Brown, "Factors affecting the Z-Width of a haptic display," in *IEEE International Conference on Robotics and Automation*, pp. 3205–3210 vol.4, May 1994.

[29] R. J. Adams and B. Hannaford, "Stable haptic interaction with virtual environments," *IEEE Transactions on Robotics and Automation*, vol. 15, pp. 465–474, June 1999.

[30] N. Imasaki and M. Tomizuka, "Adaptive control of robot manipulators with anti-backlash gears," in *IEEE International Conference on Robotics and Automation Proceedings*, vol. 1, pp. 306 –311 vol.1, 1995.

[31] M. Nordin and P. O. Gutman, "Controlling mechanical systems with backlash - a survey," *Automatica*, vol. 38, pp. 1633–1649, Oct. 2002.

[32] H. Mokhtari and F. Barati, "A New Scheme for a Mechanical Load Position Control Driven by a Permanent Magnet DC Motor and a Nonzero Backlash Gearbox," in *IEEE International Symposium on Industrial Electronics*, vol. 3, pp. 2052–2057, 2006.

[33] M. Anand Mohan, "Position control in the presence of unknown output backlash," in *Proceedings of the Thirty-Seventh Southeastern Symposium on System Theory*, pp. 102–106, 2005.

[34] M. A. Mohan, "A New Compensation Technique for Backlash in Position Control Systems with Elasticity," in *Thirty-Ninth Southeastern Symposium on System Theory*, pp. 244–248, 2007.

[35] G. Tao and P. V. Kokotovic, "Adaptive control of system with unknown output backlash," *IEEE Transactions on Automatic Control*, vol. 40, no. 2, pp. 326–330, 1995.

[36] N. J. Ahmad, H. K. Ebraheem, and M. Q. Qasem, "Global Asmptotic Stability for Systems with Friction and Input Backlash," in *Proceedings of the IEEE International Symposium on Intelligent Control, Control and Automation*, pp. 212–218, 2005.

[37] J. Guo, B. Yao, Q. Chen, and J. Jiang, "Adaptive robust control for nonlinear system with input backlash or backlash-like hysteresis," in *IEEE International Conference on Control and Automation*, pp. 1962–1967, 2009.

[38] K. T. Woo, L.-X. Wang, F. L. Lewis, and Z. X. Li, "A fuzzy system compensator for backlash," in *IEEE International Conference on Robotics and Automation*, vol. 1, pp. 181 –186 vol.1, 1998.

[39] C. W. Tao, "Fuzzy control for linear plants with uncertain output backlashes," *IEEE Transactions on Systems, Man, and Cybernetics, Part B: Cybernetics*, vol. 32, no. 3, pp. 373–380, 2002.

[40] I. Mohammadzaman, A. K. Sedigh, and M. Nasirian, "Predictive Control of Non-minimum Phase Motor with Backlash in an Earth Station Antenna," in *Proceedings of Chinese Control Conference (CCC)*, pp. 900–905, 2006.

[41] I. Mohammadzaman, A. K. Sedigh, M. Nasirian, and M. H. Ferdowsi, "Predictive control of earth station antenna with backlash compensation," in *IEEE International Symposium on Intelligent Control*, pp. 2225–2230, 2006.

[42] L. Marton and B. Lantos, "Friction and backlash measurement and identification method for robotic arms," in *International Conference on Advanced Robotics (ICAR)*, pp. 1–6, 2009.

[43] C. Ma and Y. Hori, "Geometric Interpretation of Discrete Fractional Order Controllers Based on Sampling Time Scaling Property and Experimental Veri-

fication of Fractional 1/S[sup alpha] Systems' Robustness," *ASME Conference Proceedings*, vol. 2003, no. 37033, pp. 661–666, 2003.

[44] C. Ma and Y. Hori, "The application backlash of fractional order control to vibration suppression," in *Proceedings of the American Control Conference*, vol. 3, pp. 2901 – 2906 vol.3, 2004.

[45] E. G. Papadopoulos and G. C. Chasparis, "Analysis and model-based control of servomechanisms with friction," in *IEEE/RSJ International Conference on Intelligent Robots and Systems*, vol. 3, pp. 2109–2114 vol.3, 2002.

[46] S. C. P. Gomes and J. P. Chretien, "Dynamic modelling and friction compensated control of a robot manipulator joint," in *Proceedings of IEEE International Conference on Robotics and Automation*, pp. 1429 –1435 vol.2, 1992.

[47] N. V. Q. Hung, H. D. Tuan, T. Narikiyo, and P. Apkarian, "Adaptive Control for Nonlinearly Parameterized Uncertainties in Robot Manipulators," *IEEE Transactions on Control Systems Technology*, vol. 16, no. 3, pp. 458–468, 2008.

[48] M. Feemster, P. Vedagarbha, D. M. Dawson, and D. Haste, "Adaptive control techniques for friction compensation," in *Proceedings of American Control Conference*, vol. 3, pp. 1488–1492 vol.3, 1998.

[49] L. Mostefai, M. Denai, and Y. Hori, "Robot joint friction compensation based on a local modeling technique," in *IEEE International Workshop on Advanced Motion Control*, pp. 229–233, 2008.

[50] A. Alcocer, A. Robertsson, A. Valera, and R. Johansson, "Force Estimation and Control in Robot Manipulators," in *Robot control* (J. Sasiadek and I. Duleba, eds.), pp. 31–36, Elsevier, 2004.

[51] K. S. Eom, I. H. Suh, W. K. Chung, and S. R. Oh, "Disturbance observer based force control of robot manipulator without force sensor," in *IEEE International Conference on Robotics and Automation*, vol. 4, pp. 3012–3017 vol.4, May 1998.

[52] K. Ohishi, M. Miyazaki, and M. Fujita, "Hybrid control of force and position without force sensor," in *Proceedings of the International Conference on Power Electronics and Motion Control, Industrial Electronics, Control, Instrumentation, and Automation*, pp. 670–675 vol.2, Nov. 1992.

[53] Z. Jamaludin, H. Van Brussel, and J. Swevers, "Friction Compensation of an Feed Table Using Friction-Model-Based Feedforward and an Inverse-Model-Based Disturbance Observer," *IEEE Transactions on Industrial Electronics*, vol. 56, pp. 3848–3853, Oct. 2009.

[54] B. Friedland and Y.-J. Park, "On adaptive friction compensation," in *Proceedings of the 30th IEEE Conference on Decision and Control*, pp. 2899–2902 vol.3, Dec. 1991.

[55] J. Amin, B. Friedland, and A. Harnoy, "Implementation of a friction estimation and compensation technique," in *IEEE International Conference on Control Applications*, pp. 804–808, Sept. 1996.

[56] B. Armstrong-Helouvry and B. Amin, "PID control in the presence of static friction: exact and describing function analysis," in *American Control Conference*, vol. 1, pp. 597–601 vol.1, June 1994.

[57] P. E. Dupont, "Avoiding stick-slip through PD control," *IEEE Transactions on Automatic Control*, vol. 39, pp. 1094–1097, May 1994.

[58] E. Tung, G. Anwar, and M. Tomizuka, "Low Velocity Friction Compensation and Feedforward Solution based on Repetitive Control," in *American Control Conference*, pp. 2615–2620, June 1991.

[59] H. Du and S. S. Nair, "Low velocity friction compensation," *IEEE Control Systems*, vol. 18, pp. 61–69, Apr. 1998.

[60] C.-Y. Chen, M.-M. Cheng, C.-F. Yang, and J.-S. Chen, "Robust Adaptive Control for Robot Manipulators with Friction," in *International Conference on Innovative Computing Information and Control*, p. 422, June 2008.

[61] S. I. Han, Y. S. Cho, S. M. Jin, C. D. Lee, and S. Y. Yang, "Adaptive friction observer and sliding mode controller development with RFNN for nonlinear friction compensation," in *ICCAS-SICE*, pp. 4971–4976, Aug. 2009.

[62] W.-F. Xie and Z.-Y. Zhao, "Sliding-Mode Observer Based Adaptive Control for Servo Actuator with Friction," in *International Conference on Mechatronics and Automation*, pp. 1196–1201, Aug. 2007.

[63] N. Hogan, "Impedance control - An approach to manipulation. I - Theory. II - Implementation. III - Applications," *ASME Transactions Journal of Dynamic Systems and Measurement Control B*, vol. 107, pp. 1–24, Mar. 1985.

[64] G. Alici and R. W. Daniel, "Importance of resolution of joint encoders during robotic hard-on-hard tasks," in *Proc. IEE Colloquium Precision Motion Control in Robotics and Machine Drives*, 1994.

[65] J. P. N. Glover and G. Dodds, "Small motion robot dynamics simulated in real-time," in *Proc. IEE Colloquium Precision Motion Control in Robotics and Machine Drives*, 1994.

[66] B. Bona and M. Indri, "Friction compensation and robustness issues in force/-position controlled manipulators," *IEE Proceedings on Control Theory and Applications*, vol. 142, pp. 569–574, Nov. 1995.

[67] A. Tornambe, "Global regulation of a planar robot arm striking a surface," *IEEE Transactions on Automatic Control*, vol. 41, pp. 1517–1521, Oct. 1996.

[68] P. R. Pagilla and B. Yu, "A stable transition controller for constrained robots," *IEEE/ASME Transactions on Mechatronics*, vol. 6, pp. 65–74, Mar. 2001.

[69] J. M. Hyde and M. R. Cutkosky, "Contact transition control: an experimental study," in *Proceedings of EEE International Conference on Robotics and Automation*, pp. 363 –368 vol.1, 1993.

[70] T.-J. Tarn, Y. Wu, N. Xi, and A. Isidori, "Force regulation and contact transition control," *IEEE Control Systems Magazine*, vol. 16, pp. 32–40, Feb. 1996.

[71] Y. Wu, T.-J. Tarn, N. Xi, and A. Isidori, "On robust impact control via positive acceleration feedback for robot manipulators," in *IEEE International Conference on Robotics and Automation*, vol. 2, pp. 1891 –1896 vol.2, 1996.

[72] E. Lee, "Force and impact control for robot manipulators using time delay," in *Proceedings of the IEEE International Symposium on Industrial Electronics*, vol. 1, pp. 151 –156 vol.1, 1999.

[73] C. Liang, S. Bhasin, K. Dupree, and W. E. Dixon, "A force limiting adaptive controller for a robotic system undergoing a non-contact to contact transition," in *Proceedings of 46th IEEE Conference on Decision and Control*, pp. 3555–3560, 2007.

[74] N. Doh, W. K. Chung, and Y. Youm, "On hard contact force control," in *Proceedings of IEEE/RSJ International Conference on Intelligent Robots and Systems (IROS), VOLS 1-3*, pp. 1528–1533, 2000.

[75] I. D. Walker, "The use of kinematic redundancy in reducing impact and contact effects in manipulation," in *IEEE International Conference on Robotics and Automation*, pp. 434 –439 vol.1, 1990.

[76] M. W. Gertz, J.-O. Kim, and P. K. Khosla, "Exploiting redundancy to reduce impact force," in *IEEE/RSJ International Workshop on Intelligent Robots and Systems*, pp. 179 –184 vol.1, 1991.

[77] K. Dupree, W. E. Dixon, G. Hu, and C. Liang, "Lyapunov-based control of a robot and mass-spring system undergoing an impact collision," in *American Control Conference*, p. 6 pp., 2006.

[78] K. Dupree, C. Liang, G. Hu, and W. E. Dixon, "Global Adaptive Lyapunov-Based Control of a Robot and Mass-Spring System Undergoing An Impact Collision," in *Proceedings of 45th IEEE Conference on Decision and Control*, pp. 2039–2044, 2006.

[79] K. Dupree, C.-H. Liang, G. Hu, and W. E. Dixon, "Adaptive Lyapunov-Based Control of a Robot and Mass-Spring System Undergoing an Impact Collision," *IEEE Transactions on Systems, Man, and Cybernetics, Part B: Cybernetics*, vol. 38, no. 4, pp. 1050–1061, 2008.

[80] S. B. Karunakar and A. A. Goldenberg, "Contact stability in model-based force control systems of robot manipulators," in *Proc. Symp. IEEE Int Intelligent Control*, pp. 412–417, 1988.

[81] D. A. Horsley, D. Hernandez, R. Horowitz, A. K. Packard, and A. P. Pisano, "Closed-loop control of a microfabricated actuator for dual-stage hard disk drive servo systems," in *Proceedings of American Control Conference*, vol. 5, pp. 3028 –3032 vol.5, 1998.

[82] S.-H. Lee and Y.-H. Kim, "Comparative design of dual-stage actuator control systems for hard disk drives," in *IEEE International Symposium on Industrial Electronics*, vol. 3, pp. 2108 –2113 vol.3, 2001.

[83] Y.-H. Kim and S.-H. Lee, "An approach to dual-stage servo design in computer disk drives," *IEEE Transactions on Control Systems Technology*, vol. 12, no. 1, pp. 12–20, 2004.

[84] M. Zinn, O. Khatib, and B. Roth, "A new actuation approach for human friendly robot design," in *IEEE International Conference on Robotics and Automation*, vol. 1, pp. 249 – 254 Vol.1, 2004.

[85] H. Vallery, J. Veneman, E. van Asseldonk, R. Ekkelenkamp, M. Buss, and H. van Der Kooij, "Compliant actuation of rehabilitation robots," *IEEE Robotics Automation Magazine*, vol. 15, no. 3, pp. 60–69, 2008.

[86] K. Nagai, Y. Shiigi, Y. Ikegami, R. Loureiro, and W. S. Harwin, "Impedance control of redundant drive joints with double actuation," in *IEEE International Conference on Robotics and Automation (ICRA)*, pp. 1528–1534, 2009.

[87] K. Nagai, Y. Dake, Y. Shiigi, R. C. V. Loureiro, and W. S. Harwin, "Design of Redundant Drive Joints with Double Actuation using springs in the second actuator to avoid excessive active torques," in *IEEE International Conference on Robotics and Automation (ICRA)*, pp. 805–812, 2010.

[88] A. L. Barrow and W. S. Harwin, "High Bandwidth, Large Workspace Haptic Interaction: Flying Phantoms," in *Symposium on Haptic interfaces for virtual environment and teleoperator systems*, pp. 295–302, 2008.

[89] O. Khatib, "Reduced Effective Inertia in Macro-/Mini-manipulator Systems," in *The Fifth International Symposium on Robotics Research*, (Cambridge, MA, USA), pp. 279–284, MIT Press, 1990.

[90] K. Nagai and T. Yoshikawa, "Impedance control of redundant macro-micro manipulators," in *Proceedings of the IEEE/RSJ/GI International Conference on Intelligent Robots and Systems*, vol. 2, pp. 1438 –1445 vol.2, 1994.

[91] A. Sharon, N. Hogan, and D. E. Hardt, "Controller design in the physical domain (application to robot impedance control)," in *IEEE International Conference on Robotics and Automation*, pp. 552–559 vol.1, May 1989.

[92] D. C. Hu and B. C. Chang, "Multivariable controller design for hard drive dual-stage actuator servo systems," in *IEEE International Conference on Mechatronics*, pp. 404–409, 2005.

[93] J. Zheng, M. Fu, Y. Wang, and C. Du, "Nonlinear Tracking Control for a Hard Disk Drive Dual-Stage Actuator System," *IEEE/ASME Transactions on Mechatronics*, vol. 13, no. 5, pp. 510–518, 2008.

[94] B.-S. Kim, J.-J. Park, and J.-B. Song, "Improved manipulation efficiency using a serial-type dual actuator unit," in *International Conference on Control, Automation and Systems ICCAS*, pp. 30–35, 2007.

[95] B.-S. Kim, J.-B. Song, and J.-J. Park, "A Serial-Type Dual Actuator Unit With Planetary Gear Train: Basic Design and Applications," *IEEE/ASME Transactions on Mechatronics*, vol. 15, no. 1, pp. 108–116, 2010.

[96] B.-S. Kim and J.-B. Song, "Hybrid dual actuator unit: A design of a variable stiffness actuator based on an adjustable moment arm mechanism," in *IEEE International Conference on Robotics and Automation (ICRA)*, pp. 1655–1660, 2010.

[97] K. Nagai and T. Yoshikawa, "Impedance control of redundant macro-micro manipulators," in *Proceedings of the IEEE/RSJ/GI International Conference on Intelligent Robots and Systems*, vol. 2, pp. 1438–1445 vol.2, 1994.

[98] W. S. Lee and M. V. C. Rao, "Modeling and design of tape transport mechanism," *Mathematics and Computers in Simulation*, vol. 72, no. 1, pp. 26–37, 2006.

[99] C. Mitsantisuk, S. Katsura, and K. Ohishi, "Variable power assist control of twin direct-drive motor system based on human stiffness estimation," in *Proceedings of 10th IEEE Int. Workshop Advanced Motion Control (AMC)*, pp. 520–525, 2008.

[100] C. Mitsantisuk, K. Ohishi, S. Urushihara, and S. Katsura, "Identification of twin direct-drive motor system with consideration of wire rope tension," in *Proceedings of IEEE International Conference on Mechatronics (ICM)*, pp. 1–6, 2009.

[101] C. Mitsantisuk, S. Katsura, and K. Ohishi, "Force Control of Human–Robot Interaction Using Twin Direct-Drive Motor System Based on Modal Space Design," vol. 57, no. 4, pp. 1383–1392, 2010.

[102] K. Nagai, T. N. Le, Y. Hayashi, and K. Ito, "Proposal of a Redundant Drive Wire Mechanism for producing motions with high acceleration and high precision," in *IEEE/SICE International Symposium on System Integration (SII)*, pp. 1049–1054, 2011.

[103] K. Nagai, T. N. Le, Y. Hayashi, and K. Ito, "Kinematical analysis of redundant drive wire mechanisms with velocity constraint," in *International Conference on Mechatronics and Automation (ICMA)*, pp. 1496–1501, 2012.

[104] R. D. Valentine, J. G. Trasky, and D. R. Rippin, "Load Sharing of Dual Motor Grinding Mill Drives," *IEEE Transactions on Industry Applications*, vol. IA-13, pp. 161–168, Mar. 1977.

[105] V. E. Wagner, "Load Sharing in Dual Drive Conveyors," *IEEE Transactions on Industry Applications*, vol. IA-20, pp. 1412–1417, Nov. 1984.

[106] A. Lacoponi, "Taming the beast," *Control Automation*, vol. 18, no. 6, pp. 36–41, 2007.

[107] L. F. Shampine, *Numerical Solution of Ordinary Differential Equations*. No. v. 4 in Chapman & Hall mathematics, Taylor & Francis, 1994.

[108] G. F. Franklin, D. J. Powell, and A. Emami-Naeini, *Feedback Control of Dynamic Systems*. Upper Saddle River, NJ, USA: Prentice Hall PTR, 4th ed., 2001.

Appendices

Appendix A

Stability analysis

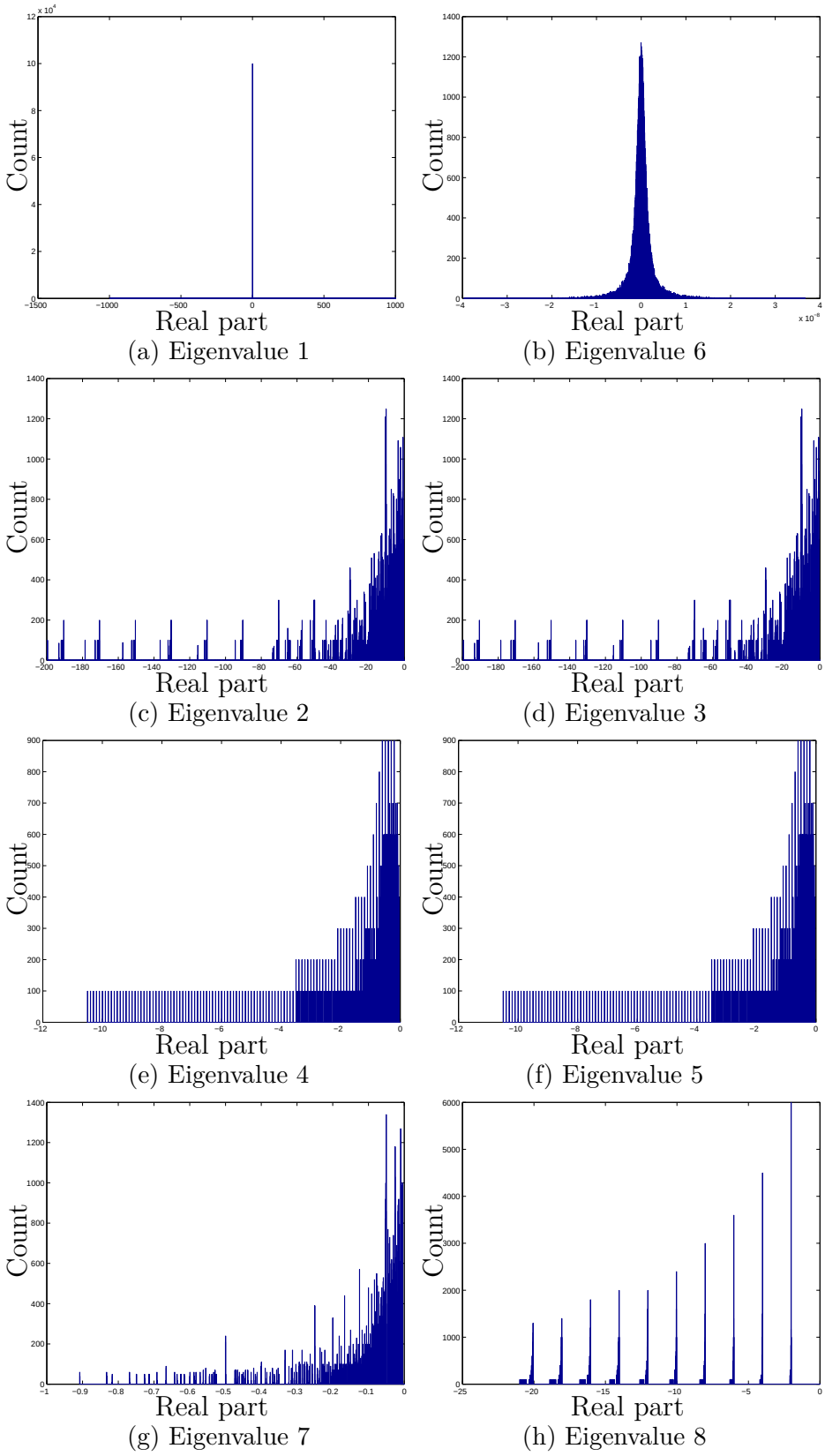

(a) Eigenvalue 1 (b) Eigenvalue 6

(c) Eigenvalue 2 (d) Eigenvalue 3

(e) Eigenvalue 4 (f) Eigenvalue 5

(g) Eigenvalue 7 (h) Eigenvalue 8

Figure A.1: Real part of Eigenvalues of 4DoF system

Appendix B

MATLAB files

B.1 Coulomb friction simulation

```
clear all; close all;
w=2*pi;
tvect=0:0.0001:(2*pi/w);  %time for two cycles
a=1;               %amplitude of sinusioud
C=0.6;             %coulomb limits

fa = a*sin(w*tvect);  %forcing function
tcp=asin(C/a)/w;   %tc is when fa exceeds C
tcn=asin(C/a)/w+pi/w;

%pm is +1 if  +/-   and -1 if -/+
fvel=@(t,tc,pm)(a/w*(cos(w*tc)-cos(w*t))+pm*C*tc-pm*C*t);
fpos=@(t,tc,pm)(a/(w^2)*(sin(w*tc)-sin(w*t))-pm*C/2*(t.^2-tc.^2) + a/w*cos(w*tc).*(t-tc)+pm*C*tc.*(t-tc));

%plot(tvect,fa+C,'k--'); plot(tvect,fa-C,'k-.');  %plots the upper/lower coulomb

vel=zeros(1,length(tvect));  pos=zeros(1,length(tvect));
fres=zeros(1,length(tvect)); fc=zeros(1,length(tvect));

posDir=1;
finalPos=0;
for i=1:length(tvect)
    t=tvect(i);
    if (posDir>0)
        if (t<tcp)
            vel(i)=0; pos(i)=0; fres(i)=0; fc(i)=0;
        else
            vel(i)=fvel(t,tcp,1);
            pos(i)=fpos(t,tcp,1);
            fc(i)=-C;
            fres(i)=fa(i)-C;
            if (vel(i)<=0)
                vel(i)=0; posDir=0; finalPos=pos(i);
            end
```

```
35          end
36      else
37          if (t<tcn)
38              vel(i)=vel(i-1); pos(i)=pos(i-1); fres(i)=0; fc(i)=0;
39          else
40              vel(i)=fvel(t,tcn,-1);
41              pos(i)=finalPos+fpos(t,tcn,-1);
42              fres(i)=fa(i)+C;
43              fc(i)=C;
44              if (vel(i)>=0)
45                  vel(i)=0; posDir=1;
46                  tcp=tcp+2*pi/w;
47                  tcn=tcn+2*pi/w;
48              end
49          end
50      end
51  end
52
53  t_tplot=figure; hold on; %PART e
54  plot(tvect,fres./10,'k');
55  plot(tvect,pos,'k--');
56  plot(tvect,vel,'k-.');
57  xlabel('Time (sec)','interpreter','latex');
58  legend({'Fr/10','Velocity','Position'});
59
60  t_pos_vel=figure; plot(pos,vel,'k'); grid on;
61  xlabel('Position $x$','interpreter','latex');
62  ylabel('Velocity $\dot{x}$','interpreter','latex');
63  axis([-0.005 0.025 -0.1 0.1]);
64
65  t_vel_ff=figure; plot(vel, -1*fc,'k'); grid on;
66  xlabel('Velocity $\dot{x}$','interpreter','latex');
67  ylabel('Friction force $f_c$','interpreter','latex');
68  axis([-0.1 0.1 -1 1]);
69
70  t_pos_fa=figure; plot(pos, fa,'k'); grid on;
71  xlabel('Position $x$','interpreter','latex');
72  ylabel('Applied force $f_a$','interpreter','latex');
73  axis([-0.005 0.025 -1.2 1.2]);
74
75  t_vel_fa=figure; plot(vel, fa,'k'); grid on;
76  xlabel('Velocity $\dot{x}$','interpreter','latex');
77  ylabel('Applied force $f_a$','interpreter','latex');
78  axis([-0.09 0.09 -1.2 1.2]);
```

B.2 Eigenvalue plot generation

As the eigenvalues for systems of order 4 and higher are challenging to express algebraically, to assess the stability of such systems, numerical analysis is necessary. The MATLAB code below generates a histogram plot of each eigenvalue for every combination of system parameters.

```
close all

%preallocate so loops are faster
eigens=zeros(8,100001);
params=zeros(6,100001);
i=1;

%Each parameter swept in reasonable range
for Jm=1e-4:2e-4:2e-3
 for Bm=2e-5:2e-5:2e-4
  for Jc=1e-5:2e-5:2e-4
   for JL=1e-5:2e1-5:2e-4
    for Bg=1e-4:2e-4:2e-3
     for Bc=1e-8:2e-8:2e-7
      eigens(:,i)=GetEigens( Kg, Jm, Bm, Jc, JL, Bg, Bc );
      params(:,i) = [Jm;Bm;Jc;JL;Bg;Bc];
      i=i+1;
     end
    end
   end
  end
 end
end

for i=1:8
    fhandle=figure;
    hist(real(eigens(i,:)),2000)
    %title(sprintf('Histogram for eigenvalue %d',i));
    xlabel('Real part of the pole','FontSize',12);
    ylabel('Count of values','FontSize',12);
    %print(fhandle,'-dps2',sprintf('eigen%d.eps',i));
end
```

```
function [ eigens ] = GetEigens( Kg, Jm, Bm, Jc, JL, Bg, Bc )
%GETEIGENS Computes the eigenvalues for the A matrix 8thOrder

sA=[0 1 0 0 0 0 0 0;
   -Kg/Jm -(Bm+Bg)/Jm Kg/Jm Bg/Jm 0 0 0 0;
    0 0 0 1 0 0 0 0;
    Kg/Jc Bg/Jc -(2*Kg)/Jc -(2*Bg+Bc)/Jc Kg/Jc Bg/Jc 0 0;
    0 0 0 0 0 1 0 0;
    0 0 Kg/Jm Bg/Jm -Kg/Jm -(Bg+Bm)/Jm 0 Bm/Jm;
    0 0 0 0 0 0 0 1;
    0 0 0 0 0 Bm/JL 0 -Bm/JL];

eigens=eig(sA);

end
```

B.3 fminsearch

Estimation of parameters for a second order step response using MATLAB *fminsearch* function.

```
% fit the step response of data to 2nd order response
function err=fitStep(xx,data)
% xx=[A zeta omega]
%
% Usage: (vector at end are initial guess of xx)
% [Xfinal,feval] = fminsearch(@(x) fitStep(x,stepdata),[.5 0.6 1.8/0.1]);

A=xx(1);
zeta=xx(2);
omega=xx(3);
t0=(0:0.001:1.999)';
srt1mzeta2=sqrt(1-zeta^2);
phi=atan2(srt1mzeta2,zeta);

r=A*(1-exp(-zeta*omega*t0).*(sin(omega*srt1mzeta2*t0+phi)));

err=sum((r-data).^2);

%At the prompt, recover parameters and get step response
% A=X2(1);zeta=X2(2);omega=X2(3);t0=(0:0.001:1.999)';
% srt1mzeta2=sqrt(1-zeta^2);phi=atan2(srt1mzeta2,zeta);
% r=A*(1-exp(-zeta*omega*t0).*(sin(omega*srt1mzeta2*t0+phi)));
```